Characterization of Anomalous Ion Heating in Ultra-Low Safety Factor Toroidal Pinch Plasmas

by

Armand Kayvon Keyhani

A dissertation submitted in partial fulfillment of

the requirements for the degree of

Doctor of Philosophy

(Nuclear Engineering and Engineering Physics)

at the

UNIVERSITY OF WISCONSIN–MADISON

2025

Date of final oral examination: 08/13/2025

The dissertation is approved by the following members of the Final Oral Committee:

Cary B. Forest, Professor, Physics

Benedikt Geiger, Professor, Engineering Physics

Mark D. Nornberg, Scientist, Engineering Physics

John S. Sarff, Professor, Physics

Carl R. Sovinec, Professor Emeritus, Engineering Physics

Abstract

Ultra-low safety factor (ULq) plasmas having edge safety factor q_a with a range of $0 < q_a < 1$ lie in the regime of toroidal pinch plasmas between the tokamak which has $q_a > 2$ and the reversed-field pinch which has $q_a < 0$. ULq plasmas are poorly understood due to their susceptibility to external kink modes, which can cause disruption, and their weak magnetic shear which makes them unstable to interchange modes. Interchange leads to poor confinement which causes them to have high global electrical resistance R_P, making them difficult to sustain in most devices. ULq plasmas can be sustained with steady parameters in MST due to its thick conducting shell which stabilizes external kink modes and feedback power supplies which can drive the high loop voltages necessary to sustain them. This thesis investigates the variation of impurity temperature T_z with discharge parameters and the mechanism of the impurity heating in ULq plasmas.

Magnetic fluctuations, electron density fluctuations, plasma potential fluctuations, and T_z in ULq plasmas are characterized. Impurity (B-IV 282.2 nm) T_z is observed as high as 400 eV, or up to 3× the electron temperature. T_z has a strong dependence on q_a and tends to increase as q_a decreases. T_z is highest at $q_a \approx 0.6$. At $q_a \approx 0.55$, there is an abrupt decrease in fluctuation amplitudes, T_z, and R_P. T_z has a greater than linear inverse dependence on line-averaged electron density $\bar{n}_e$. R_P is minimized when $\bar{n}_e \approx 5 \times 10^{18}\ m^{-3}$. At fixed q_a, T_z increases roughly linearly as toroidal field and plasma current are increased.

Observations suggest that strong magnetic and plasma potential fluctuations are associated with the rotation of radially-localized helical resonant modes. Increases in fluctuation frequencies and amplitudes are associated with increases in $\bar{T}_z$, which all depend strongly on q_a and $\bar{n}_e$. Broadband radial electric field fluctuations $\tilde{E}_r$ are observed with RMS amplitudes as high as 14 kV/m. Impurity heating power estimates for ion cyclotron resonance damping and viscous dissipation are much lower than the power required to sustain the observed $\bar{T}_z$. The estimate of stochastic heating power due to broadband $\tilde{E}_r$ is consistent with the required heating power.

Acknowledgements

It is hard to believe that my time in grad school is finally coming to an end after nearly 8 years. It has been very challenging at times but highly rewarding overall. Dealing with the pandemic, multiple surgeries, and changing thesis projects was far from ideal, but this experience has shown me how important the people we surround ourselves with are to our success and well-being. I have been so fortunate to be supported by the best mentors, colleagues, and friends anyone could ask for, and I would like to acknowledge some of them here.

First of all, I must thank my advisor and first contact at UW-Madison, Carl Sovinec. My admissions process was not typical, but I suppose my persistence paid off. I will forever be grateful for your help in obtaining the opportunity to start my graduate studies at UW-Madison with the support of a teaching assistant position. I eventually found a research project at the Pegasus experiment, but after several years of work it became necessary for me to leave the project. You took over as my research advisor and found me this fascinating project which enabled me to finish my degree. Thank you for your commitment to my education, your patience, invaluable discussions on plasma physics, and your contributions to this dissertation.

A special thanks to Mark Nornberg, who I worked closely with at Pegasus and who then contributed significantly to this work. I owe all of my knowledge of plasma sources,

high-voltage systems, optics, and spectroscopy to your guidance. I am grateful for your commitment to my research, our many insightful discussions, your feedback while writing this dissertation, and for your assistance with the spectrometer and data analysis.

To John Sarff, my advisor at MST, thank you for the opportunity to conduct this research and for warmly welcoming me into the group. I am grateful for your contributions to developing these experiments, the many hours of discussions we have had, your patience in teaching me new concepts, and your feedback while writing this dissertation. Your vast knowledge of plasma physics and the MST facility were essential to the completion of this work.

Thank you to Daniel Den Hartog and Noah Hurst for your assistance in developing experiments and analysis as well as insightful discussions of the results. Noah and Abdulgader Almagri, I am grateful for your assistance with implementing the deep-insertion probe and analysis of the data. Abdulgader and Constance Rouda, I am indebted to you for your assistance in obtaining the last-minute data with the capacitive probe, which proved to be a crucial part of my data set. Thank you to Brett Chapman, Karsten McCollam, and Cary Forest for your valuable discussions and advice.

This work would not have been possible without the help of the MST staff. Alex Squitieri, thank you for your assistance in implementing the new data acquisition system for the spectrometer, reducing noise pickup, and keeping MST running. Paul Wilhite, thank you for your assistance with computer issues, finding my data, and keeping the data acquisition system working. Patrick Tracy, thank you for your efforts to keep the MST facility running as things randomly break (and we break things). Don Holly, thank you for your assistance in keeping the MST power supplies functional. Thank you everyone who operated MST for my experiments and learned how to operate ULq plasmas with me.

To my fellow MST grad students and office mates Ben Antognetti, Joe Flahavan, Carlos

Ortiz, and Sam Farrar, it has been a pleasure working with you guys, discussing physics, and engaging in witty (and not so witty) banter. Our conversations definitely kept me sane while writing this thesis.

I am so privileged to have been a part of the MST research group. It provides a unique plasma facility, personnel with vast experience in engineering and plasma physics, and an environment that fosters discovery and learning. I hope that future graduate students get to enjoy contributing to research at MST for many years to come.

Graduate school is difficult, and life can make it even more so. I can not imagine navigating it without the friends I made along the way. In particular, I am deeply grateful to Ricardo, Temo, and Carolyn for your friendship and support when it was most needed.

Finally, I want to thank my family, who supported me in my move across the country and throughout grad school. Dad, you always pushed me to strive for excellence in academics. I did not appreciate it at the time, but I can say for certain that I would not be here writing this thesis without your consistent guidance, love, and support. Mom, thank you for your endless love and encouragement. To my brothers Adam and Bejan, thank you for your support over the years and for teaching me about computers, science, and electronics from a young age. The path to this accomplishment began with your influence and encouragement of my curiosity.

Contents

Abstract **i**

Acknowledgements **iii**

1 Introduction **1**

1.1 Magnetic Confinement Fusion 1

1.2 Toroidal Plasma Pinches: the Tokamak, RFP, and ULq Regimes 3

1.3 Ion Heating in Magnetized Plasmas 11

1.4 Summary of Research Objectives, Observations, and Results 14

1.5 Outline of Thesis 15

2 Background and Motivation **17**

2.1 Ion Heating in the Solar Corona 17

2.2 Ion Heating Studies of the RFP 18

2.3 Past Experimental and Computational Work on ULq 24

2.4 Potential Ion Heating Mechanisms 30

2.5 Summary 36

3 The Madison Symmetric Torus and Diagnostics **39**

3.1 The Madison Symmetric Torus 39

3.2 External Magnetic Coil Arrays 41
3.3 Insertable Probes 43
3.4 Far Infrared Interferometer 44
3.5 Ion Doppler Spectrometer 45
3.6 Summary of Diagnostics 52

4 ULq Pinch Operation and Observations 54

4.1 Startup and Current Ramp 54
4.2 Neutral Particle Transport and Energy Confinement 56
4.3 Magnetohydrodynamic Activity 59
4.4 Equilibrium Properties 63
4.5 Ion Heating 66
4.6 Summary of ULq Properties 68

5 Experiments, Data, and Analysis 70

5.1 Edge Safety Factor Scan 71
5.2 Plasma Density Scan 74
5.3 Toroidal Field Scan 77
5.4 Fluctuation Analysis of Select Edge Safety Factor Values 79
5.5 Summary and Discussion 102

6 Evaluation of Potential Ion Heating Mechanisms 106

6.1 Power Balance 107
6.2 Ion Cyclotron Resonance Heating 113
6.3 Stochastic Heating 116
6.4 Viscous Heating 119

7 Conclusion **121**

7.1 Summary of Observations 122

7.2 Summary of Conclusions 127

7.3 Suggestions for Future Work 128

Bibliography **132**

Chapter 1

Introduction

1.1 Magnetic Confinement Fusion

Controlled nuclear fusion has the potential to significantly reduce the world's dependence on fossil fuels and the impact of climate change. Nuclear fusion is the process where low-mass atomic nuclei are forced to overcome their Coulomb repulsion, combine to form heavier nuclei, and release nuclear binding energy. Nuclear fusion is the source of energy in the Sun where hydrogen nuclei are fused to produce helium. The Sun sustains these fusion reactions by confining the particles through its intense gravity, and the pressure maintained by this gravitational confinement and the continuous heating from fusion reactions drives a self-sustaining thermonuclear plasma. Fusion energy science seeks to harness a similar process to generate a sustainable source of energy for heat and electrical power generation. A significant challenge to achieving fusion energy is developing an economical method of heating and confining a large volume of hydrogen plasma to the degree where sufficient fusion reactions are sustained. One of the most researched methods of achieving these plasma conditions uses strong magnetic fields to trap hydrogen plasmas, with many configurations and technologies explored since the 1950s [1].

The performance of a magnetic confinement device is generally gauged based on the value of its triple product $n\,T_i\,\tau_E$ where n is the plasma number density, T_i is the temperature of the plasma ions, and τ_E is the energy confinement time which describes the rate of energy loss from the plasma. A fusion reactor using deuterium-tritium fuel must exceed a triple product value of about $1 \times 10^{21}\ keV\,m^{-3}\,s$, in order to achieve break-even energy production [2]. The tokamak is, so far, the best performing magnetic confinement device and a viable platform for nuclear fusion energy generation [3]. It consists of a torus-shaped vacuum vessel surrounded by several strong electromagnet coils as illustrated in figure 1.1. The vacuum vessel provides a low impurity environment for controlled deuterium-tritium fueling of the plasma, and the magnetic fields provide particle and energy confinement. Several electromagnet coils encircle the plasma along the torus to produce a toroidally oriented magnetic field B_T throughout the plasma volume, and a large solenoid is located in the central void to induce a toroidal electric current I_P in the plasma. Electric current is ramped in the central solenoid to induce a toroidal electric field which ionizes the fuel gas into a conductive plasma. Continued ramping of the solenoid current induces a strong I_P which produces a poloidal magnetic field B_P encircling the plasma. The resultant of the B_P sourced by the plasma current and the B_T applied by the magnet coils is a helical magnetic field throughout the plasma volume. Due to the Lorentz force, charged particles tend to spiral and flow along these field lines, and this tendency is utilized by the tokamak to confine charged particles and sustain high plasma pressures. The helical magnetic field configuration, rather than purely B_T or purely B_P, is necessary to maintain stability of the I_P and plasma pressure as well as mitigate particle and energy losses due to various outward particle drifts. Additionally, several other magnet coils are employed to provide positioning and plasma shaping functions. A fusion reactor concept like this, along with proper heat extraction and radiation shielding, could be engineered to maintain large thermonuclear plasmas as a source of sustainable energy. [4]

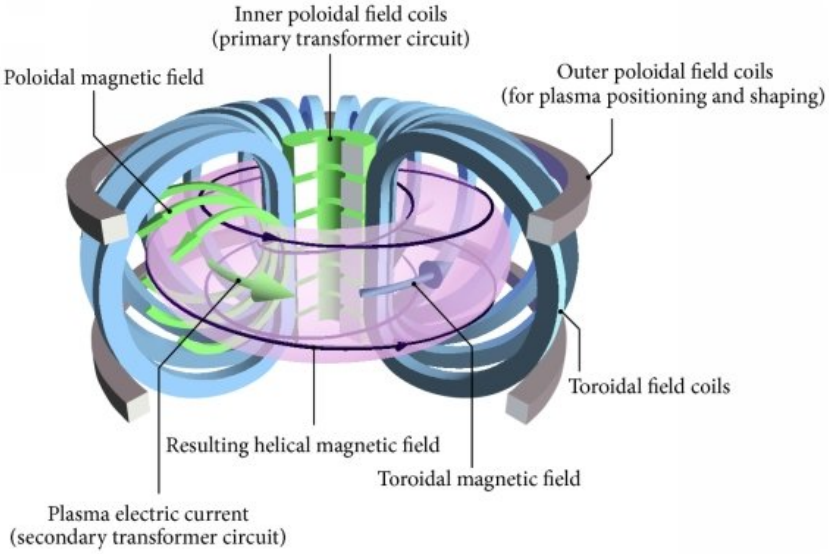

Figure 1.1: Diagram of a tokamak plasma current (purple) confined by toroidal field coils (blue). The central solenoid (green) is used to inductively drive plasma current (green) along the externally applied toroidal field (blue), resulting in a helical magnetic field (black). Additional poloidal field coils (grey) enable control of the plasma position and shape. Figure reproduced from [5].

1.2 Toroidal Plasma Pinches: the Tokamak, RFP, and ULq Regimes

Plasma pinches were some of the first magnetic confinement techniques explored for producing fusion energy. The term "pinch" refers to the inward force experienced by a plasma column which arises due an axial electric current flowing in the plasma. The Lorentz force equation,

$$\mathbf{f} = \rho(\mathbf{E} + \mathbf{v} \times \mathbf{B}) \,, \tag{1.1}$$

gives the force per unit volume $\mathbf{f}$ acting on a particle distribution with charge per unit volume ρ due to an electric field $\mathbf{E}$ or a velocity $\mathbf{v}$ through a magnetic field $\mathbf{B}$. Neglecting the electric field component and substituting $\mathbf{J} = \rho\mathbf{v}$, where $\mathbf{J}$ is the current per unit area, yields

$$\mathbf{f} = \mathbf{J} \times \mathbf{B} \,. \tag{1.2}$$

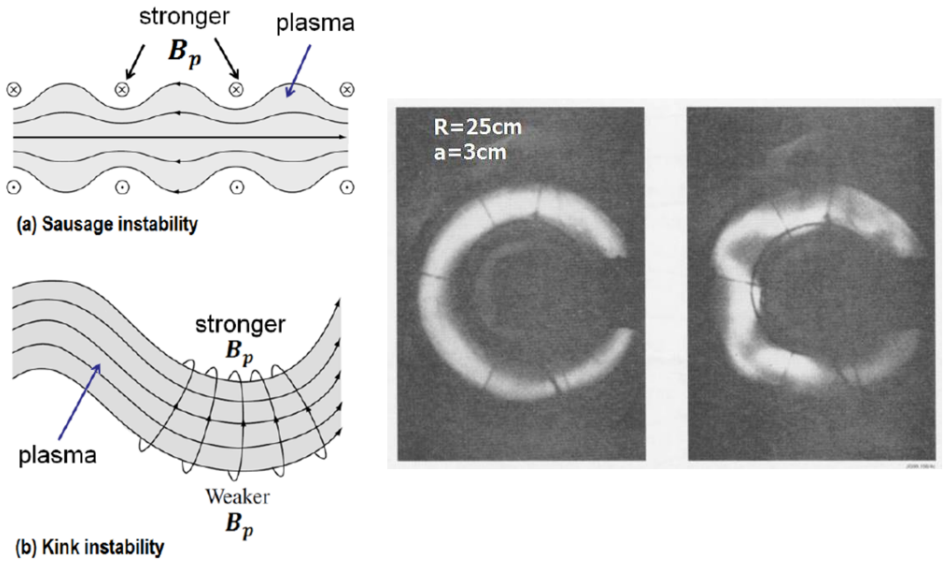

Figure 1.2: (Left) Illustration of MHD instabilities in a pinch with strong axial current and weak axial magnetic field. For the sausage instability, a perturbation which pinches the plasma column inwards results in stronger poloidal field at the pinch point and an even greater $J \times B$ pinching force, driving the instability. For the kink instability, a perturbation which slightly kinks the plasma column enhances the poloidal field on one side and reduces it on the other, further driving the kink deformation. Figure reproduced from [4]. (Right) Images of an early toroidal pinch before and after onset of global instability. The plasma deformation causes total displacement of the plasma and sudden loss of the plasma's stored energy to the pyrex chamber [UKAEA].

Thus, a plasma column carrying an axial current which generates a poloidal magnetic field will experience an inward force due to the current's interaction with its own magnetic field, the pinch effect [6]. Early pinch devices operated with only axial current (a Z-pinch), and as a result they suffered from large scale plasma instabilities that severely limited their discharge duration and performance due to rapid loss of plasma confinement and termination of the discharge. An illustration of the sausage and kink instabilities in a cylindrical pinch plasma is shown in 1.2 along with images of an early toroidal pinch plasma before and after the onset of global instability. In a plasma column carrying an axial current, the column is susceptible to instability because a small perturbation to the current channel results in a change in the magnetic field which enhances the deformation of the column. Another type of pinch with

only poloidal current (a θ-pinch) was explored; this configuration was much less susceptible to global instability but exhibited insufficient energy confinement times [7].

Global instability of axial current in a plasma pinch can be suppressed by the application of a strong axial magnetic field. A screw-pinch combines the stabilizing effect of the axial magnetic field with the confinement properties of the poloidal magnetic field, resulting in a helical or screw-shaped magnetic field. The screw-pinch configuration provided a significant improvement in confinement and stability, but linear devices still suffered from particle and energy loss by streaming out the ends of the confined region. This motivated the development of toroid-shaped devices which eliminated end losses by forming a closed loop of magnetic flux, effectively streaming the particles back into the confined region. The twist of the magnetic field lines is commonly characterized by the safety factor q. In the cylindrical approximation for toroidal geometry, q is defined as

$$q = \frac{rB_T}{RB_P} \tag{1.3}$$

where r is minor radius, B_T is the toroidal field strength, R is the major radius, and B_P is the poloidal field strength. On a given magnetic flux surface, q is essentially the number of toroidal transits per poloidal transit that a field line will make when traced. The safety factor at the plasma edge, q_a, is defined as

$$q_a = \frac{aB_T(a)}{RB_P(a)} \ , \tag{1.4}$$

where a is the plasma minor radius, $B_T(a)$ is the average toroidal field at the plasma edge, and $B_P(a)$ is the average poloidal field at the plasma edge. It was found that operating at higher B_T such that q_a was greater than 2 resulted in greatly improved stability and energy confinement. This operation regime became known as the tokamak and has remained the best performing magnetic confinement concept [1].

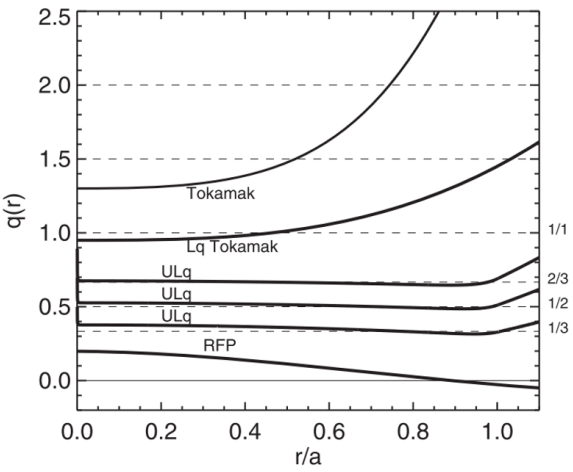

Figure 1.3: Sketches of tokamak, ultra-low safety factor (ULq), and RFP safety factor profiles. Figure reproduced from [8]

1.2.1 The Tokamak

In the tokamak, the B_T is almost entirely supported by external electromagnet coils while the B_P is generated by the internal toroidal plasma current I_P. The B_P is needed for good particle confinement, and the large B_T stabilizes both current-driven kink modes and pressure-driven interchange modes. The tokamak generally has a monotonically increasing radial safety factor profile $q(r)$ with the core value q_0 near 1 and increasing to an edge value of $q_a > 2.5$. An example of the tokamak's $q(r)$ profile is shown in 1.3.

At any location where the $q(r)$ value is equal to a rational number, the magnetic field lines will close on themselves on that surface allowing magnetohydrodynamic (MHD) modes to resonate. The modes that resonate on a rational surface will satisfy $q = m/n$ where m is the poloidal mode number and n is the toroidal mode number. For example, a $q(r) = 2$ surface within the plasma can be problematic because the m/n=2/1 tearing mode can resonate there, form magnetic islands (see Figure 1.4), and significantly degrade plasma confinement [4]. Optimally, magnetic flux contours in the poloidal cross section of a tokamak plasma will form nested flux surfaces. Ideal kink modes will deform the plasma without changing the

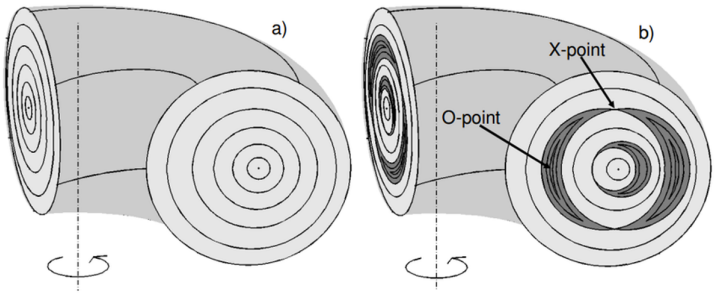

Figure 1.4: (a.) Illustration of a tokamak plasma cross section with nested flux surfaces. (b.) Illustration of cross section with m/n=1/1 and 2/1 magnetic islands developed on rational surfaces. Figure reproduced from [9]

nested flux surface topology of the ideal case. Tearing modes, however, can break the magnetic field lines and reconnect them to form small isolated nested flux surfaces within the overall topology called magnetic islands. An illustration of a nested flux surface topology and one with magnetic islands present is shown in 1.4. Low order modes, such as those with $m < 3$ and $n < 3$, tend to produce larger perturbations that can have global impact on the plasma.

The tokamak's $q(r)$ profile is beneficial for two reasons. First, the $q(r) = 2$ rational surface lies near mid-radius; and second, there is significant magnetic shear $\frac{r}{q}\frac{dq}{dr}$ from core to edge. If I_P were increased such that the $q(r) = 2$ surface expands towards the edge, the plasma can deform via external kink, and its proximity to the plasma edge enhances its interaction with vessel structures. Keeping the $q(r) = 2$ surface away from the plasma edge is necessary for avoiding external kink modes and disruptions. The magnetic shear is required for stabilizing pressure-driven instabilities like interchange and ballooning modes which can severely degrade confinement. These modes can be destabilized in any magnetic confinement configuration whose magnetic field has regions of "bad curvature", defined as having a radius of curvature which points into the confined plasma. Stability to interchange in a toroidal confinement system is characterized by the Mercier stability criterion [10]. A

convenient approximation for the Mercier criterion for the case of a circular cross section, high aspect ratio tokamak is given by

$$rB_T^2\left(\frac{q'}{q}\right)^2 + 8\mu_0 p'(1-q^2) > 0\ , \tag{1.5}$$

where $q' = \frac{dq}{dr}$ and $p' = \frac{dp}{dr}$ are the radial gradients of safety factor and plasma pressure, respectively. In order to support a negative pressure gradient without instability, the stabilizing magnetic shear (first term in 1.5) must be large enough to overcome the destabilizing pressure gradient (second term in 1.5). Even with a strong pressure gradient, the tokamak's $q(r) > 1$ profile satisfies this condition and allows for its good confinement properties. A similar $q(r)$ profile is used in essentially every tokamak, along with auxiliary heating and current drive systems to tailor the $q(r)$ profile, achieve higher plasma performance, and enhance stability [1].

An instability inherent to the tokamak configuration is the sawtooth instability, which gets its name from the sawtooth-like waveforms it produces on many diagnostics. Due to the core peaking of the electron temperature T_e and electron density n_e profiles, the plasma current density profile $J(r)$ will also tend towards a core-peaked structure. Since the resistivity of the plasma is proportional to $T_e^{-3/2}$ [4], the J in the core will continue to increase and drive the value of the core safety factor q_0 below 1. This small region with $q(r) < 1$ becomes unstable and releases its stored energy, acting to flatten the $T_e(r)$ and $J(r)$ profiles to return q_0 to a value greater than 1 [11]. This process will repeat as the sawtooth cycle, periodically gaining magnetic and thermal energy in the core and releasing it once reaching an unstable state. The sawtooth instability, being core localized, is usually minimally perturbative to the global stability of the plasma; but in a high performance tokamak it can significantly degrade confinement and even trigger disruptions by exciting other instabilities. The tokamak $q(r)$ profile will cross several major rational surfaces like

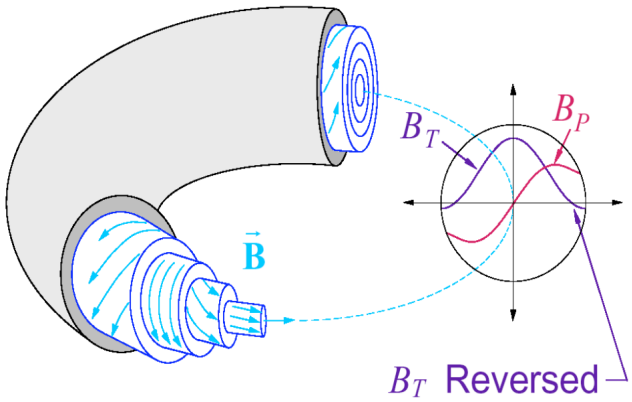

Figure 1.5: Illustration of RFP configuration. [figure courtesy of J. Sarff]

$q(r)$=1, 3/2, 2, 5/2, 3, etc.; and these rational surfaces can be sources of confinement-degrading instabilities.

1.2.2 The Reversed-Field Pinch

If a conducting shell surrounds the plasma edge, I_P can be increased without concern for external kink modes. If a large enough I_P is driven, a reversed-field pinch (RFP) configuration can be generated with a significantly different $q(r)$ profile [12]. In the RFP, both the B_P and the B_T are almost entirely supported by internal plasma currents. At steady state, the applied B_T from external coils is relatively small and is used primarily for control of the $q(r)$ profile near the plasma edge. The term "reversed-field" comes from the feature of the configuration where the B_T peaks in the core and reverses direction near the edge. An illustration of an RFP configuration is shown in 1.5.

The difference in $q(r)$ profile between the tokamak and the RFP can be seen in Figure 1.3. The gradient of $q(r)$ is smaller than the tokamak's, but since q is relatively small, the stabilizing magnetic shear $\frac{r}{q}\frac{dq}{dr}$ is strong enough to suppress ideal interchange modes and allow for good confinement. The RFP's energy confinement time is generally comparable to but lower than that of a tokamak with comparable size and magnetic field strength. In the

RFP, $q_0 \approx 0.2$ and decreases monotonically to $q_a \lesssim 0$ at the edge. Thus, the RFP contains a different set of rational surfaces compared to the tokamak, usually including $q(r)$ =1/5, 1/6, 1/7, etc. These rational surfaces also have relatively close radial spacing which leads to the RFP exhibiting its own sawtooth cycle with a different mechanism than the tokamak's. The sawtooth cycle in the RFP is caused by the growth and subsequent overlapping of the magnetic islands which lie on these rational surfaces. The overlapping of island chains leads to spontaneous reconnection events that convert significant poloidal magnetic flux into toroidal flux and drive particle energization due to the magnetic reconnection and current reorganization process.

1.2.3 The Ultra-Low Safety Factor Pinch

Between the tokamak and RFP operation regimes lies the ultra-low safety factor (ULq) plasma configuration with $0 < q(a) < 1$ which is poorly understood for several reasons. In toroidal pinch devices without active or passive stabilization of the plasma boundary, the ULq regime is inaccessible due to external kink instability and disruption when operating at $q_a < 2.5$. In devices stabilized by a conductive wall which were developed to support RFP research, it is observed that approaching the ULq regime from an RFP discharge by increasing the applied B_T results in a significant increase of fluctuation amplitudes and global plasma resistance [13] [8]. In Figure 1.3, it can be seen that this regime with $0 < q_a < 0.3$ has reduced magnetic shear which may be partially responsible for the degradation of energy confinement. Discharge properties for ULq plasmas with $0 < q_a < 0.3$ are otherwise similar to the RFP.

In devices that can drive significant B_T while also stabilizing the external kink instability, the ULq regime with $0.4 < q_a < 1$ is accessible with its own distinct properties. Magnetic shear in this regime is very low relative to the tokamak and RFP, and $q(r)$ is always less

than 1, which makes even a minimal pressure gradient in this configuration unstable to interchange modes. Energy confinement time in the ULq regime is significantly shorter than in the tokamak and RFP. The ULq configuration contains major rational surfaces which are not present in the tokamak or RFP and may include the $q(r)$=4/5, 3/4, 2/3, 3/5, 1/2, 2/5, and 1/3 surfaces. Discharge properties are highly dependent on the value of q_a and are strongly influenced by the formation of resonant modes on these rational surfaces. These helical perturbations grow to large amplitudes and are observed to spontaneously rotate toroidally. Fluctuation amplitudes are much stronger than those in the RFP and tokamak, and the amplitudes and spectra of these fluctuations are highly dependent on the value of q_a. $T_e(r)$ profiles tend to be relatively flat in ULq plasmas with some internal gradients appearing in specific cases [8].

In the Madison Symmetric Torus (MST), high bandwidth and high power 10 kHz feedback power supplies have been recently implemented which can deliver up to 120 loop volts to the plasma [14]. This allows for the sustainment of flat I_P and B_T waveforms for 20-40 ms throughout the ULq regime, which has not been possible is past experiments due to the high global resistance of ULq plasmas. This capability allows for steady sustainment of ULq discharges and an investigation of the anomalous ion heating.

1.3 Ion Heating in Magnetized Plasmas

Without auxiliary ion heating systems, T_i in an Ohmic-heated tokamak plasma is determined by the ion energy confinement properties of the plasma, the T_e, and the collisional coupling of electron thermal energy to the ions. Due to the large difference in mass between the ions and electrons, the electrons will directly absorb >99% of Ohmic input power, leaving only their weak collisional coupling to heat the ions. In order for ion-ion collisions to overcome their Coulomb repulsion and produce a significant rate of nuclear fusion reactions, high

T_i is required. The collisional coupling between electrons and ions can be increased by operating at high plasma density. However, there are density limits for these confinement configurations, and bremsstrahlung radiation losses are proportional to the square of the electron density [15]. This motivates the use of auxiliary ion heating systems in order to achieve fusion-relevant T_i. Auxiliary ion heating in tokamaks is primarily facilitated by neutral beam injection (NBI) or ion cyclotron resonance heating (ICRH).

In NBI systems, deuterium ions are electrostatically accelerated into a 10 keV to 1 MeV ion beam. This high energy, high current ion beam is then neutralized by charge exchange reactions with neutral gas to form a powerful neutral particle beam which can penetrate the tokamak's magnetic fields without deflection. These energetic neutrals are then ionized by collisions in the plasma and transfer their energy to the bulk plasma. Unfortunately, there is strong preferential deposition of NBI power to electrons over ions [4]. This, along with high energy NBI systems being complex and inefficient, motivates the research of alternative ion heating methods.

In ICRH systems, electromagnetic waves with frequency of order 10 MHz are launched by antennae outside the plasma edge and couple to the ions by a resonant interaction at a specific radial location. The ion cyclotron resonance frequency ω_{ci} is given by

$$\omega_{ci} = \frac{qB}{m_i} \tag{1.6}$$

where B is the magnetic field strength, q is the charge of the ion, and m_i is the ion mass. This technique efficiently couples heating power directly to the ions, but these high power RF systems are challenging to implement and maintain in close proximity to a high performance plasma. It can also be difficult in large, high density plasmas to efficiently transmit the RF waves to the desired resonance location [4]. Lack of an efficient method of ion heating for high performance plasmas remains a significant obstacle to achieving fusion energy.

Anomalous intrinsic ion heating is observed in the RFP regime which is not observed in the tokamak [16] [17] [18] [19]. In the RFP, there is a continuous ion heating which drives $T_i \geq T_e$ as well as impulsive heating events which cause significant increases in T_i within 100 μs after a sawtooth reconnection event. Studies of this ion heating have attempted to attribute it to viscous damping of flows [20] [21], damping of magnetic fluctuations with frequencies near ω_{ci} [22] [23] [24], and stochastic ion heating from strong electric field fluctuations [24]. In the case of viscous damping, bulk plasma flows are damped by the plasma viscosity, dissipating large scale flow energy as ion thermal energy. In the case of ion cyclotron resonance damping, high frequency magnetic fluctuations are generated as the high amplitude, large scale, low frequency fluctuations produced directly from the magnetic reconnection event cascade their fluctuation energy to higher frequencies and smaller scales. When this fluctuation cascade reaches ω_{ci} of an ion species, the electric field component of the fluctuation can accelerate ions, transferring fluctuation energy to ion gyro motion and thermal energy. Stochastic heating can occur when small scale electric field fluctuations are strong enough to drive chaotic ion motion and directly heat the ions. There is strong evidence that cyclotron resonance damping or stochastic heating is responsible for the ion heating in the RFP. Evidence for significant heating from viscous damping is weak, and there is no conclusive evidence to determine the contributions from cyclotron resonance damping and stochastic heating.

Anomalous ion heating is also observed in the ULq plasma regime, but it has received little research focus to understand its source and dependence on discharge parameters [25]. In sustained conditions, impurity temperatures in ULq plasmas are nearly constant in time and no heating events are observed. While the RFP sawtooth ion heating has a clear source of energy being the significant magnetic energy lost during reconnection events, the ULq plasmas exhibit no distinct events or change in magnetic energy.

1.4 Summary of Research Objectives, Observations, and Results

The objectives of this work are to experimentally characterize ULq plasmas in MST, focusing on the anomalous impurity ion heating in plasmas with edge safety factor having a range of $0.4 \leq q_a \leq 0.9$. An attempt is then by made to use the information to explain the observations with known ion heating mechanisms. The information is obtained by performing several single parameter scans in ULq discharges while measuring magnetic fluctuations, electron density fluctuations, plasma potential fluctuations, and line-averaged impurity ion temperatures $\bar{T}_z$. These parameter scans include a scan of q_a at fixed B_T and $\bar{n}_e$, a scan of I_P and B_T at fixed q_a and $\bar{n}_e$, and a scan of $\bar{n}_e$ at fixed q_a and B_T. The diagnostics used for this work include magnetic pickup coil arrays at the plasma edge, an insertable probe containing an array of magnetic pickup coils, an insertable probe containing an array of capacitive plasma potential sensors, multi-chord infrared laser interferometry, and multi-chord passive Doppler spectroscopy.

The ULq discharges require high neutral fueling rates and loop voltages to achieve reproducible startup and sustainment. They generally exhibit high global electrical resistance, large fluctuation amplitudes, high toroidal rotation velocities, and anomalously high impurity $\bar{T}_z$. Impurity (B-IV 282.2 nm) $\bar{T}_z$ is observed as high as 400 eV, or up to approximately 3× the electron temperature. $\bar{T}_z$ has a strong dependence on q_a and generally increases as q_a decreases. $\bar{T}_z$ is highest at $q_a \approx 0.6$. At $q_a \approx 0.55$, there is an abrupt decrease in fluctuation amplitudes, $\bar{T}_z$, global plasma resistance. $\bar{T}_z$ also has a strong dependence on line-averaged electron density $\bar{n}_e$ where a factor of 4× decrease in $\bar{n}_e$ causes a factor of ∼10× increase in $\bar{T}_z$. Global plasma resistance has a minimum value when $\bar{n}_e \approx 5 \times 10^{18}\ m^{-3}$ such that resistance increases significantly as $\bar{n}_e$ increases or decreases from this value. At a fixed q_a value, $\bar{T}_z$ increases linearly as B_T and I_P are increased while Ohmic input power increases

quadratically and global plasma resistance remains nearly constant.

Magnetic, plasma potential, and $\bar{n}_e$ fluctuations are analyzed in detail for three different q_a values of 0.7, 0.65, and 0.55. These q_a cases are selected due to their significant change in discharge behavior with small changes in I_P. Strong plasma potential fluctuations and radially localized magnetic fluctuations are correlated with the amplitude and rotation of toroidal modes. Increases in fluctuation frequencies and amplitudes are associated with increases in $\bar{T}_z$, which all depend strongly on q_a and $\bar{n}_e$. Broadband radial electric field fluctuations $\tilde{E}_r$ are observed with RMS amplitudes up to 14 kV/m.

A power balance for the B-IV impurities is estimated to determine the heating power necessary to sustain the observed $\bar{T}_z$. The impurity heating power estimate for ion cyclotron resonance damping and viscous dissipation are found to be much lower than the required heating power. An estimate of the stochastic heating power due to broadband $\tilde{E}_r$ is consistent with the required heating power. Results suggest that impurity heating is caused by stochastic heating via high amplitude, broadband, short coherence length $\tilde{E}_r$ associated with the rotation of resonant helical modes.

1.5 Outline of Thesis

Chapter 2 summarizes anomalous ion heating observed in the solar corona and research on ion heating in the reversed-field pinch. It then describes past experimental and computational work on the ULq regime and the observations of anomalous ion heating. It concludes with a discussion of the possible ion heating mechanisms in ULq plasmas including ion cyclotron resonance damping, stochastic heating, and viscous dissipation.

Chapter 3 describes the Madison Symmetric Torus where these experiments are performed and the diagnostics used in this work. The diagnostics include several arrays of wall-mounted magnetic pickup coils, an insertable probe with magnetic pickup coils, an in-

sertable probe with capacitive plasma potential sensors, a far-infrared interferometer system for electron density measurements, and a spectrometer for impurity temperature measurements.

Chapter 4 describes the general observations made while performing these ULq experiments and how they compare to tokamak and reversed-field pinch plasmas. This includes a discussion of plasma startup techniques, neutral fueling requirements, global energy confinement, mode activity, equilibrium properties, and ion heating.

Chapter 5 reports on the experiments performed to characterize the variation in fluctuations and impurity temperature with discharge parameters. It begins with presentation and discussion of the data from parameter scans of the ULq regime including a scan of q_a, a scan of average plasma density, and a scan of I_P and B_T at a fixed q_a. This is followed by magnetic fluctuation and electron density fluctuation analysis of three specific q_a cases of interest which are selected due to their significant change in discharge behavior with relatively small changes in I_P. Finally, plasma potential and radial electric field fluctuation measurements are presented.

Chapter 6 evaluates the possible ion heating mechanisms in the ULq plasmas. It begins with a power balance for the boron impurities in order to estimate the heating power necessary to sustain the observed impurity temperatures. Then, the heating power from each of the mechanisms is estimated to determine which of them may contribute significant heating power to the boron impurities. The mechanisms evaluated include ion cyclotron resonance damping, stochastic heating, and viscous dissipation.

Chapter 7 provides a summary of the observations and conclusions from this work and discusses suggestions for future work on the impurity heating and properties of ULq plasmas.

Chapter 2

Background and Motivation

2.1 Ion Heating in the Solar Corona

One motivation for studying the physics of non-collisional ion heating in magnetized plasmas is to understand the heating observed in the solar corona. Ion temperatures in the diffuse solar corona are observed to be $\sim$100$\times$ the temperature measured at the photosphere, the relatively dense surface of the sun [26] [27] [28]. This observation is puzzling due to the fact that fusion reactions are produced primarily in the core, which indicates that there is some other heating mechanism active in the corona. At around 1000 km above the sun's surface, ion temperatures abruptly increase from about 0.1 eV to 10 eV and continue to steadily increase to about 100 eV at a distance of 3 solar radii. Heavier ions tend to be significantly hotter than the protons. Oxygen ions have been observed as high as 10 keV and exhibit anisotropy with $T_\perp > T_\parallel$, where perpendicular and parallel refer to the degree of freedom with respect the background magnetic field. Some leading theories for the heating mechanisms responsible include cyclotron damping of Alfven fluctuations driven near the surface, stochastic heating via turbulent dissipation of fluctuations, and direct acceleration from magnetic reconnection events. Conclusive evidence to support these heating mecha-

nisms has not yet been established, and the coronal heating problem remains an area of active research.

2.2 Ion Heating Studies of the RFP

One of the earliest examples of anomalous ion heating in toroidal pinches was observed in the ZETA shell-stabilized toroidal pinch experiment where the RFP configuration was discovered. In some ZETA discharges, impurity temperatures T_z could be hundreds of eV while T_e was always less than 100 eV [29]. This was unexpected in an Ohmic-heated plasma, and an anomalous ion heating driven by electrostatic fluctuations was proposed.

In the dedicated RFP experiments that followed, ZT-1 [30] and ZT-40 [31], diagnostic capabilities and pulse durations were expanded which led to better T_z measurements. Similar anomalously high impurity T_z was also observed. A current-driven instability which heated ions via cyclotron damping was proposed, but evidence to differentiate it from other heating mechanisms was not conclusive.

Work performed on MST has made substantial contributions to the understanding of the RFP anomalous ion heating which has been observed since early MST operations [32]. The ion heating in the RFP is a result of closely spaced magnetic island structures that undergo large scale magnetic reconnection events and facilitate current reorganization. This ion heating is fast ($\sim$100 μs), powerful (of order MW), and occurs in bursts which following a sawtooth crash. An example of the rise in impurity T_z and its correlation with the plasma's magnetic energy is shown in 2.1. The sawtooth crash results in the sudden interaction of low-n $m = 1$ tearing modes with long spatial wavelength. Due to the mode's toroidal rotation, this perturbation will rotate past pickup coils and be measured as a fluctuation at $\sim$10 kHz with its peak in amplitude occurring at the sawtooth crash. For example, an $n = 7$ mode with rotation velocity $v_\phi = 20$ km/s would produce a fluctuation with frequency $f = \frac{nv_\phi}{2\pi R} \approx 15$

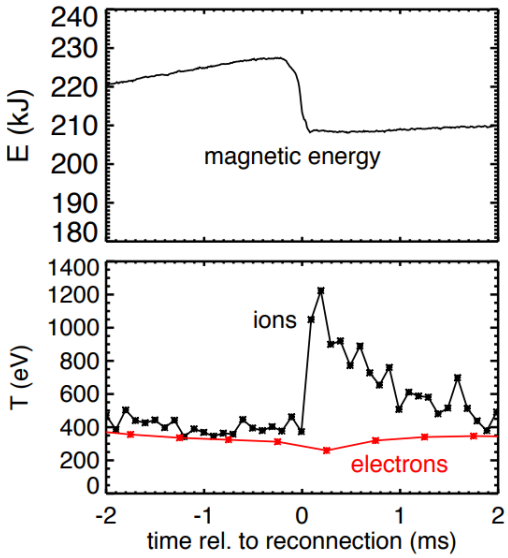

Figure 2.1: Carbon (C^{6+}) ion temperature, electron temperature, and magnetic energy evolution during a sawtooth event in the RFP. Figure reproduced from [33]

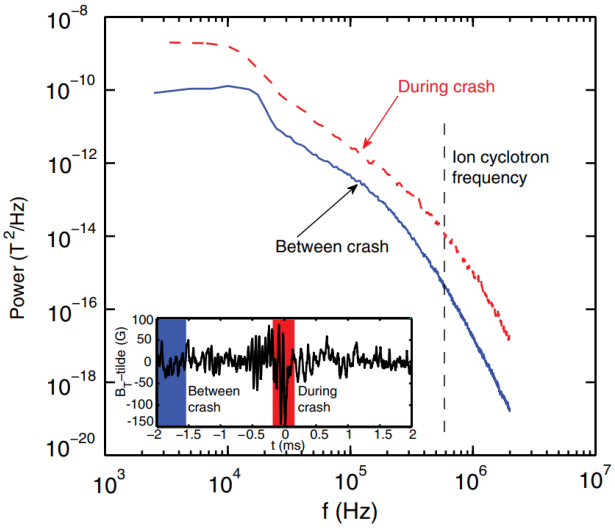

Figure 2.2: RFP B_T fluctuation spectrum before and during a sawtooth event. Figure reproduced from [34]

kHz on a single coil. Immediately after the reconnection event, the fluctuation amplitude at this relatively low frequency decay as the fluctuation energy cascades to progressively higher frequencies until it dissipates. An example of B_T fluctuation spectra from the edge of an RFP discharge before and during a sawtooth event is shown in 2.2. The heating mechanism in the RFP sawtooth may be different from the one responsible for ion heating observed

in the ULq regime which sustains nearly constant T_z and does not exhibit a correlated loss of magnetic energy; however, it is the only well-characterized anomalous ion heating in a regime comparable to ULq ion heating and will be reviewed here briefly. Note that ion heating has been observed in several dedicated reconnection experiments [35] [36] [37] as well as merging-compression experiments in the MAST spherical tokamak [38], but these will not be discussed since signatures of strong reconnection events are not observed in steady ULq plasmas.

For the RFP, it has been shown that significant change in the plasma's stored magnetic energy is required in order to observe the ion heating and that not all sawtooth events result in ion heating. Three distinct types of sawtooth events have been observed in the RFP [19]. These are described as $m = 0$ bursts which are localized in the edge region, m=1 bursts which are localized to the core, and global events which involve both the $m = 1$ and $m = 0$ bursts which are the most common. The simultaneous $m = 0$ and $m = 1$ bursts result in the largest drop in magnetic energy and the highest amount of ion heating which appears globally distributed. m=0 bursts result in a smaller drop in magnetic energy and ion heating is only observed near the B_T reversal surface. $m = 1$ bursts alone result in a minimal change in magnetic energy and no significant ion heating. The isolated $m = 1$ bursts can occur infrequently in the standard RFP but become more common if q_a is raised above zero, eliminating B_T reversal and approaching the ULq regime. These observations indicate that the equilibrium magnetic field of the RFP plasma is the source of energy, and the ion heating is linked to the growth of the $m = 0$ mode [19].

Out of the magnetic energy that is lost during a sawtooth event, as much as 50% can be transferred to ion thermal energy. This was defined as the ion heating efficiency and calculated with

$$\epsilon = \frac{\Delta E_{\text{therm}}}{\Delta E_{\text{mag}}} = \frac{\frac{3}{2}\int nk\Delta T\, dV}{\int \frac{\Delta B^2}{2\mu_0}\, dV}\,, \tag{2.1}$$

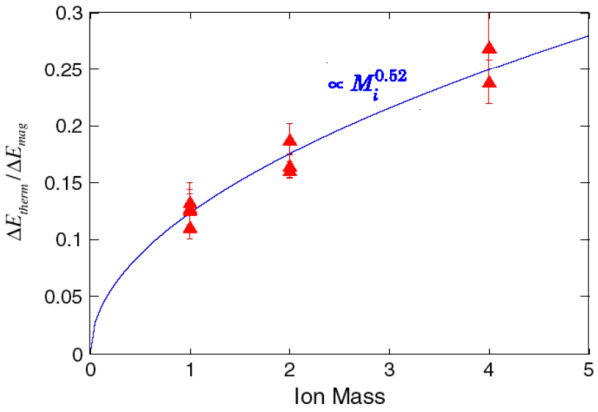

Figure 2.3: Dependence of ion heating efficiency on ion mass for three different majority species: hydrogen, deuterium, and helium. Figure reproduced from [24]

where n is the majority ion density, k is the Boltzmann constant, ΔT_i is the change in ion temperature during the heating, ΔB is the change in magnetic field strength, μ_0 is the permeability of free space, and the integration is over the plasma volume dV. The heating efficiency of the majority ions was found to have a dependence on the mass of the majority species. Majority species T_i was measured with a Rutherford scattering diagnostic and used to calculate the ϵ for hydrogen, deuterium, and helium working gases. For similar discharges, a dependence of $\epsilon \propto m^{\frac{1}{2}}$ was observed with ϵ values of 10%, 17%, and 25% for hydrogen, deuterium, and helium working gases respectively. Data from these experiments in shown in 2.3. The ion heating efficiency was only considered for the majority species since impurities make up ~1% of the plasma composition and are insignificant to the total energy transfer. For the majority species a density dependence of $\Delta T_i \propto \frac{1}{n}$ was observed, suggesting that the energy transfer to the ions is independent of density [24].

Although they do not absorb a significant portion of the total magnetic energy converted, impurity ΔT_z is generally greater than or equal to the the majority ΔT_i during the RFP sawtooth, and T_z is often greater than or equal to T_i between sawtooth events. Spatially localized measurements of fully ionized carbon impurities were facilitated by the charge exchange recombination spectroscopy (CHERS) diagnostic observing neutral beam

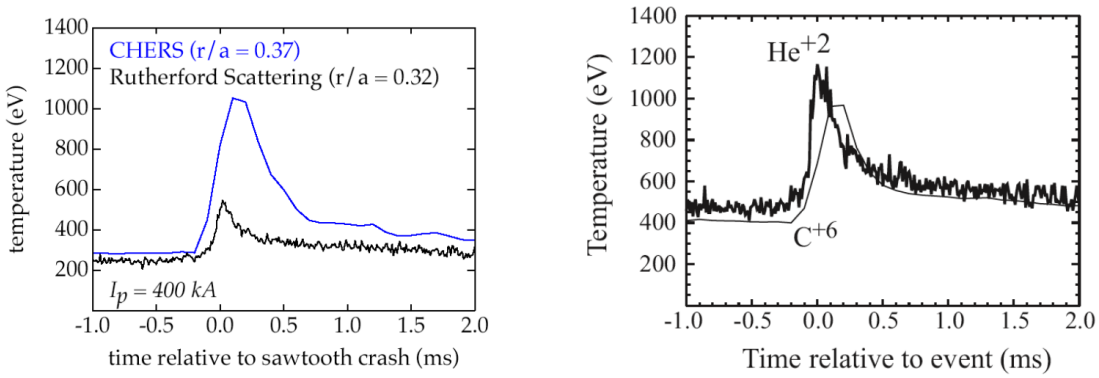

Figure 2.4: (Left) Carbon C^{6+} and deuterium ion temperature during a sawtooth event. (Right) C^{6+} and helium ion temperatures during a sawtooth event. Impurity temperatures are significantly greater than the majority when deuterium is the working gas, but comparable when using helium. Figures reproduced from [19]

induced line emissions. By comparing C^{6+} T_z measurements to simultaneous majority T_i measurements, it was shown that $T_z \approx T_i$ when operating with helium and $T_z \approx 2 \times T_i$ when operating with deuterium. Data from these experiments is shown in 2.4. A dependence of T_z on plasma density was also observed for the carbon impurities, but this density dependence varies depending on the radial location of the measurement. Generally, the core impurity T_z does not change significantly when density is varied, but an inverse density dependence grows stronger as the B_T reversal surface is approached towards the plasma edge. It was not clear if this is density dependence variation with radius is due to the ion heating weakening towards the edge or due to an anisotropy in the ion heating mechanism. Although the T_z measurements are spatially localized by intersection of the neutral beam and spectrometer line of sight, the Doppler broadening measurement is only sensitive to particle motion parallel to the line of sight. Since all of the vertical view chords are oriented tangential to the flux surfaces across the plasma radius, the core-intersecting chord is only sensitive to particle motion perpendicular to the magnetic field, and the edge-intersecting chord is only sensitive to the particle motion parallel to the magnetic field. Thus, the core measurement samples the perpendicular ion temperature $T_\perp$, the edge measurement samples the parallel

ion temperature $T_{\|}$, and locations between the core and edge reflect some combination of both $T_{\perp}$ and $T_{\|}$ [39].

The anisotropy of the RFP impurity ion heating was investigated by comparing passive measurements from toroidally oriented and vertical tangential lines of sight [39]. With passive spectroscopy using line-integrated measurements, spatial localization of T_z is determined by the emission profile of the observed impurity charge state. The species observed was C^{+4} which should have an emission shell localized to the mid-radius region. In this experiment, $T_{\|}$ was observed to be approximately equal to $T_{\perp}$ throughout the discharge and during sawtooth events. This suggested that the ion heating mechanism is isotropic when averaged over the collection line of sight, but this could not exclude local anisotropy.

The heating anisotropy was further investigated using spatially localized ChERS measurements of fully ionized carbon [40]. Measurements in the RFP plasma core showed that there is anisotropic heating driven during the sawtooth event with $T_{\perp} > T_{\|}$ for ~2 ms, after which the $T_{\perp}$ and $T_{\|}$ equilibrate. The sawtooth-driven change in perpendicular temperature $\Delta T_{\perp}$ was observed to be independent of plasma density, but $\Delta T_{\|}$ decreased with increasing density. This trend was seen at all locations across the plasma radius. These observations are consistent with a proposed model of perpendicular ion heating followed by collisional isotropization. The $T_{\|}$ dependence on majority density can be explained by the cooler deuterium ions inhibiting the equilibration of the C^{+6} $T_{\|}$ and $T_{\perp}$. Another possible explanation is that the plasma impurity concentration decreases with increasing plasma density, decreasing the rate of impurity T_z isotropization.

Impurity ions in RFP plasmas generally have higher T_z than the majority T_i during the periods away from sawtooth events, but the proposed model can only reproduce this feature by the addition of a continuous heating mechanism with power equal to ~30% of the sawtooth heating power. However, if the continuous heating mechanism preferentially

heats in the perpendicular degree of freedom, the model predicts a steady temperature anisotropy which was not observed experimentally [40]. For the sawtooth event heating, it was concluded that the impurities are most likely only directly heated in their perpendicular degree of freedom, but the apparent isotropy of the continuous heating mechanism has not been explained.

2.3 Past Experimental and Computational Work on ULq

ULq plasmas were first observed experimentally in ZETA [41]. These discharges were highly unstable and could not be sustained for any significant duration. ULq plasmas were first sustained in REPUTE-1 [42] and followed soon after by experiments in TORIUT-6 [43] [44]. These discharges were sustained for several milliseconds; however, power supply limitations prevented discharge parameters from being held constant for more than 1 ms. ULq plasmas in TORIUT-6 exhibited hollow current density profiles with $q(r)$ minima located between the mid-radius and edge. These plasmas were very sensitive to impurity concentrations, and carbonization of the vessel wall resulted in a $\sim$50% decrease in global plasma resistance.

In REPUTE-1 discharges, anomalously high plasma resistivity and T_z were observed for plasmas with $140 \leq I_P \leq 300$ kA and $n_e = 3 \times 10^{19}\ m^{-3}$ [13]. The plasma resistance was described as anomalous due to it being about 100$\times$ greater than the resistance calculated with the measured $T_e \approx 100$ eV. The global plasma resistance was inversely related to the applied B_T, a scaling which was also observed in other devices with different dimensions and B_T. Soft x-ray measurements suggested the presence of a high energy tail in the electron energy distribution, but the diagnostic could not differentiate between emissions sourced from the plasma and wall impact. Oxygen impurity T_z measured by O^{+4} Doppler spectroscopy were as high as 600 eV [25]. Majority ion temperatures of $T_i \approx 100$ eV for hydrogen and $T_i \approx 150$ eV for deuterium plasmas were measured by the time-of-flight method and were

usually significantly lower than the impurity temperature. The O^{+4} T_z was correlated with the amplitude of B_P fluctuations, but there was no clear correlation to the majority T_i. An inverse dependence of impurity T_z on plasma density was observed and attributed to a change in the rate of cooling of hot impurity ions on the cooler majority species. A stochastic ion heating and power balance model was proposed to explain why the oxygen T_z exceeds the majority T_i and why the heating is strong even though the magnetic fluctuation frequencies are much less than the ion cyclotron frequencies. This model reasonably explained the observations if the impurity energy confinement time is comparable to the temperature equilibration time between impurity and majority ions.

ULq experiments were also performed in HBTX-1C, a small conducting shell stabilized toroidal pinch device [45]. Resistive wall modes growing on the time scale of the resistive wall time τ_{wall} of the conducting shell were observed in both ULq and RFP plasmas. In both regimes, the growth of these modes to large amplitude limited the discharge durations. Mode rotation velocities appeared significantly greater in ULq discharges than in RFP. ULq discharges exhibited a feature where the I_P would be limited to a particular value despite increasing the applied loop voltage. These I_P values corresponded to q_a having major rational values, and these I_P limits could only be exceeded by applying significantly larger loop voltage than the voltage needed to maintain I_P. In ULq discharges, the resistive wall modes could be suppressed by maintaining the value of the q_a within 10% above these rational values. The I_P limits observed in low-q and ULq regimes were correlated to large amplitude resonant modes that grew faster than τ_{wall}. Their growth resulted in minor plasma current collapse or relaxation events, but not to a major disruption. These fast growing resonant modes together with the resistive wall modes imposed a narrow range of values of q_a near the major rational values for stable ULq operation. Global plasma resistivity was higher in ULq plasmas than in RFPs, and it was suggested that this may be related to a higher rate of

particle recycling. Plasma current fluctuations similar to the quasi-continuous sawtooth-like activity seen in low-q tokamak discharges were present in ULq plasmas but not in RFPs.

More recently, ULq discharges with greater B_T have been studied in the RFX-mod device [8]. RFX-mod is a significantly larger toroidal pinch that maintains global plasma stability by using an array of electromagnet coils and radial field B_R sensing coils outside a thin copper shell which surrounds the plasma boundary. The system consists of 192 independently driven saddle coils which mimics the passive stabilization of a thick conducting shell. This is achieved by feedback-controlling the coil currents needed to cancel out the measured B_R at the plasma boundary. Similar to earlier experiments, these ULq discharges exhibited a tendency to relax towards a nearby q_a value, and small changes in q_a could drive a transition from a quiescent state to exhibiting steady sawtooth-like fluctuations. The magnetic fluctuation spectrum was generally dominated by a single helicity, and modes tended to spontaneously rotate toroidally. Wall locking events were not typically observed, even without feedback control of the plasma boundary coils.

These RFX-mod experiments were complemented by computational work using the visco-resistive, zero pressure, 3-D cylindrical MHD code SpeCyl [46]. The MHD behavior was characterized by sweeping through the entire ULq regime by slowly ramping B_T to drive from $q_a = 0$ to $q_a = 0.8$ and back. The results, displayed in 2.5, show that as q_a approaches a major rational value, an $m = 1$ mode is strongly excited with the dominant n component satisfying $q(a) = m/n$. Near $q(a) = \frac{3}{5}, \frac{2}{3}, \frac{3}{4}$ activity is dominated by $m > 1$ modes. Ramping beyond a major rational $q(a)$ value results in a flattening of the $q(r)$ profile and fluctuations transition from a strong $m = 1$ to relatively weak $m > 1$ modes. Contour plots of the helical flux function for the dominant modes plotted over the Poincare map at select instances of the q_a ramp simulation are shown in 2.6. These plots suggest the formation of large island structures when the spectrum is dominated by a single mode, with the topology strongly

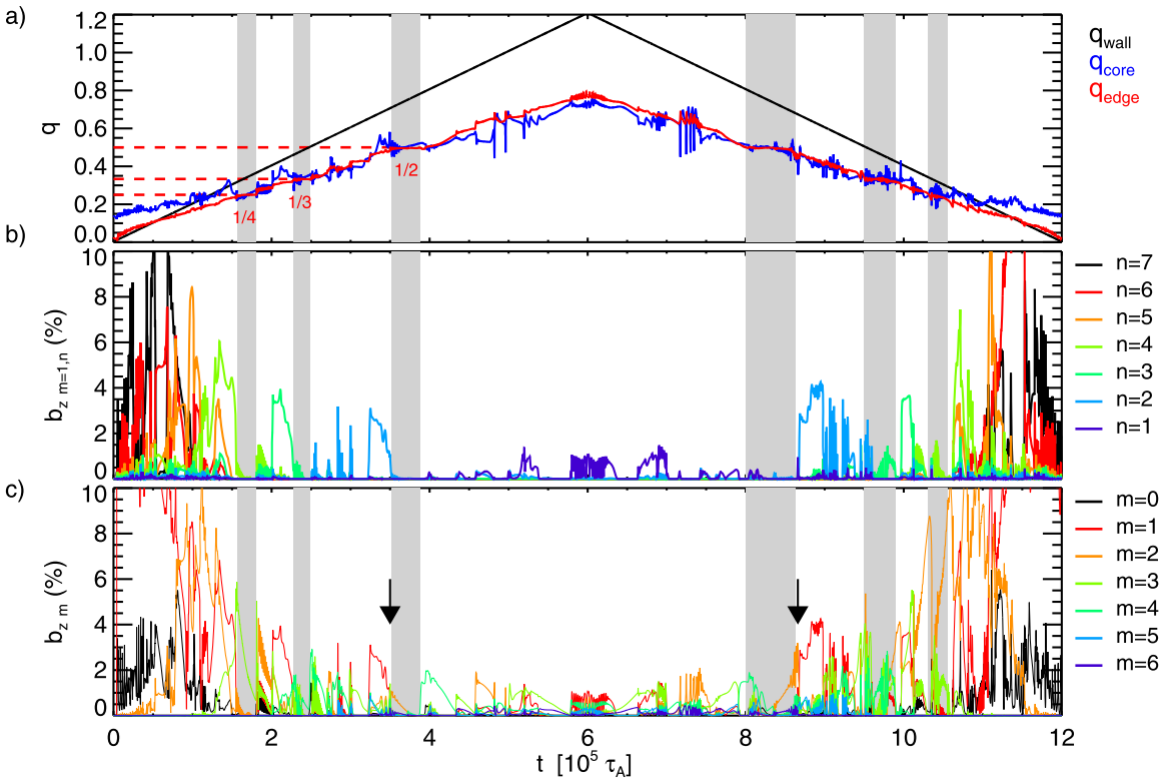

Figure 2.5: ULq ramp-up and ramp-down simulation. (a.) q_{wall}, q_{core}, and q_{edge} evolution. (b.) Amplitudes of $m = 1$ component for several n. (c.) Amplitudes of several m summed over all n. Figure reproduced from [46]

dependent on q_a.

A similar ramp of q_a was performed in a single RFX-mod discharge and shown in 2.7 to have very similar behavior to the simulations. The plateaus in q_a, shaded in gray, correspond to the stage with low mode amplitudes, and single mode amplitudes dominate just before the plateau. Notice that in the $q(a) \approx 0.66$ region, there are significant fluctuations in $q(a)$, rather than a plateau, and oscillations in the $n = 3$ and $m = 0, 2$. Generally, a single dominant mode was observed away from the plateaus with its structure dependent on $q(a)$. In simulation, mode amplitudes tend to decrease as $q(a)$ increases, but the experiment did not show a significant trend in mode amplitudes.

Discharges sustained at specific q_a values exhibited an oscillatory behavior of both the mode amplitude and $q(r)$ profile. The value of q_a also strongly influenced the confinement

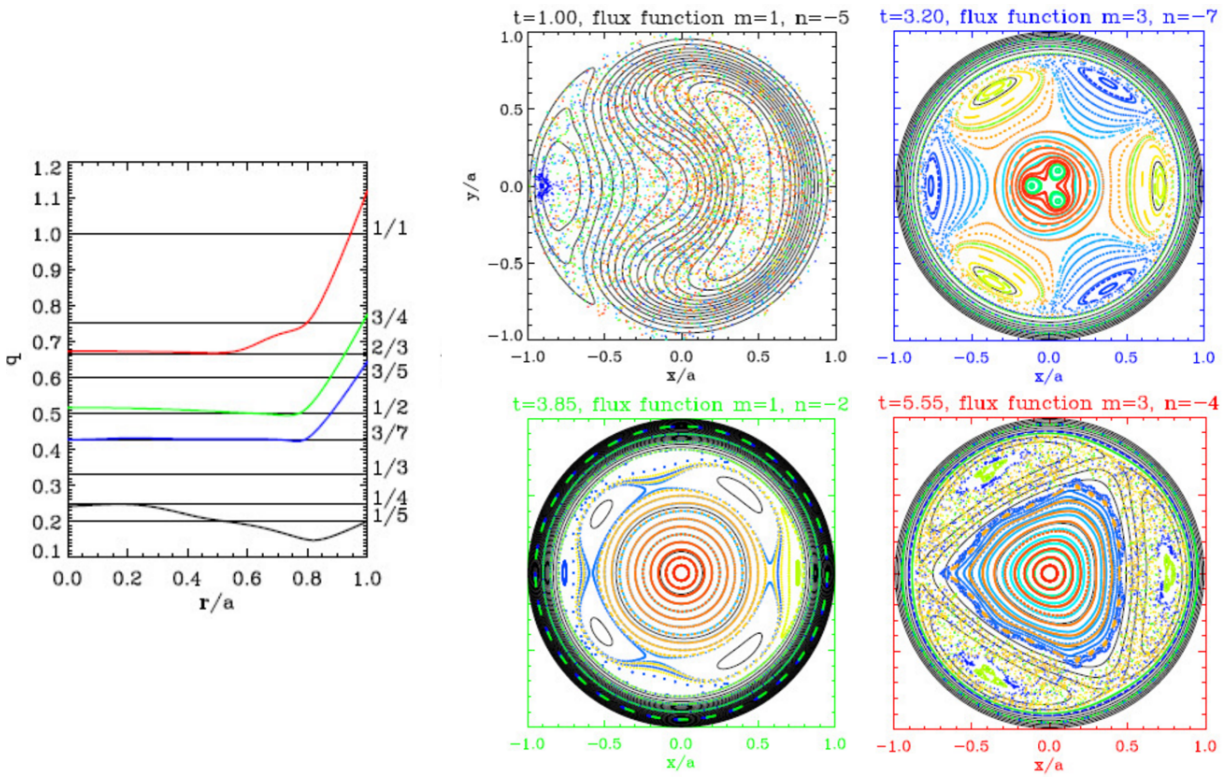

Figure 2.6: (Left) $q(r)$ profiles at time points from the $q(a)$ ramp simulation. (Right) Helical flux function contours plotted over the Poincare plots from the simulation. The helical flux contours are plotted for only the dominant helicity at each of the 4 time points. Figure reproduced from [8]

properties of the configurations which resulted in either flattened $T_e(r)$ profiles or significant radial structure when activity was dominated by a single helicity mode. Thomson scattering measurements of $T_e(r)$ profiles are shown in 2.8 for several different q_a discharges. In RFX-mod ULq discharges, no sudden change in confinement properties at high density was observed while the tokamak and RFP discharges exhibited a sudden change near the empirical Greenwald limit. Unfortunately, ion temperature measurements were not available for these ULq experiments in RFX-mod

Simulations of MST ULq plasmas in toroidal geometry are currently being developed using the NIMROD nonlinear visco-resistive MHD code [47] [48]. In these simulations, density and temperature evolution are incorporated by self-consistently computing Ohmic heating and anisotropic thermal transport, which is a significant improvement on previous

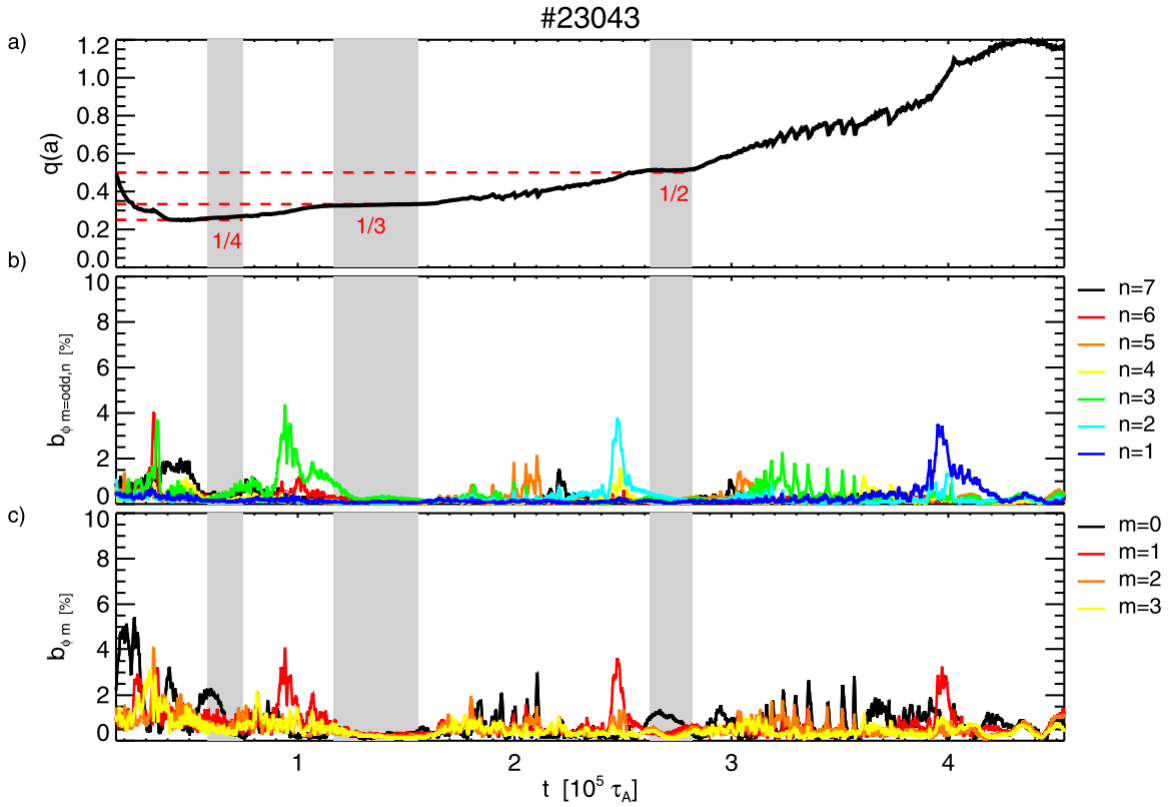

Figure 2.7: q_a ramp experiment in RFX-mod. (a.) q_a evolution. (b.) Amplitudes of several n modes. (c.) Amplitudes of several m modes. Figure reproduced from [8]

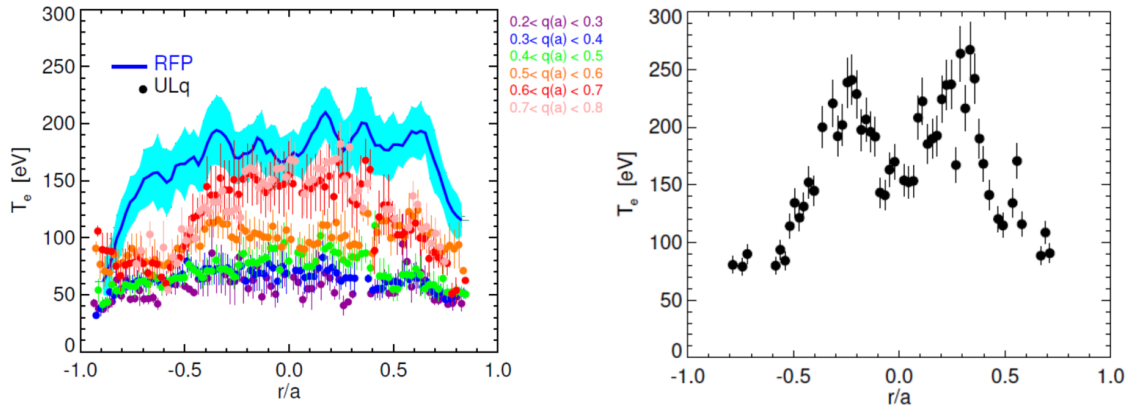

Figure 2.8: (Left) $T_e(r)$ profiles from ULq discharges in RFX-mod for several different q_a. (Right) A lower density discharge dominated by m/n=2/3 mode which shows significant gradients in T_e Figures reproduced from [8]

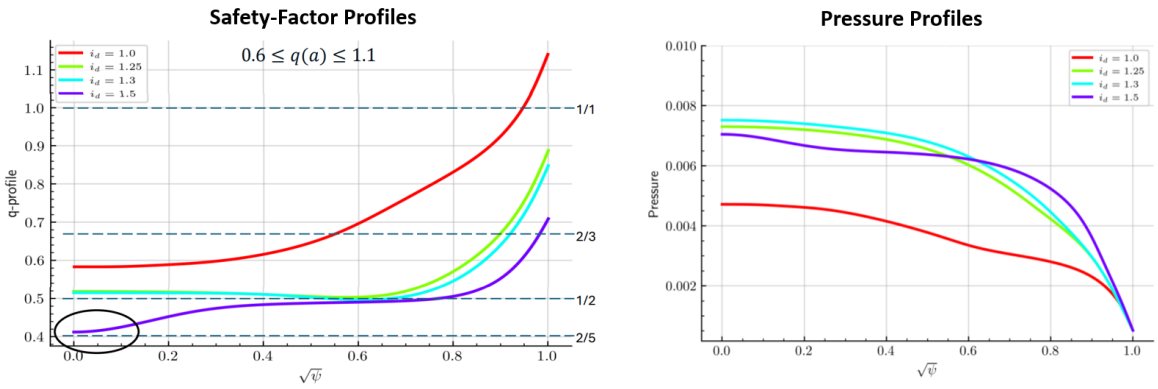

Figure 2.9: (Left) $q(r)$ profiles from ULq discharge simulations in NIMROD. (Right) Pressure profiles from the same simulations. An abrupt shift of q_0 to $q_0 = 2/5$ is circled, and this feature will be relevant to experimental results presented in Chapter 5. Figure reproduced from [47]

computational work on the ULq regime. Initial results show flattening of the $q(r)$ profile near major rational values along with local minima in $q(r)$ in the core or near the edge which strongly depends on q_a. Plots of some $q(r)$ and pressure profiles from these simulations are shown in 2.9. These non-dimensional simulations are being modified to use Braginskii transport coefficients and SI units to provide a direct comparison experimental observations. These simulations will complement the experimental work in MST and help provide a better understanding of the dynamics and unique transport properties of the ULq regime.

2.4 Potential Ion Heating Mechanisms

2.4.1 Ion Cyclotron Resonance Damping

One mechanism believed to be at least partially responsible for the anomalous ion heating in the RFP [22] [39] [33] and the solar corona [27] [28] is ion cyclotron resonance (ICR) damping of magnetic fluctuations. The ICR damping theory for RFP anomalous ion heating posits that the energy from large amplitude tearing-mode-driven magnetic fluctuations at 10's of kHz cascades to higher frequencies and smaller wavelengths, and these fluctuations

experience significant dissipation when they reach cyclotron frequencies at 100's of kHz for impurities and 1-2 MHz for deuterium at typical RFP parameters in MST. Given the strong magnetic fluctuations observed in ULq plasmas, a natural starting point for identifying an ion heating mechanism is to evaluate the potential heating from ICR damping.

In the RFP, the magnetic fluctuation amplitudes at the ω_{ci} of the majority species were found to be insufficient to explain the heating rates through ICR damping alone. However, the ICR heating rates for impurities were found to be consistent with observations. The model was extended to include thermal effects on the damping as well as collisional isotropization and equilibration of impurities with majority species [22]. This model was used to show that the impurities, having much lower cyclotron frequencies where the fluctuation amplitudes are higher, are strongly heated and can collisionally couple heating power to the majority ions which is consistent with the observations in the RFP.

Waves with a left-hand polarized elliptical or circular electric field component can couple to ion gyro motion when the resonance condition

$$\omega - \omega_{ci} = \vec{k} \cdot \vec{v} \tag{2.2}$$

is satisfied, where ω is the frequency of the wave, $\vec{k}$ is the wavevector of the wave, ω_{ci} is the ion cyclotron frequency, and $\vec{v}$ is the ion velocity. This coupling requires that part of the wave electric field is perpendicular to the equilibrium field $\vec{B}_0$, such that the electric field resonates with the ion gyromotion perpendicular to $\vec{B}_0$. For magnetic fluctuations with frequencies near ω_{ci} of an ion species, the damping rate γ is used to calculate the energy dissipation rate using the equation

$$\frac{dE}{dt} = \int \gamma(\omega) E(\omega) d\omega = \int \gamma(\omega) \frac{\tilde{B}^2(\omega)}{8\pi} d\omega \tag{2.3}$$

where E is the wave energy, ω is the frequency, and $\tilde{B}$ is the magnetic fluctuation amplitude. In this simple model, it is assumed that the wave's electric field is entirely left-hand polarized.

For waves in a cold isotropic plasma in the weak damping regime ($\gamma << \omega$), the damping rate can be approximated by

$$\gamma = \frac{\pi}{8}\omega_{pi}^2 \frac{1}{k_\parallel v_\parallel} \exp\left[-\frac{(\omega - \omega_{ci})^2}{2k_\parallel^2 v_\parallel^2}\right] \tag{2.4}$$

where ω_{pi} is the ion plasma frequency, $k_\parallel$ is the component of the wavevector parallel to $\vec{B}_0$, and $v_\parallel$ is the ion velocity parallel to $\vec{B}_0$ [22]. The plasma ion frequency for an impurity is defined as

$$\omega_{pi} = \sqrt{\frac{n_z Z^2 e^2}{m_i \epsilon_0}} \tag{2.5}$$

where n_z is the species number density, Z is the species charge, m_z is the mass of the impurity, e is the elementary charge, and ϵ_0 is the permittivity of free space.

By estimating γ and integrating over the measured magnetic fluctuation spectrum, an estimate of the potential heating power density from ICR damping can be obtained. This simple model will overestimate the ICR damping, but it can be used to determine an upper limit to the ICR heating power based on measured magnetic fluctuation amplitudes. If the overestimated heating power is insufficient to support the observed ion temperatures, then ICR damping can be ruled out as a dominant heating mechanism; and if the ICR heating power estimate is comparable to the required heating power, then more sophisticated modeling is warranted.

2.4.2 Stochastic Heating

Stochastic heating refers to any heating model where ions gain thermal energy by electric field fluctuations driving chaotic motion. Stochastic heating mechanisms have been proposed to explain ion heating observed in the Caltech Encore toroidal device [49], in the magnetopause [50], in the RFP sawtooth [24], and in ULq plasmas in REPUTE-1 [25].

Experimental evidence and modeling of stochastic ion heating due to large amplitude drift waves in a tokamak is described in [51]. When the amplitude of the potential and electric field fluctuations is high enough, the guiding center approximation for ion motion breaks down and the orbits become chaotic. In this model, stochastic heating becomes possible when the ion displacement due to polarization drift becomes comparable to the perpendicular wavelength of the wave. This threshold is defined as

$$\Phi_0 > \frac{qB_0^2}{k_\perp^2 m_i} \quad , \tag{2.6}$$

where Φ_0 is the peak potential amplitude of the wave, B_0 is the equilibrium magnetic field, q is the charge of the ion, $k_\perp$ is the perpendicular wavenumber of the drift wave, and m_i is the mass of the ion. Numerical simulations are required in order to predict a heating rate or heating power density in specific conditions using this model, but experiments and modeling showed that ion thermal energies could reach up to 50% of $k_B\Phi_0$.

In the RFP case, the ion's radial motion becomes random in regions of magnetic stochasticity due to the radial magnetic field fluctuations sourced by the reconnection and tearing mode rotation. The ion's radial position will oscillate as it follows the oscillations of the stochastic field lines. If this motion occurs within an uncorrelated fluctuating radial electric field, the ion will experience random changes to its $E \times B$ drift velocity, and the ions can gain thermal energy as the velocity distribution broadens due to this random walk in velocity space.

Following the model in [24], the average perpendicular kinetic energy of ions experiencing random cross-field motion within an uncorrelated fluctuating electric field is estimated as

$$K(t) = \frac{1}{2} m_i v_\perp^2(t) \approx \frac{1}{2} m_i t D_v = \frac{1}{2\tau} m_i v_E^2 t, \tag{2.7}$$

where $v_\perp$ is the ion's velocity perpendicular to $\vec{B}$, $D_v \approx v_E^2/\tau$ is the perpendicular velocity diffusion coefficient, $v_E = E_r/B_0$ is the perpendicular drift velocity, and τ is the average

time step of the kinetic energy change. τ is approximated as the average time for an ion to traverse the radial correlation length of the electric field as $\tau \approx \delta_r^2/D_\perp$ where δ_r is the radial correlation length and $D_\perp$ is the spatial diffusion coefficient. The heating power density delivered to the ions is then

$$Q_{stoch} = n_i \frac{dK}{dt} = n_i \frac{m_i v_E^2}{2\tau} = n_i \frac{m_i D_\perp \tilde{E}_r^2}{2\delta_r^2 B_0^2} \tag{2.8}$$

where $\tilde{E}_r$ is the radial electric field fluctuation amplitude, and B_0 is the equilibrium magnetic field. $D_\perp$ is calculated using the stochastic magnetic diffusivity D_M as

$$D_\perp = c_s D_M = c_s \pi q R_0 \left(\frac{\tilde{B}_r}{B_0} \right)^2 , \tag{2.9}$$

where c_s is the plasma sound speed, q is the local safety factor, and $\tilde{B}_r$ is the amplitude of the radial magnetic field fluctuations. The plasma sound speed c_s is defined as

$$c_s = \sqrt{\frac{\gamma_e Z k_B T_e + \gamma_i k_B T_i}{m_i}} . \tag{2.10}$$

Note that Q_{stoch} is inversely dependent on the square of δ_r; so, only fluctuations with small radial correlation length will contribute significantly to the ion heating.

2.4.3 Viscous Damping of Bulk Flow

Due to the ions having much greater mass than electrons, any bulk plasma momentum will primarily be transported and dissipated by the ion fluid. Viscous damping is the process where fluid viscosity reduces gradients in flow velocity by converting bulk flow to progressively smaller spatial scales until the energy reaches the ion thermal motion. For the RFP, it was sensible to consider that viscous damping was a significant contributor to the anomalous ion heating given the presence of energetic reconnection events and knowing that magnetic reconnection can dissipate magnetic energy as ion flow [52]. A model of viscous dissipation in the RFP was explored in [20] where the viscous damping model was extended to include

impurity heating and their coupling to the majority ions. This model showed reasonable agreement to observed impurity heating rates, but the estimated majority ion heating was significantly weaker than in the experiment. The estimates were highly dependent on flow velocities and spatial scales which are difficult to resolve in experiment and were reliant on modeled estimates of these parameters. This work suggested that ion heating from viscous damping of flows driven by magnetic reconnection may contribute to RFP sawtooth impurity ion heating, but more experimental data and self-consistent modeling would be needed to make a conclusion about the significance of viscous damping in the RFP. In ULq plasmas, toroidal mode rotation velocities are observed at 10's of km/s; and, if these rotation speeds reflect the bulk flow of plasma, the flow shear between these modes and the surrounding plasma may be source of significant viscous dissipation.

Magnetized plasmas exhibit anisotropic viscosity where the transport of fluid momentum is highly dependent on whether the direction of the velocity gradient is parallel or perpendicular to the equilibrium magnetic field $\vec{B}_0$. Ions move freely in the direction parallel to $\vec{B}_0$, but in the directions perpendicular to $\vec{B}_0$, the ions are restricted to circular motion with a gyroradius of $\rho_i = \frac{v_{th}}{\omega_{ci}}$, where v_{th} is the ion thermal speed. This causes the parallel viscosity to be much greater than the perpendicular viscosity in strongly magnetized plasmas. For highly collisional and strongly magnetized plasmas, the parallel viscosity $\eta_\parallel$ and perpendicular viscosity $\eta_\perp$ can be approximated with the Braginskii [53] equations as

$$\eta_\parallel = \frac{n_i m_i v_{Th}^2 \tau_{ii}}{2} \tag{2.11}$$

and

$$\eta_\perp = \frac{\eta_\parallel}{1 + (\omega_{ci}\tau_{ii})^2} = \frac{3}{10} n_i m_i \tau_{ii} \frac{v_{th}}{\omega_{ci}} \tag{2.12}$$

where n_i is the ion number density, m_i is the ion mass, and τ_{ii} is the ion-ion collision time.

τ_{ii} is given by

$$\tau_{ii} = \frac{3(4\pi\epsilon_0)^2\sqrt{m_i}\,T_i^{3/2}}{4\sqrt{\pi}\,n_i Z^4 e^4\,ln(\Lambda)}\,. \tag{2.13}$$

For the parameters of plasmas in MST, $\eta_\perp$ is usually several orders of magnitude lower than $\eta_\parallel$.

The power dissipated per unit volume due to viscous dissipation is

$$Q_{visc} = \eta_\perp \left(\frac{\partial v_\perp}{\partial r}\right)^2 + \eta_\parallel \left(\frac{\partial v_\parallel}{\partial l_\parallel}\right)^2 + \eta_\perp \left(\frac{\partial v_\parallel}{\partial r}\right)^2, \tag{2.14}$$

where $v_\perp$ is the velocity perpendicular to both the magnetic field and radial direction, $v_\parallel$ is the velocity parallel to the magnetic field, $\partial/\partial r$ is the radial derivative, and $\partial/\partial l_\parallel$ is the derivative along a field line. In ULq plasmas the toroidal mode rotation velocities measured by the toroidal array coils and the minimal poloidal rotation velocities measured by Doppler spectroscopy suggest that the bulk flows would be mostly toroidal and the gradient in this flow would be radial. In this case, the dissipation due to $\eta_\parallel$ can be neglected and the viscous heating power density from radial shear in toroidal flow is

$$Q_{visc} \approx \eta_\perp \left(\frac{\partial v_\phi}{\partial r}\right)^2 \approx \frac{3}{10} n_i m_i \tau_{ii} \frac{v_{th}}{\omega_{ci}} \left(\frac{\Delta v_\phi}{\Delta r}\right)^2\,. \tag{2.15}$$

where Δv_ϕ is difference in flow velocity across an assumed linear flow shear layer, and Δr is the width of the layer.

2.5 Summary

Anomalous ion heating is a poorly understood phenomenon commonly observed in astrophysical and laboratory plasmas. In Ohmic-heated plasmas, ion temperatures greater than or equal to electron temperatures are characterized as anomalous since they cannot be explained by collisional coupling with the electrons. Strong ion heating is observed in RFP plasmas and is associated with global sawtooth reconnection events, a significant loss in

magnetic energy, and strong magnetic fluctuations. There is often preferential heating of the impurity species over the majority ions. The heating efficiency of the majority ions is proportional to the square root of the mass of the majority species, and the increase in majority ion temperature is inversely proportional to plasma density. The ion heating from the RFP sawtooth is mostly in the perpendicular degree of freedom.

Anomalous ion heating has also been observed in past ULq plasma experiments. ULq plasmas are challenging to sustain in experiments due to their high global plasma resistance. These plasmas had flat $q(r)$ profiles, hollow current density profiles, and often had $q(r)$ minimums between the mid-radius and edge. ULq plasmas exhibited a tendency to relax towards specific values of q_a such that loop voltages significantly larger than that required to sustain the plasma were needed in order to increase the plasma current. Insufficient loop voltage resulted in the fast growth of resonant modes and minor collapse of the plasma current but not major disruption. Magnetic fluctuation spectra were often dominated by a single helicity, and the toroidal mode rotation speeds were greater than that observed in the RFP. Simulations of ULq plasmas suggest that large magnetic island structures are formed with the topology highly dependent on q_a. $T_e(r)$ profiles are core-peaked at high q_a and flatten gradually as q_a is decreased. $T_z \leq$600 eV and $T_i \leq$150 eV were observed when $T_e \leq$ 100 eV, and both T_z and T_i had an inverse dependence on plasma density. Stochastic heating was suggested as a mechanism to explain the observed ion temperatures, but no conclusive evidence was presented.

The mechanisms which could be responsible for the ion heating in ULq plasmas are ICR damping, stochastic heating, and viscous damping. ICR damping can occur when the energy in large amplitude, long wavelength magnetic fluctuations cascades to smaller wavelengths and higher frequencies. If these high frequency fluctuations have a left-hand polarized electric field component, they can couple their energy to the ion gyromotion and directly heat the

ions. Stochastic heating can occur when electric field fluctuations are strong enough to cause chaotic ion motion. Viscous dissipation can occur if there are significant bulk flows which develop flow shear layers within the plasma.

Chapter 3

The Madison Symmetric Torus and Diagnostics

3.1 The Madison Symmetric Torus

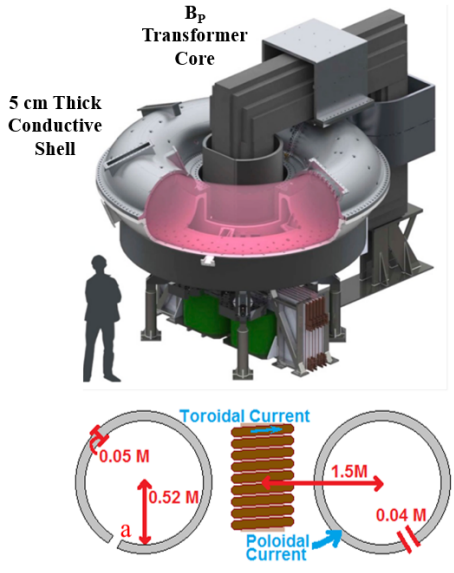

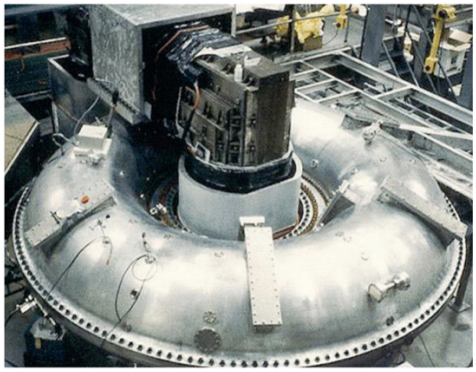

B_T (Applied)	I_P	B_P Flux Swing	Plasma Volume	Pulse Length	Loop Voltage
< 0.13 T	< 600 kA	2 Wb	8 m^3	<60 ms	<120 V

Figure 3.1: CAD model, image, and some important parameters of MST.

These experiments have been performed in the Madison Symmetric Torus (MST), a mid-size toroidal plasma confinement device operated at the Wisconsin Plasma Physics Labora-

tory at the University of Wisconsin-Madison. An image and CAD model of MST is shown in figure 3.1 along with some relevant machine parameters. The plasma boundary in MST is limited by graphite tiles covering approximately 15% of the wall which support a 2 cm gap between the plasma edge and the shell.

A feature of MST which is essential for ULq plasma operation is the thick, conductive, close-fitting shell. As magnetic flux begins to penetrate the conducting shell, eddy currents are generated in the shell which oppose this penetration, and these eddy currents decay over time due to the resistivity of the shell. The aluminum shell is 5 cm thick, giving a resistive wall time τ_w of approximately 800 ms [54]. τ_w describes the time scale of magnetic field diffusion through a conductive wall and is defined as

$$\tau_w = \frac{\mu_0 \delta_w r_w}{\eta_w} \ , \tag{3.1}$$

where δ_r is the wall thickness, r_w is the wall radius, and η_w is the wall resistivity. If the duration of the discharge is significantly less than τ_w, the plasma effectively sees an ideal conductor boundary which does not allow for any penetration of magnetic flux. This enables operation far beyond conventional external-kink stability limits since, apart from error fields, the magnetic perturbations of large-scale plasma instabilities are forced to have a vanishing normal component at the wall. The conductive shell is critical to ULq operation since tokamaks are increasingly susceptible to kink instability and disruption as $q_a \leq 2$ is approached. The shell has insulating gaps in both the toroidal and poloidal planes. The toroidal gap allows for a poloidal current to be driven in the shell which produces the B_T, and the poloidal gap prevents toroidal wall currents from being driven by the central transformer pulse during operation. The voltage across the poloidal gap is measured during operation and used as a proxy for the loop voltage applied to the plasma. The location of diagnostics will be described by their poloidal and toroidal angle. 0° toroidal refers to the location of the transformer core and poloidal gap, and 0° poloidal refers to outboard midplane.

The currents driving B_P and B_T are both sourced by feedback-controlled programmable power supplies composed of many reconfigurable power supply modules [14]. These power supplies allow for arbitrary waveforms to be delivered to these circuits with unprecedented power and fidelity. Currents are corrected at a rate of 10 kHz, and the system can deliver up to 120 loop volts to the plasma. This performance is also critical to ULq operation as the plasmas have high global resistance and can exhibit disruption-like instabilities during plasma current ramp-up if the loop voltage is insufficient.

3.2 External Magnetic Coil Arrays

MST employs several sets of wall-mounted magnetic pickup coils to characterize the plasma equilibrium and MHD activity. The locations of these pickup coils are shown in figure 3.2.

A Rogowski coil is mounted in the interior vessel wall and encircles the plasma column to measure the B_P from the plasma current. This provides a direct measurement of the toroidal plasma current and is used to estimate the average B_P at the plasma edge. A flux

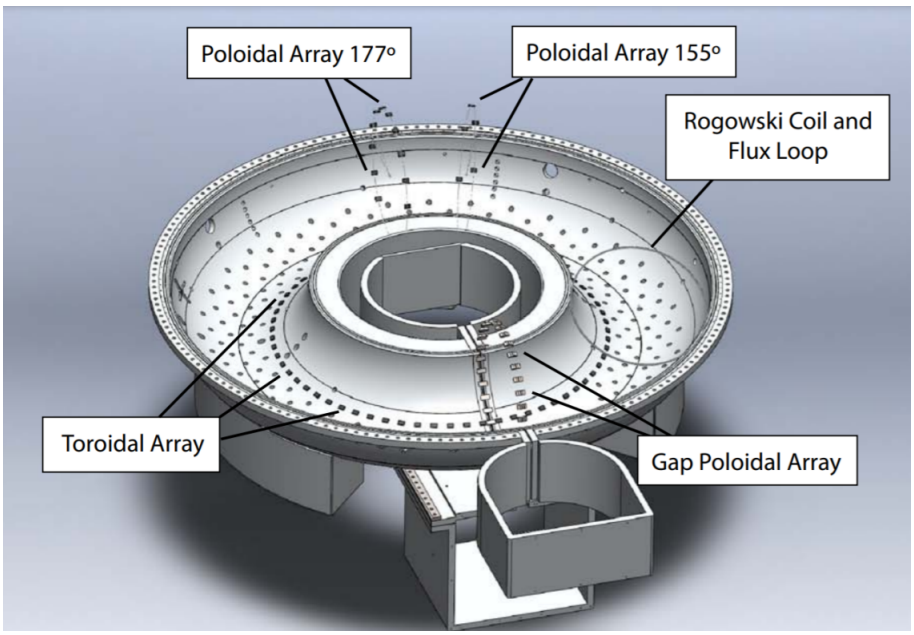

Figure 3.2: Pickup coil arrays on MST. Figure reproduced from [55]

loop which samples B_T is mounted at the same location and encircles the plasma column. This coil provides a measurement of the average B_T at the wall B_{Tw}. q_a is estimated as

$$q_a \approx \frac{2\pi a^2 B_{Tw}}{R\mu_0 I_P} \ , \tag{3.2}$$

where $a = 0.52$ m is the shell minor radius and $R = 1.5$ m is the major radius.

The toroidal array is a toroidally symmetric ring of coil triplets measuring the B_T, B_P, and B_r magnetic field components at each triplet location with their signals analog-integrated and digitized at 200 kHz, and B_r is the magnetic field component in the direction outward from the geometric center of the poloidal cross section. Each triplet is evenly spaced around the torus and is located just outside the plasma edge at 61° below the inboard midplane. Signals from this coil set are calibrated before each discharge and Fourier-decomposed to determine amplitudes and phases of the toroidal modes throughout a shot. The B_P and B_T measured at each toroidal angle is decomposed into the sum of components as

$$B_P(\phi, t) = \sum_{n=1}^{N} b_n(t) \cos\left(n\phi - \delta_n(t)\right) \tag{3.3}$$

where ϕ is the toroidal angle, n is the toroidal mode number, b_n is the amplitude of the n^{th} component, δ_n is the component's phase, and $N = 15$ for B_P and $N = 31$ for B_T. Toroidal mode amplitudes and phases are well resolved by this coil set, but it provides no information on the poloidal mode structure since there is no poloidal separation among coils.

The poloidal gap in the conducting wall is necessary to avoid a conductive loop encircling the transformer, but this gap can allow for significant magnetic field errors in the region. To mitigate this error, there is a poloidal array of 32 B_r pickup coils and 38 field correction coils mounted along the gap. Measurements from the pickup coils are used by a feedback control system to drive the correction coil currents necessary to cancel out the error fields and preserve field symmetry in the vessel. There is also an array of 16 B_P coils at the gap which are similarly Fourier-decomposed to provide information on the poloidal mode amplitudes

and phases up to $m = 7$. These coil signals are also analog-integrated and digitized at 200 kHz.

The dense array is a small cluster of 1 cm spaced B_P and B_T pickup coils mounted at 246° toroidal and 32° below the outboard midplane. This coil set has better sensitivity to high frequency fluctuations and is digitized at 3 MHz as $\dot{B}$ directly rather than being integrated with analog circuits. All of the coils discussed so far are fixed to the interior wall of the vessel and record data for every discharge.

3.3 Insertable Probes

For magnetic field measurements within the plasma, an insertable probe containing an array of coils is used. The probe array is composed of 20 coil triplets spaced evenly over 20 cm and cemented within a boron-nitride cylindrical particle shield [56]. It was mounted at 15° above the outboard midplane at 180° toroidal, the side of MST opposite the poloidal gap. This probe allows for measurements of radial profiles of B_T, B_P, and B_r as well as their fluctuations, analog-integrated and digitized at 200 kHz. It can be inserted up to 35 cm within the plasma and provides a direct measurement of the local $q(r)$ and the radial distribution of magnetic fluctuations.

For plasma potential and electric field fluctuations, a capacitive sensor probe array is used [57] [58]. The probe consists of boron-nitride stalk which holds 4 steel rings with radial spacing of 7 mm. The stalk and steel rings are covered by a 2 mm thick annular sheath of boron-nitride which serves as the particle shield and the dielectric which couples the rings to the plasma potential. Due to the high secondary electron emission rate of boron-nitride in plasmas with $T_e > 18$ eV, Debye sheath formation is prevented, and the potential at the probe surface is the plasma potential rather than floating potential. The voltage on the capacitive sensor rings is digitized through a capacitive divider. Each sensor is calibrated

by placing a close-fitting aluminum sheath around the probe and applying an AC voltage to the sheath. Calibration values are obtained by dividing the RMS voltages of the applied voltage and the output of the capacitive sensor. Signals are digitized at 1 MHz, and the probe and capacitive divider have nearly flat frequency response up to 150 kHz.

3.4 Far Infrared Interferometer

Electron density measurements are provided by the far-infrared laser interferometer system (FIR) [59] [60] [61]. The FIR interferometer has 11 chords which measure line integrated electron density $\bar{n}_e$ for each tangential chord, shown in figure 3.3. The FIR interferometer can resolve $\bar{n}_e$ as low as $1 \times 10^{17}\ m^{-3}$ and has a bandwidth of approximately 100 kHz for plasma conditions in this work. The basis of an FIR interferometer is that a coherent beam of light will experience a measurable phase shift if the index of refraction of its medium varies. The relationship between the phase shift $\Delta\theta$ and electron density is derived from the Appleton-Hartree formula for the cold plasma refractive index as [62] [63]

$$\Delta\theta = \frac{\lambda e^2}{4\pi c^2 m_e \epsilon_o} \int n_e dl \ , \tag{3.4}$$

where λ is the vacuum wavelength, e is the elementary charge, c is the speed of light, m_e is the electron mass, and the integral is over the path length l. Thus, the phase shift of a coherent beam over the beam path through the plasma is proportional to $\bar{n}_e$. The MST FIR system is a type of heterodyne interferometer. An FIR laser shines a beam (1 of 11) with one frequency through the plasma volume where it experiences a phase shift. This probing beam is then combined with a reference beam tuned to a slightly different frequency before reaching the diode detectors. This beam combination results in interference at the detector which produces a modulated signal with a frequency $f_{mod} = f_{probe} - f_{ref}$. The phase difference between the probe and reference beams is equal to the the phase shift of the

Chord Name	Impact Parameter $R - R_0$ (cm)	Toroidal Angle ϕ (degrees)	chord length L (cm)
N32	-32	255	81.97
N24	-24	250	92.26
N17	-17	255	98.29
N09	-9	250	102.4
N02	-2	255	103.9
P06	6	250	103.3
P13	13	255	100.7
P21	21	250	95.14
P28	28	255	87.64
P36	36	250	75.04
P43	43	255	58.48

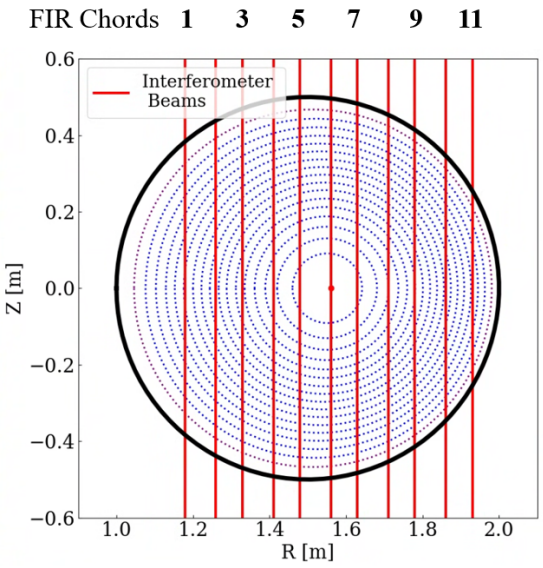

Figure 3.3: (Left) Table of far-infrared (FIR) interferometer geometry parameters. R_0 refers to the geometric axis. (Right) Poloidal cross section showing FIR beams.

modulated signal which, when compared to the phase in vacuum, can be used to calculate $\bar{n}_e$ directly. The measurements from the FIR interferometer are used to measure the radial $\bar{n}_e$ profile of the plasma as well as characterize how the $\bar{n}_e$ fluctuations relate to magnetic fluctuations.

3.5 Ion Doppler Spectrometer

Impurity ion temperatures are measured with the ion Doppler spectrometer (IDS) [64] [65]. This high throughput, high resolution spectrometer can simultaneously observe light from two collection fibers with 11 available tangential views across the diameter of the device. IDS has a spectral resolution of approximately 0.5 Angstrom, an etendue of 0.8 mm^2 sr, and an aperture of $f/4.5$. A diagram of the system as well as some relevant specifications are shown in Figure 3.4. The basis of Doppler spectroscopy is that radiating ions will emit photons with their wavelengths Doppler shifted depending on the ion's velocity relative to the observer, and their collective effect is seen in features of the observed emission line. For thermalized impurities in a plasma, their emission lines will have a Doppler broadened spectral width

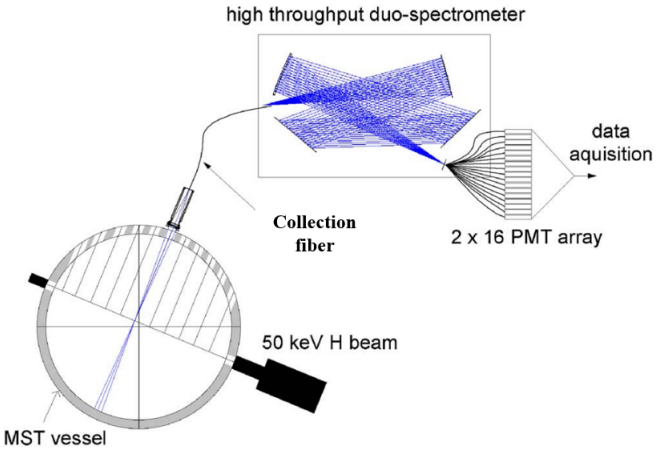

Ion Doppler Spectrometer Specifications

Resolution: 0.5 Å
Spectral Window: 6.4 Å
Range: 225 to 450nm
Etendue: 0.8 mm^2 sr
Aperture : $f/4.5$
Acquisition Speed: 250 kHz

Figure 3.4: Diagram of ion Doppler spectrometer system and relevant parameters. Figure adapted from [66].

dependent on the impurity temperature T_z with the centroid of the line Doppler shifted in wavelength depending on impurity species fluid velocity towards or away from the collection optics. The shape of an emission line, emitted from a thermal distribution and without fine structure effects, is defined by a Gaussian function of the form [63]

$$f(\lambda) = A\frac{-(\lambda - \lambda_c)^2}{2\sigma^2} \,, \tag{3.5}$$

where A is the amplitude at the peak of the distribution, λ_c is the central wavelength of the line, and σ is the standard deviation of the distribution. σ is related to the ion temperature by

$$\sigma = \frac{\lambda_c}{c}\sqrt{\frac{kT_z}{m_z}} \,, \tag{3.6}$$

where c is the speed of light and m_z is the ion mass. The wavelength of the centroid of the line λ_c is calculated with

$$\lambda_c = \lambda_0(1 + \frac{v_{LOS}}{c}) \,, \tag{3.7}$$

where λ_0 is the central wavelength of the line for a stationary ion and v_{LOS} is the bulk ion velocity parallel to the line-of-sight. An example of modeled Gaussian emission lines emitted

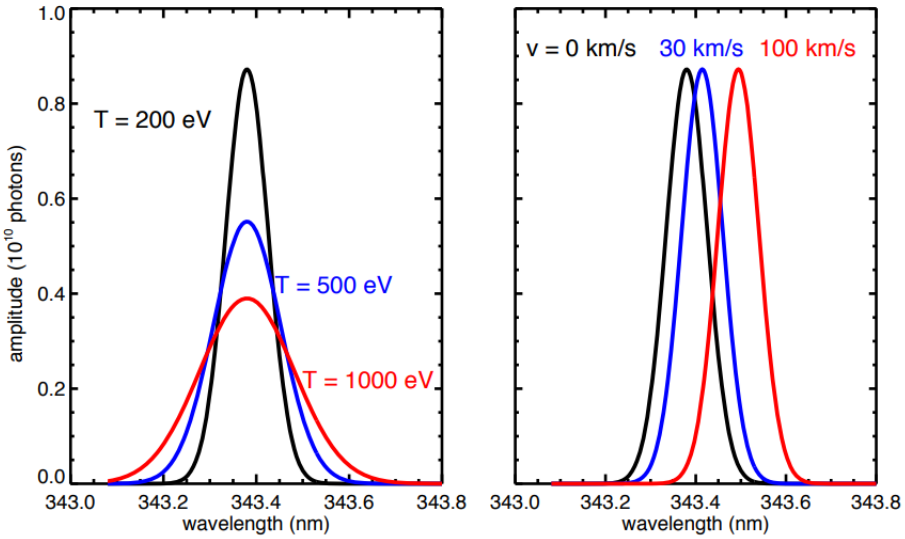

Figure 3.5: (Left) Modeled Gaussian emission lines from thermalized particles with different temperatures. (Right) Gaussian emission lines from particles with different flow velocities. Figure reproduced from [33].

by ions with thermal velocity distributions of different temperatures and flow velocities is shown in figure 3.5.

The IDS was designed as an impurity charge exchange recombination spectroscopy (ChERS) system to be used in conjunction with a diagnostic neutral beam [67] [68]. In a ChERS system, a high energy neutral beam traverses the plasma, and the neutrals donate electrons to fully ionized species via charge exchange reactions to stimulate photon emissions localized to the beam path [69]. For example, C^{+6} ions will charge exchange with beam neutrals to become C^{+5} with an electron in an excited state, and this electron will decay towards the ground state by emitting photons of characteristic wavelengths. There will also be C^{+5} ions emitting photons naturally from electron impact excitation due to collisions with plasma electrons; so, the photon flux from this background emission must be subtracted from the total photon flux in order to extract the charge exchange emissions from the total signal. This requires that the brightness of the charge exchange emissions be great enough relative to the background such that the signal-to-noise ratio allows for practicable extraction of

the signal. This is made tractable by the fact that fully ionized species have high charge exchange cross sections at particular neutral beam energies and that highly ionized charge state emissions tend to have low background brightness levels.

Performing ChERS measurements on partially ionized impurities is very difficult because their bound electrons will partially shield the electric potential of their nucleus and significantly reduce their charge exchange cross section. A low charge exchange cross section along with low charge state ions having relatively bright background emissions results in a signal-to-noise ratio too low for the IDS system to distinguish the charge exchange signal from the background. Due to limited electron temperatures, the fully ionized species necessary for ChERS were not observed in ULq plasmas. The terminal charge state for boron and carbon impurities in ULq plasmas is typically (3+) and in some cases (4+). ChERS measurements were attempted using emissions from these partially ionized impurities as well as fully ionized helium, but the signal-to-noise ratio was too low to extract the charge exchange signal. Thus, this work was performed using IDS as a passive impurity emission diagnostic measuring line-averaged impurity temperatures $\bar{T}_z$.

A significant portion of this work involved determining the optimal emission line to use for measuring $\bar{T}_z$ across a wide range of parameters in ULq plasmas. An attempt was made to use helium emissions. The plasmas were doped with trace amounts of helium; however, this resulted in very bright helium emissions in the edge region with very narrow line widths. These bright emissions from cold helium in the edge obscured measurement of T_z in the core. C^{4+} emissions were only observed in plasmas with $q_a < 0.3$. C^{3+} emissions were observed, but an emission line which lacked fine structure broadening could not be found. The boron B^{3+} charge state, referred to in spectroscopic notation as B-IV, provides the most consistent $\bar{T}_z$ measurements across the full q_a range of ULq and at most radial locations by observing the isolated fine structure component at 282.2 nm. Boron impurities are present in MST

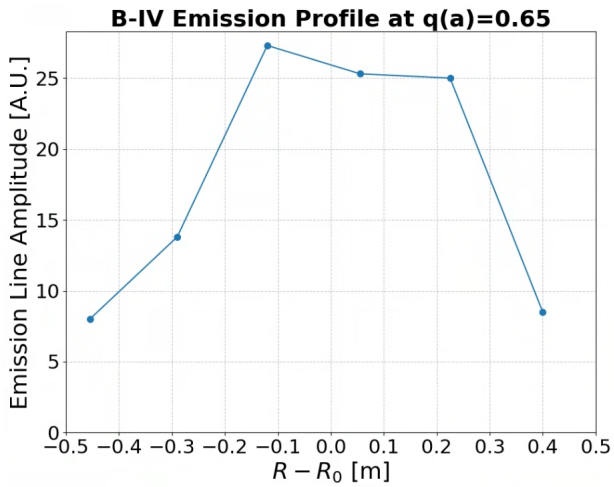

Figure 3.6: Radial profile of the B-IV emission line (282.2 nm) amplitude from q_a =0.65 discharge. R_0 refers to the geometric axis.

because of a history of boronization for vacuum conditions as well as regular use of diagnostic probes shielded with boron-nitride. The radial profile of impurity emissions in ULq plasmas differs significantly from the RFP and tokamak. For RFP and tokamak plasmas with good confinement, impurity charge states tend to form annular emission shells with a dominant charge state in each shell. These shells will start with neutral and singly ionized species in the edge and step towards fully ionized species in the core. Due to the flattened T_e profiles and high impurity transport in ULq plasmas, B-IV emissions tend to be strong across most of the plasma radius. A radial profile of the B-IV emission line amplitude is shown in Figure 3.6

To facilitate fast measurements, IDS uses a 2x16 array of photomultiplier tubes (PMT) and transimpedance amplifiers as the detector array for each of the two input fibers. A 2x16 array of optical fibers is placed at the exit slit of the spectrometer, and these fibers channel light to the photo-cathode of each channel's PMT. A photon strikes the high-voltage biased photo-cathode to eject an electron, and this electron is accelerated to a dynode which ejects several more electrons on impact. This process is repeated through 11 dynode stages, resulting in exponential electron amplification and a measurable current at the anode from a

single photon interaction at the photo-cathode. This electron multiplication is a stochastic process such that the number of electrons ejected at each dynode stage is described by a Poisson probability distribution of the form [65]

$$P_\mu(n) = \frac{\mu^n e^{-\mu}}{n!} \,, \tag{3.8}$$

where μ is the expectation value and n is the number of secondary electrons ejected by a primary electron.

When detecting low levels of light, the uncertainty in the measurement of the incident photon flux is usually dominated by photon counting statistics which is also governed by a Poisson distribution. If an ideal steady light source is repeatedly sampled by a detector observing an average of N photons per sample, the variance of the samples is equal to the mean value N, and the standard deviation of the samples is equal to the square root of N. Thus, the relative uncertainty in the number of photons n counted in one sample is $\frac{\sqrt{n}}{n} = \frac{1}{\sqrt{n}}$. In this system, uncertainty is quantified by estimating an effective photon count rate as

$$\Phi_{eff} = \frac{\mu_V}{\sigma_V T_{int}} \,, \tag{3.9}$$

where μ_V is the mean voltage output of the transimpedance amplifier, σ_V is the standard deviation of the voltage samples, and T_{int} is the integration time per sample. A DC deuterium arc lamp was used to provide a steady broadband light source within the molecular deuterium continuum band of the spectrum at 282 nm. Measurements of the signal mean and standard deviation over many samples for each channel was then used to calculate the effective photon count rate as a function of voltage through the linear operation range of the PMT. The estimate of the number of photons per sample is used to weight each data point in the Gaussian fit so that the uncertainty in $\bar{T}_z$ reflects both the quality of the fit and the uncertainty in the photon count for each channel. In this work, an integration time

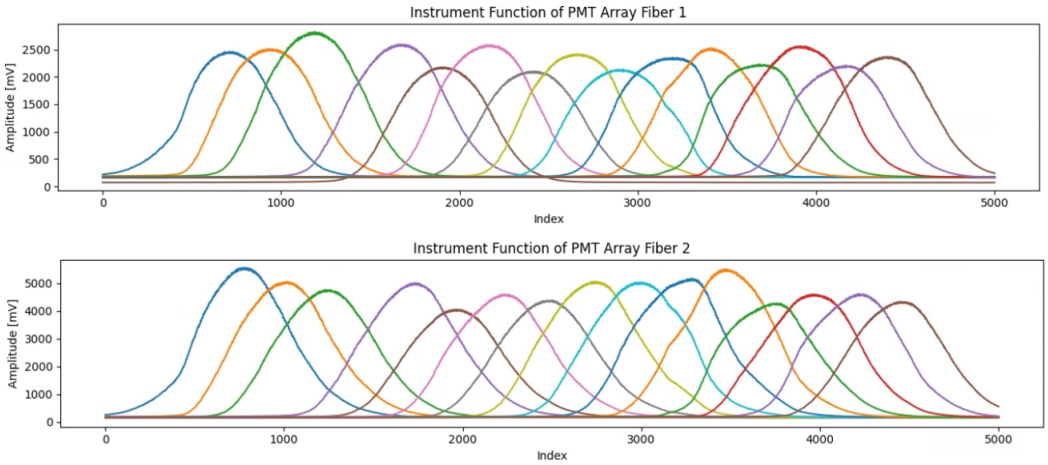

Figure 3.7: Instrument profiles for fiber-1 and fiber-2 detector arrays of the ion Doppler spectrometer.

of 100-200 μs per sample was found to give the best quality fits while still resolving the fluctuations in $\bar{T}_z$.

IDS is spectrally calibrated using a cadmium lamp. The Cd-I doublet at 346.62 and 346.77 nm is swept across the PMTs, and the known spacing between the doublet components provides a relationship between channel and wavelength. For this system, the change in central wavelength with grating angle is very close to linear for central wavelengths of 240-360 nm; so, this calibration is valid over this range of central wavelengths. Any spectrometer system will introduce some degree of instrumental broadening to a narrow emission line which must be accounted for in order to accurately measure T_z from Doppler broadening. Instrumental broadening and channel overlap is measured for this work using a DC mercury pen lamp as the steady source of a narrow or "cold" emission line at 253.7 nm. By slowly rotating the diffraction grating, the line was swept across the PMTs to trace out the instrument function of the system. The data from this instrument function trace is shown in Figure 3.7.

To perform a fit, a Gaussian emission line with some initial guess parameters (A, λ_c, and σ) is generated and convolved with the instrument function of the spectrometer. An

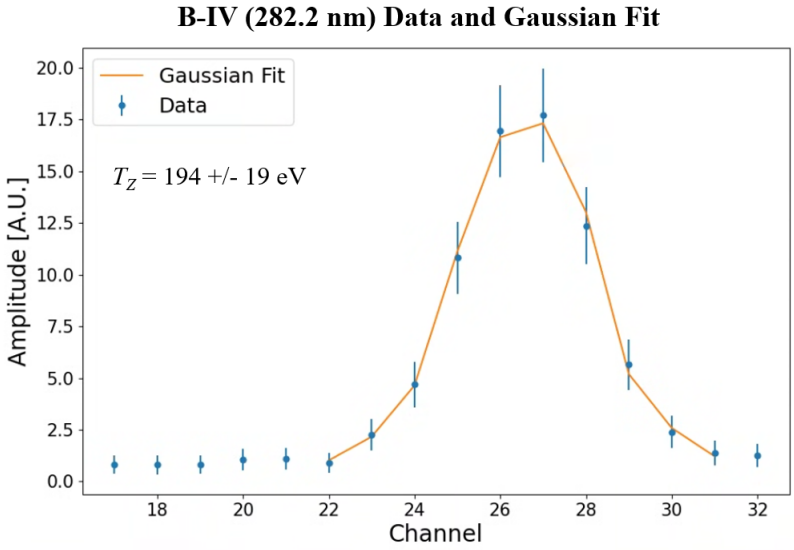

Figure 3.8: IDS data and $\bar{T}_z$ fit for the B-IV emission line. Data from all channels is plotted in blue with error bars representing photon count uncertainty. The best fit Gaussian spectrum is convolved with the instrument function and plotted as a yellow line.

iterative least squares fit is then performed between the modeled spectrum and the measured spectrum, and $\bar{T}_z$ is determined by the value of σ which gives the best fit to the data. An example of a fit is shown in Figure 3.8. Notice that the spectrum is symmetric and well-fit by a simple Gaussian. Note that the plotted fit is not a perfect Gaussian since it has been convolved with the instrument function in order to compare to the measured data. This method includes the effects of instrumental broadening, channel overlap, and channel-to-channel variations in the calculation of $\bar{T}_z$.

3.6 Summary of Diagnostics

The objective of this work is to characterize and understand the mechanism of the anomalous impurity heating observed in ULq plasmas. It is shown in the following chapters that impurity temperatures are associated with the amplitude and rotation of helical modes which result in strong fluctuations measured in several diagnostics with varying degrees of coherence. The primary diagnostic is the a high throughput, high resolution spectrometer for

making line-integrated measurements of B-IV impurity $\bar{T}_z$. This system provides $\bar{T}_z(t)$ measurements at $\leq$20 kHz as well as radial profiles of $\bar{T}_z(r)$. Equilibrium $\bar{n}_e(r)$ is measured by an 11-chord far-infrared interferometer, and fluctuations in $\bar{n}_e$ are measured at $\leq$100 kHz. Global mode amplitudes and rotation speeds are characterized by wall-mounted toroidal and poloidal arrays of pickup coils with signals analog-integrated with a bandwidth of 250 kHz. Higher frequency magnetic fluctuations are measured by a cluster of wall-mounted $\dot{B}$ coils digitized at 3 MHz. Internal fluctuations of B_P, B_T, and B_r are measured with an insertable probe array of pickup coils with signals analog-integrated with a bandwidth of 250 kHz. The magnetic probe is inserted to 35 cm within the plasma edge, and the data is used to infer the radial location of the modes and spatial scale of their perturbations. Since non-collisional ion heating must be facilitated by a fluctuating electric field, plasma potential and radial electric field measurements are made using a capacitive probe inserted to 6-8 cm within the plasma edge. The probe contains four capacitive sensors each separated radially by 7 mm, and signals are digitized at 1 MHz with a flat frequency response up to 150 kHz.

Chapter 4

ULq Pinch Operation and Observations

A major portion of this work involved determining how to operate plasmas in the poorly understood ULq regime and observing how general characteristics of ULq plasmas differ from the reversed-field pinch (RFP) and tokamak. These observations are summarized in this chapter.

4.1 Startup and Current Ramp

A standard tokamak plasma is initiated by first driving the B_T to a steady value followed by puffing deuterium into the vessel and ramping current in the B_P transformer winding. The electric field induced by the transformer flux swing ionizes the neutral gas and ramps up the plasma current I_P. There is no limit to how slow I_P can be ramped in the standard tokamak; however, since the tokamak has good confinement, there is a settling time required for the pressure and current profiles to relax to their lowest energy state. This settling time is usually several milliseconds in MST tokamak plasmas, and ramping I_P too quickly can result in strong mode activity and significant perturbations in I_P and n_e during this settling period. Gas fueling can begin at the same time as loop voltage is applied without consequence as long as there is sufficient neutral density to prevent electron runaway triggering a low-density

major disruption, which can be observed in MST.

RFPs are initiated in a similar fashion to the tokamak, but at roughly $\frac{1}{2}$ of the way through the I_P ramp, the applied B_T is quickly reduced to 0 or a small value with opposite polarity. The plasma current then reorganizes to an RFP configuration with significant poloidal plasma current that sustains the $B_T(r)$ profile. Continued ramping of I_P also increases the poloidal plasma current and the self-driven B_T until steady I_P is reached. RFPs tend to be generated more consistently and more efficiently when the I_P ramp rate is maximized, and startup can be sensitive to the neutral fueling rate and timing. Fueling usually begins at the same time as loop voltage is applied, and the fueling rate required is significantly higher than a tokamak of comparable plasma density.

ULq plasma startup is similar to the standard tokamak but is challenging due to the high global plasma resistance $R_P = \frac{V_{loop}}{I_P}$ and an apparent reduction of neutral particle transport into the plasma. The high R_P requires a large loop voltage in order to continue ramping I_P into the ULq regime, usually 60-120 V in MST. ULq plasmas exhibit a tendency to relax towards major rational values of q_a, and this effect is especially pronounced at $q_a \approx 1$. If the loop voltage is insufficient, attempting to ramp I_P to $q_a < 1$ results in large oscillations in I_P which prevent transition to the ULq regime. This effect is best suppressed by maximizing the applied loop voltage and I_P ramp rate.

ULq I_P ramp-up can take several milliseconds which means an electric field of order 10 V/m is sustained for this ramp duration. This electric field is strong enough to generate suprathermal electrons and cause sudden disruption-like drops in I_P if the neutral density is too low, and these events are coincident with bursts of soft x-rays. This disruption-like behavior can be suppressed by maximizing plasma density during I_P ramp-up. It is observed that $\bar{n}_e$ decreases significantly during the I_P ramp to the ULq regime. $\bar{n}_e$ has a weak response to gas puffing such that a fueling rate which can support an RFP with $\bar{n}_e \approx 1 \times 10^{19}\ m^{-3}$ is

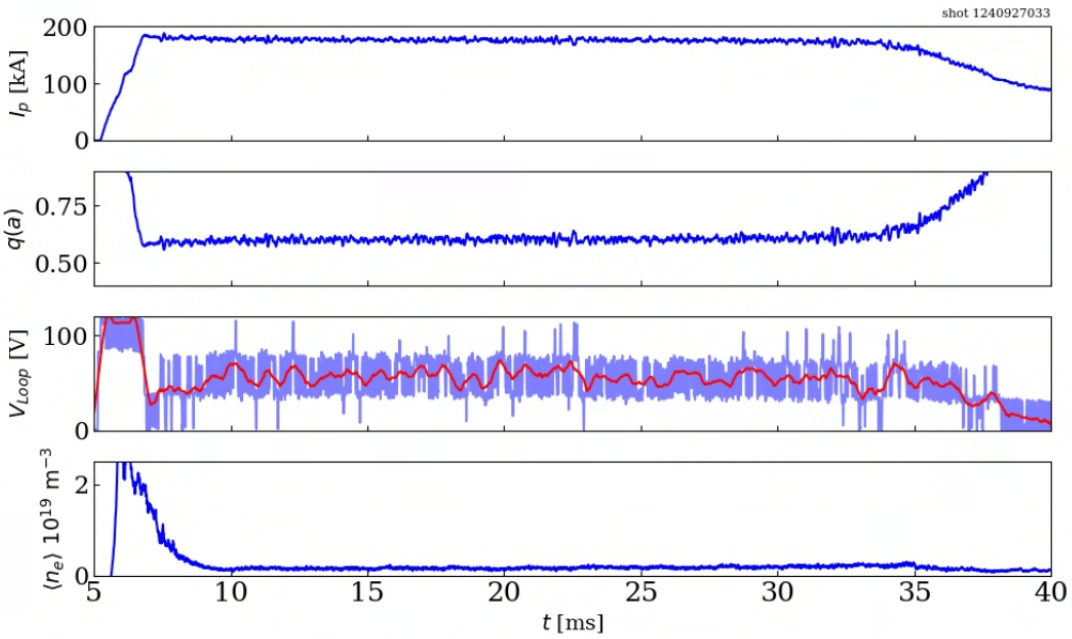

Figure 4.1: Example of an ULq discharge with q_a =0.6

insufficient to reproducibly startup and sustain an ULq plasma at $\bar{n}_e \approx 1 \times 10^{18}\ m^{-3}$. It was found that puffing a substantial amount of gas 5 ms before applying loop voltage greatly increases the initial $\bar{n}_e$ which reduces or eliminates fast electron losses and disruption-like behavior. An example of an ULq plasma discharge is shown in Figure 4.1. Notice the order of magnitude drop in $\bar{n}_e$ during startup and high loop voltage. As long as the applied loop voltage and neutral fueling are sufficient, ULq plasmas are reproducible and do not disrupt.

4.2 Neutral Particle Transport and Energy Confinement

At steady-state, the tokamak exhibits good energy and particle confinement. R_P is a proxy measure of the global energy confinement with $R_P \leq 0.07$ mOhm for tokamaks in MST. MST tokamak plasma density can be easily controlled and held flat by tuning puff valve duration and timing throughout the discharge. Tokamak plasmas exhibit a pumping effect where neutral pressure outside the plasma decreases after startup due to the plasma acting as a neutral particle sink through ionization and confinement.

Steady state RFP behavior is similar to the tokamak but with higher R_P of approximately 0.05 mOhm for a 400 kA RFP plasma. This decrease in R_P relative to the tokamak is due to the large performance gap over the 50 kA standard tokamak; a standard tokamak plasma with comparable magnetic field strength would have a longer energy confinement time and lower R_P. Plasma density can be easily controlled by tuning puff valve settings, but much higher neutral fueling rates are required compared to the tokamak. The neutral particle pumping effect is reduced in RFP plasmas compared to the tokamak.

ULq plasmas tend to bifurcate into one of two different behaviors depending on $\bar{n}_e$, and this bifurcation typically occurs near $\bar{n}_e \approx 5 \times 10^{18}\ m^{-3}$. In the high-density regime, $\bar{n}_e$ is highly responsive to gas puffing, and density control is simple like the standard tokamak. In the low-density regime, $\bar{n}_e$ is minimally responsive to gas puffing. If a $\bar{n}_e \approx 2 \times 10^{18}\ m^{-3}$ ULq plasma is repeated but with gas throughput increased by a factor of 5×, the repeated discharges appear nearly identical to the initial low-density discharge. It was found that repeating several high-density discharges prior to low-density discharges resulted in more easily controllable $\bar{n}_e$ in the low-density regime. This is presumed to be due to accumulation of deuterium within the wall or limiter surfaces. The apparent fueling from the limiter surfaces gradually decreases over several discharges; after density control is lost, high-density plasmas can be repeated to regain control of low-density discharges. It is not clear what causes this change in particle transport in the low-density regime, or why additional gas puffing is not as effective as loading the vessel with gas over several discharges.

The R_P dependence on $\bar{n}_e$ is also very different in the high and low density regimes. In the high-density regime, R_P increases with increasing $\bar{n}_e$ as is seen in the RFP and tokamak. However, in the low-density regime, R_P surprisingly increases with *decreasing* $\bar{n}_e$. This effect can be seen in the plot of Ohmic input power as a function of $\bar{n}_e$ for fixed q_a, shown in Figure 4.2. Factors that may contribute to this effect include increasing impurity concentration and

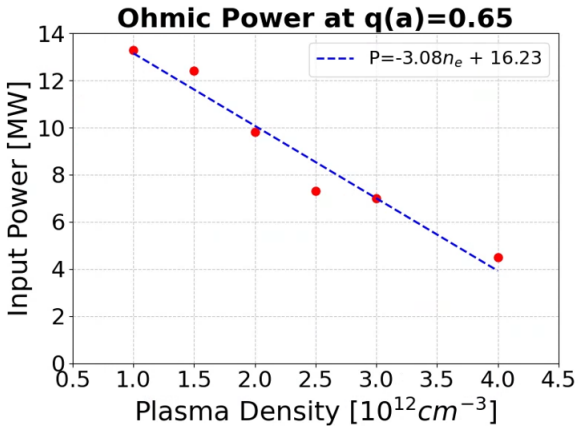

Figure 4.2: Ohmic input power versus average plasma density in the low-density regime at fixed q_a. In the low-density ULq regime, R_P increases roughly linearly with decreasing $\bar{n}_e$.

radiated power, increasing anomalous heating power, and degradation of confinement. All of this work has focused on the low-density regime of ULq plasmas where high impurity ion temperatures are observed and vary significantly with discharge parameters.

Steady state behavior of ULq plasmas strongly depends on the value of q_a. There is a tendency for dominant modes to lock to the wall at $q_a \approx 1$ and $q_a \approx 0.5$, and these values have been avoided in this work due to inconsistent discharge behavior. ULq plasmas have relatively high R_P typically ranging from $R_P \approx 0.1$ to 0.4 mOhm depending on q_a and $\bar{n}_e$. A plot of Ohmic input power and R_P as function of q_a is shown in figure 4.3 which displays a non-linear relationship to q_a and significant decrease in R_P at $q_a \approx 0.55$. Plasmas in the range of $0.6 \leq q_a \leq 0.95$ exhibit similar discharge behavior. At low-density, $\bar{n}_e$ is minimally responsive to gas puffing, and controlling $\bar{n}_e$ in this q_a range is relatively difficult. In the region near $q_a \approx 0.55$ there is a decrease in R_P, significant decrease in magnetic fluctuation amplitudes, and $\bar{n}_e$ is easier to control than the higher-q_a range. For ULq plasmas with $q_a \leq 0.5$, R_P increases significantly as q_a is lowered towards zero, and $\bar{n}_e$ is highly responsive to gas puffing.

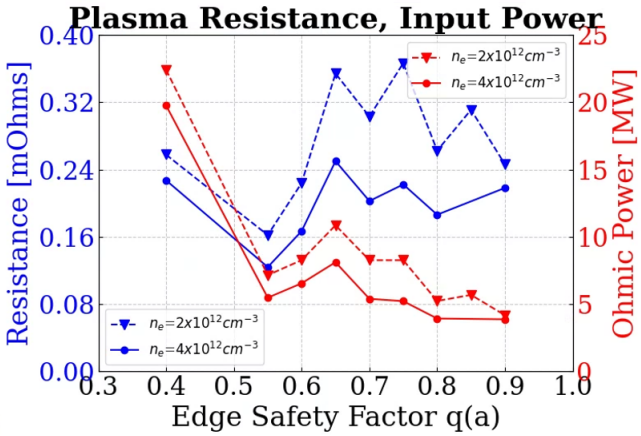

Figure 4.3: Global plasma resistance and Ohmic input power as a function of q_a at two different $\bar{n}_e$. R_P has a non-linear dependence on q_a with a significant decrease at $q_a \approx 0.55$

4.3 Magnetohydrodynamic Activity

The tokamak, RFP, and ULq plasmas exhibit very different mode activity in sustained conditions. This section summarizes observations of mode activity measured by the toroidal and poloidal arrays near the plasma edge. All toroidal and poloidal harmonic amplitudes and velocities discussed in this section refer to the B_P components.

At a typical $q_a \approx 2.5$ for a standard tokamak, magnetic fluctuations are dominated by small-wavenumber poloidal and toroidal harmonics. The dominant poloidal harmonic is by far the $m = 1$ having an amplitude of ~15 G and constant phase. Note that the poloidal array measures an increase in B_P on the inboard side of the plasma due to toroidicity, and this is reported as a high-amplitude, constant-phase $m = 1$ harmonic. The $m = 2, 3, 4$ harmonics have a much lower amplitude of $\leq$2 G. The largest toroidal harmonics are $n = 1, 2, 3$ with amplitudes $\leq$2.5 G and rotation velocities oscillating around zero. Tokamak plasmas exhibit a sawtooth cycle where a $m/n = 1/1$ kink is driven unstable in the core resulting in periodic collapses of core temperature, electron density, and current density profiles. This appears as large peaks in the $n = 1$ and $m = 2$ harmonics up to ~5 G occurring at a rate of ~1 kHz. Aside from the sawtooth cycle, harmonic amplitudes are steady but relatively small.

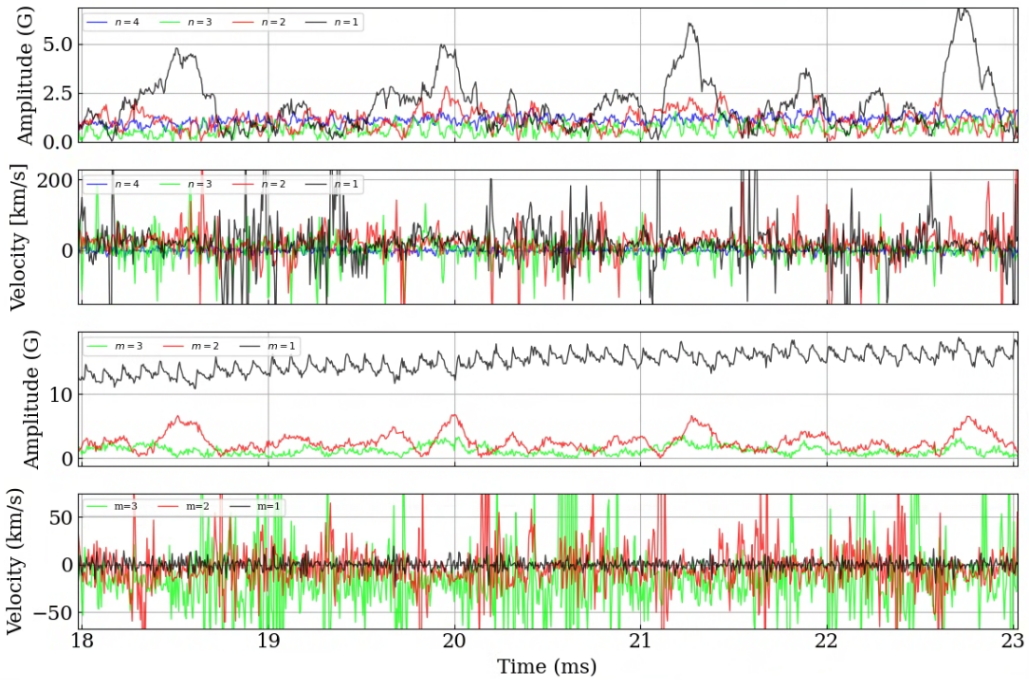

Figure 4.4: Typical B_P harmonic amplitudes and velocities over 5 ms of a steady 50 kA tokamak discharge with $q_a = 2.4$ and sawtooth cycle present. B_P at the edge is approximately 400 G

The velocities of these small amplitude harmonics are not well resolved and appear as high-frequency oscillations around a mean value of zero. An example of typical harmonic analysis of a standard tokamak is shown in Figure 4.4.

The RFP configuration is dominated by small-wavenumber poloidal harmonics and toroidal harmonics with larger-wavenumbers compared to the tokamak. Between sawtooth crashes, the dominant toroidal harmonics are $n = 5, 6, 7$ at $\sim$5 G, and these harmonics can lock in phase or rotate independently at speeds of order 10 km/s. Poloidal harmonics are again dominated by the $m = 1$ at $\sim$75 G; the next largest harmonic is the $m = 2$ at $\sim$20 G followed by $m = 3$ at $\leq$10 G. The magnetic and n_e fluctuations in the RFP are significantly higher amplitude than those in the tokamak, and they are especially large during a sawtooth crash. The RFP sawtooth mechanism is entirely different from the tokamak sawtooth. Because of the several $1/n$ rational surfaces across the plasma radius as well as the $m = 0$ resonant

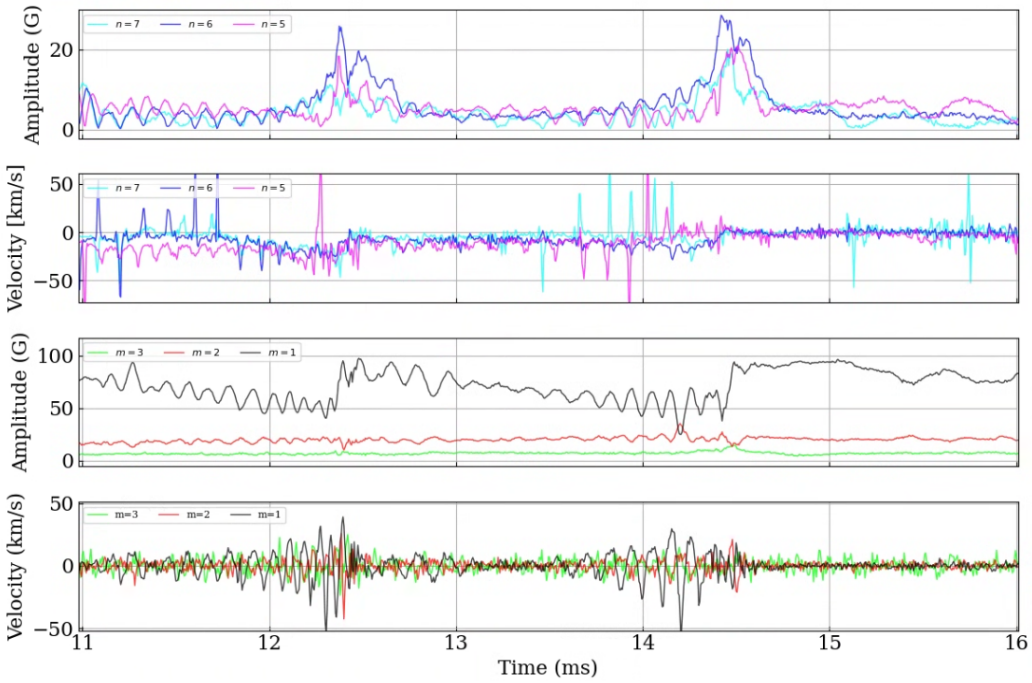

Figure 4.5: Typical B_P harmonic amplitudes and velocities over 5 ms of a steady RFP 350 kA discharge with $q_a = -0.05$ and two sawtooth crashes present. B_P at the edge is approximately 1400 G

surface at the reversal radius, magnetic island chains form on these rational surfaces, grow to the point of overlap, and trigger magnetic reconnection events seen as a sawtooth spike on all diagnostics. Notably, this results in a ∼15% sawtooth spike feature in the average B_T along with energization of both ions and electrons. This B_T effect and particle energization is absent or insignificant in the tokamak sawtooth cycle. During a sawtooth crash, the $n = 5, 6, 7$ harmonics ramp up in amplitude to 20 G and quickly decay back their steady values. The $m = 1$ amplitude slowly decays between sawteeth and quickly rises in amplitude at the event. For harmonics with sufficient mean amplitude and small fluctuations, rotation velocities are well resolved. An example of harmonic analysis during a sustained RFP discharge is shown in Figure 4.5.

MHD activity in the ULq regime is highly dependent on the value of q_a and the presence of major rational surfaces along the $q(r)$ profile. The major rational surfaces that can be

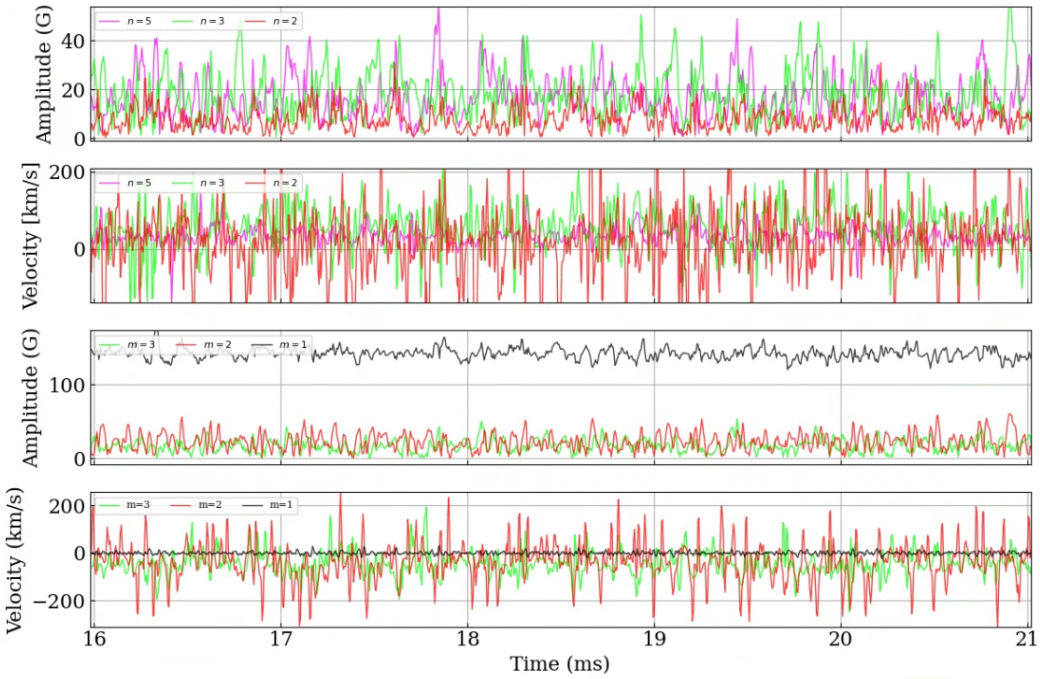

Figure 4.6: Typical B_P harmonic amplitudes and velocities over 5 ms of a steady ULq 180 kA discharge with $q_a \approx 0.65$. B_P at the edge is approximately 700 G

present in the discharges studied in this work include the m/n = 4/5, 3/4, 2/3, 3/5, 1/2, and 2/5. The largest poloidal harmonic is again always the $m = 1$ at 100-200 G. In the low-density operation regime, the largest poloidal and toroidal harmonics reflect the outermost major rational surfaces; however, their amplitudes are never steady. The dominant harmonic amplitudes fluctuate at several kHz about some mean value greater than zero and reach peaks up to 60 G. For a fixed value of q_a, the dominant harmonics can change when crossing from the low-density to the high-density regime, but this phenomenon has not been studied in detail. Due to the large high-frequency fluctuations in harmonic amplitudes, harmonic velocities are difficult to resolve in ULq plasmas. harmonic velocities can have mean values of 10's of km/s; but, without further analysis, it is not clear if these values are meaningful or a result of the noisy, fluctuating conditions. There is no sawtooth crash feature like in the RFP. An example of harmonic analysis during a steady ULq discharge is shown in Figure 4.6. Harmonics in ULq plasmas typically rotate independently without locking to other

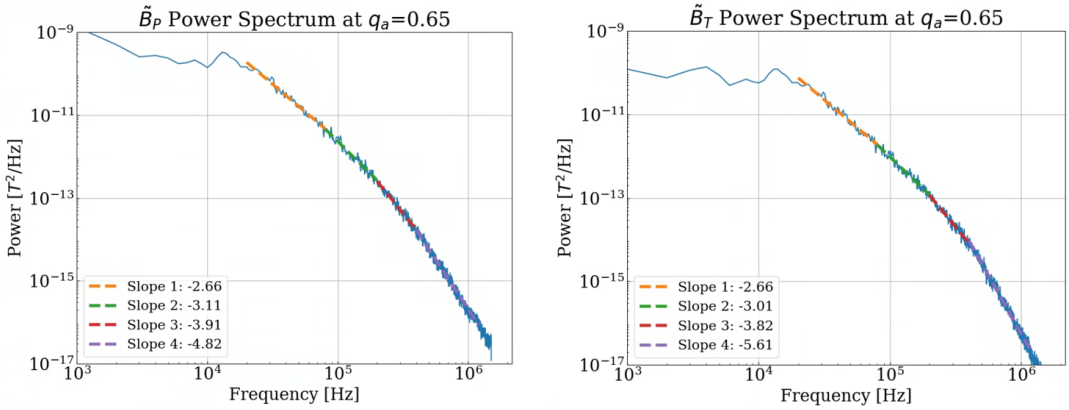

Figure 4.7: $\tilde{B}_P$ and $\tilde{B}_P$ fluctuation autopower spectra for the a $q_a = 0.65$ discharge measured by dense array coils.

harmonics or the vessel wall. However, when q_a is near values of $q_a = 0.5$ and $q_a = 1$, modes can spontaneously lock to the vessel wall which significantly perturbs the discharge. When this locking occurs, the $n = 1$ or $n = 2$ harmonic grows to very large amplitude and $\bar{n}_e$ increases by over an order of magnitude. These values of q_a have been avoided in this work due to this inconsistent behavior.

A plot of $\tilde{B}_P$ and $\tilde{B}_P$ fluctuation autopower measured by coils from the dense array for a $q_a = 0.65$ discharge is shown in Figure 4.7. Notice that the fluctuation amplitudes are highest at frequencies of 1-20 kHz, which corresponds the toroidal rotation frequency of the dominant $n = 3$ harmonic. Fluctuation amplitudes then decay with the rate of decay increasing with frequency. This change in slope indicates the onset of dissipation as the fluctuation cascade reaches ~100 kHz. It is shown in following chapters that fluctuation amplitudes in the 1-30 kHz band vary significantly with discharge parameters and appear to be associated with impurity heating.

4.4 Equilibrium Properties

The constant phase $m = 1$ perturbations are primarily due to the effect of toroidicity concentrating the flux density on the inboard side of the plasma. In all MST plasmas, B_P is

stronger on the inboard side than the outboard which is reported as an $m = 1$ harmonic. The amplitude of this inboard-outboard difference is influenced by the plasma internal inductance and by the outward Shafranov shift of the current density profile. The internal inductance reflects the shape of the current density profile. A more-peaked current density profile gives a higher internal inductance, and a broader current density profile gives a lower internal inductance. The poloidal field at the plasma surface as a function of poloidal angle is described by [15]

$$B_{P,a}(\theta) = B_{a,0}(1 + \frac{a}{R}\Lambda \cos\theta) \ , \tag{4.1}$$

where θ is the angle away from the outboard midplane, $B_{a,0}$ is the edge poloidal field at ± 90 degrees, $\frac{a}{R}$ is the inverse aspect ratio, and Λ is the poloidal asymmetry factor, defined as

$$\Lambda = \beta_P + \frac{l_i}{2} - 1 \ , \tag{4.2}$$

where β_P is the ratio of plasma pressure to the poloidal field magnetic pressure, and l_i is the internal inductance. In MST plasmas, Λ is always a negative value which gives a greater B_P on the inboard side than outboard. The tokamak has $\Lambda \approx -0.25$ and the ULq plasmas have $\Lambda \approx -0.6$. Since the $\beta_P \approx .01$ is small in these tokamak and ULq plasmas and likely not changing significantly, the large increase in the $m = 1$ amplitude and increase in $|\Lambda|$ indicate that ULq plasmas have much flatter current density profiles and lower l_i than the standard tokamak.

Line-averaged electron density $\bar{n}_e$ profiles in ULq also suggest flattening of the pressure profile. A comparison of radial $\bar{n}_e(r)$ profiles of a standard tokamak and ULq discharge with similar core $\bar{n}_e$ is shown in 4.8. Within ± 20 cm of the core, the profiles appear similar. Near mid-radius, the tokamak exhibits steep $\bar{n}_e$ gradients which trend towards an edge density of $\sim$10% of the core density. The ULq plasma also exhibits gradients beginning near mid-radius, but the gradients are much weaker than the tokamak's and trend towards an edge

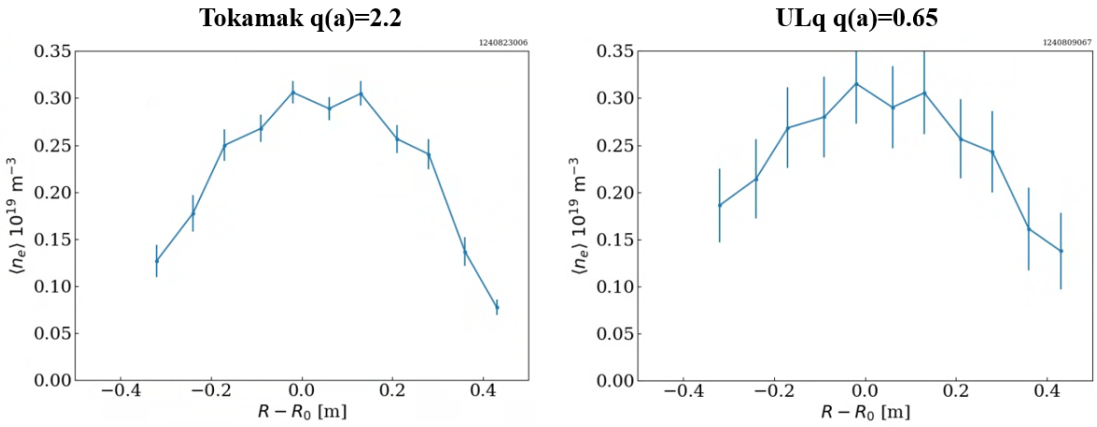

Figure 4.8: (Left) Standard tokamak $\bar{n}_e(r)$ profile. (Right) ULq line $\bar{n}_e(r)$ profile at $q_a \approx 0.65$. Density is averaged over 4 ms, and error bars represent standard deviations of the samples.

density of ∼33% of the core density. This is consistent with flattening of both the pressure and current density profiles in ULq plasmas. The tokamak and ULq plasmas appear to have similar Shafranov shifts of a few cm outboard from the geometric axis, and the ULq density profiles do not significantly skew inboard or outboard unless wall-locked modes are present. ULq plasmas are highly paramagnetic and can enhance the average B_T up to 50% of the applied B_T.

An estimate of the Mercier criterion (equation 1.5) as a function of minor radius for a $q_a = 0.65$ discharge is shown in Figure 4.9. This estimate is made assuming flat temperature profiles with $T_i = T_e = 100$ eV, the $\bar{n}_e(r)$ profile shown in 4.8, and a $q(r)$ profile similar to the profiles shown in 2.9 with $q_a = 0.65$ and $q_0 = 0.5$. Notice that much of the plasma is unstable or marginally stable to ideal interchange modes, and the only stable region lies towards the edge where significant magnetic shear is expected.

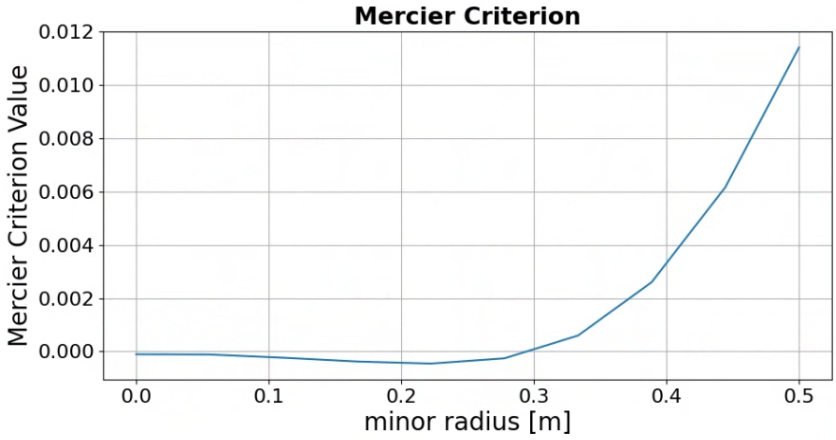

Figure 4.9: Plot of the Mercier criterion estimate for an ULq plasma with $q_a = 0.65$

4.5 Ion Heating

Ion heating in the standard tokamak is assumed to be entirely from collisional coupling to the Ohmic-heated electrons and is typically limited to $T_i \leq \frac{1}{2}T_e$. For low-performance tokamak plasmas in MST, impurity temperatures T_z are too low to resolve with the available diagnostic but is expected to be on the order of 10 eV.

Ion temperatures in the RFP are impacted by collisional coupling to electrons as well as anomalous ion heating with potentially several mechanisms being responsible. There is a continuous ion heating which tends to keep $T_z \approx T_e \approx$400 eV for a 400 kA RFP and also an impulsive ion heating coincident with each sawtooth crash. Impurity T_z can spike up to 3× the between-event value within 100 μs after a sawtooth event and then decay back to the steady value between events.

Impurity ions in ULq plasmas experience strong quasi-continuous heating. A time trace of B-IV ion temperature in an ULq discharge is shown in figure 4.10. $\bar{T}_z$ has been observed as high as $3\times T_e$. $\bar{T}_z$ is highly dependent on both q_a and $\bar{n}_e$. A plot of $\bar{T}_z$ as a function of q_a at fixed density is shown in Figure 4.11. $\bar{T}_z$ generally increases with decreasing q_a, and there is a factor of $\sim$2× increase at q_a= 0.65 followed by a factor of $\sim\frac{1}{2}\times$ decrease at q_a= 0.55.

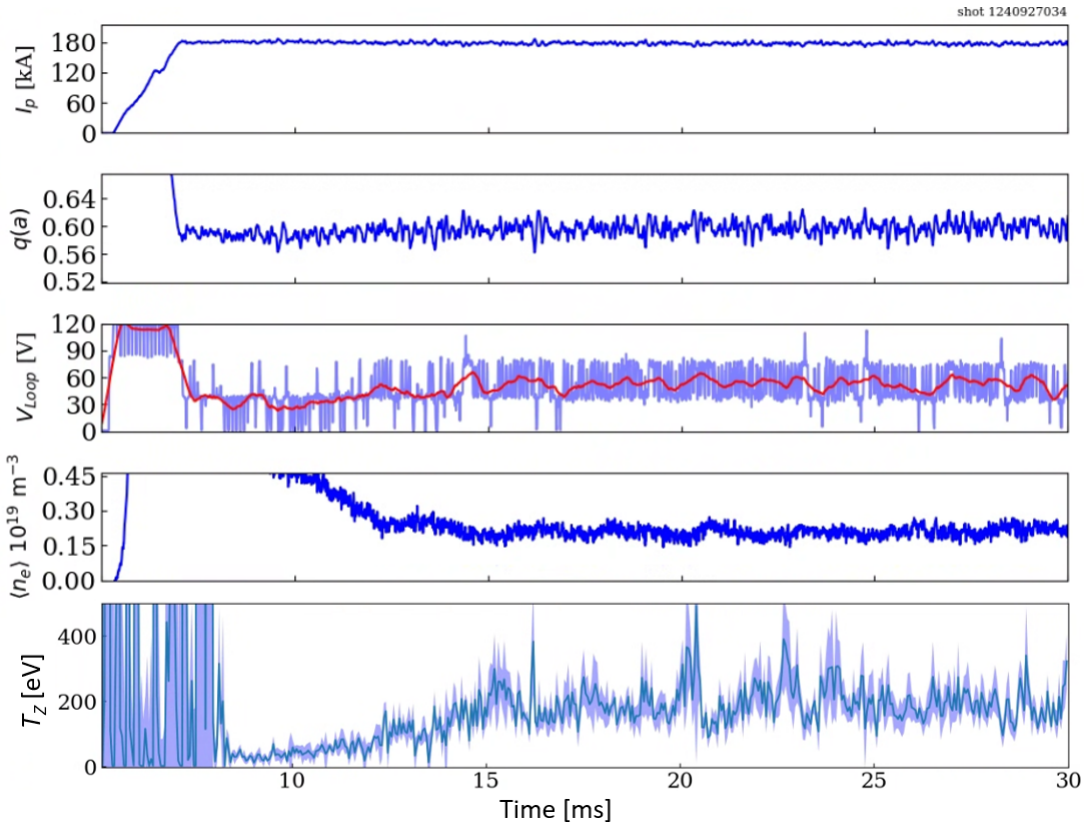

Figure 4.10: Discharge parameters and B-IV ion temperature as a function of time for a q_a ≈0.6 discharge.

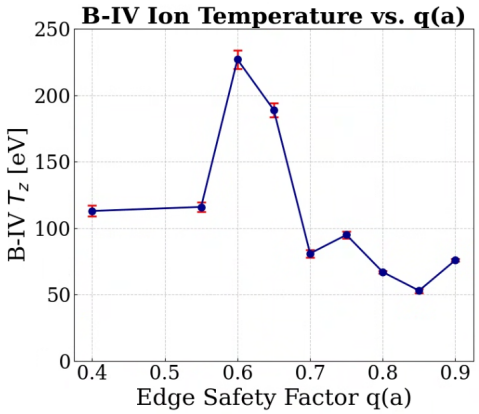

Figure 4.11: Boron-IV ion temperature versus q_a at fixed $\bar{n}_e$

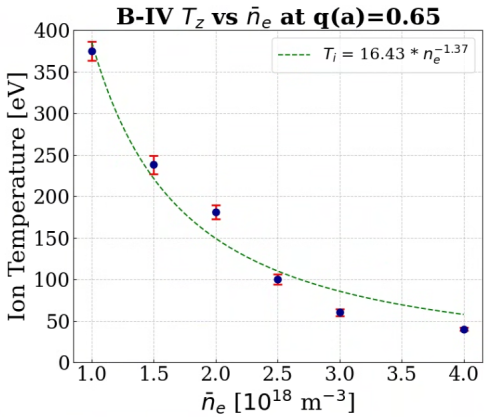

Figure 4.12: Boron-IV ion temperature versus $\bar{n}_e$ at $q_a = 0.65$.

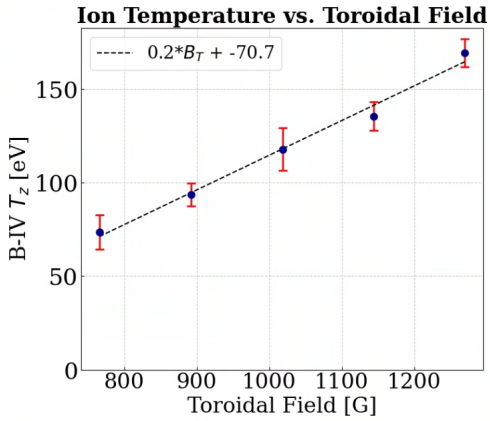

Figure 4.13: Boron-IV ion temperature versus toroidal field at fixed $q_a = 0.65$ and $\bar{n}_e$

Significantly-high T_z is only observed in the low-density ULq regime, and $\bar{T}_z$ increases with decreasing $\bar{n}_e$. A plot of $\bar{T}_z$ vs $\bar{n}_e$ at fixed q_a= 0.65 is shown in Figure 4.12. A roughly-linear dependence of $\bar{T}_z$ on equilibrium field and input power is also observed by scanning I_P and B_T together at fixed q_a, shown in Figure 4.13. The following chapter reports on the analysis of datasets obtained while performing these parameter scans.

4.6 Summary of ULq Properties

Startup of ULq plasmas can be challenging due to their high R_P and strong mode activity near $q(a) = 1$. Startup is most reproducible when the loop voltage, I_P ramp rate, and initial plasma density are maximized; and puffing a substantial amount of gas 5 ms before

beginning the ramp ensures the initial density is sufficient. Insufficient initial density or ramp rate results in bursts of x-rays and strong oscillations in $\bar{n}_e$ and I_P which prevent transition to the ULq regime. In sustained conditions, ULq plasmas have R_P a factor of 2-10× higher than the RFP and tokamak. R_P is highly dependent on q_a and was observed to increase roughly linearly with decreasing $\bar{n}_e$ for discharges with $\bar{n}_e < 5 \times 10^{18}\ m^{-3}$. Above this threshold $\bar{n}_e$, the trend inverts and R_P increases with increasing $\bar{n}_e$ which is the typical behavior for tokamak and RFP plasmas. In the low-density regime, ULq plasmas are minimally responsive to gas puffing such that large increases in fueling rates have little to no impact on $\bar{n}_e$, but in the high-density regime, a relatively small increase in fueling greatly increases $\bar{n}_e$. It is notable that this threshold $\bar{n}_e$ value is the same value where $\bar{T}_z$ becomes high enough to be resolved by the available diagnostic, and $\bar{T}_z$ increases with decreasing $\bar{n}_e$.

In ULq plasmas, B_P toroidal harmonic amplitudes can reach up to ∼5% of the edge B_P, significantly greater than the normalized harmonic amplitudes in the tokamak and RFP. The dominant harmonics tend to be those of helical modes whose value of m/n is closest to q_a. The harmonic amplitudes and rotation speeds are highly dependent on q_a, and the rotation speeds reach 10's of km/s in the low-density regime. The direction of harmonic rotation is typically opposite to the direction of rotation in the RFP and tokamak. Both the $\bar{n}_e(r)$ profiles and the poloidal asymmetry factors of ULq plasmas indicate that the current density profiles and pressure profiles are flattened compared to the tokamak and RFP.

Impurity temperatures in ULq plasmas are anomalously high in the low-density regime with $\bar{T}_z$ up to $3\times T_e$ observed. When other parameters are steady, $\bar{T}_z$ is nearly constant in time and does not appear correlated with fluctuations in I_P or B_T. Discrete relaxation events like the RFP sawtooth and tokamak sawtooth are not observed in ULq plasmas. $\bar{T}_z$ has a strong dependence on q_a, $\bar{n}_e$, and equilibrium magnetic field strength.

Chapter 5

Experiments, Data, and Analysis

This chapter reports on the experimental observations and data sets obtained in this work. Several parameter scans are performed in order to coarsely characterize the discharge behavior and impurity ion temperature variation in ULq plasmas. The data points from these scans represent 4 ms averages during periods of steady parameters which satisfy the requirements for the scan. These time windows are much greater than the typical ULq plasma energy confinement time of order 100 μs, but some of the measurements have considerable uncertainty due to the limited data set for time averaging. Still, these scans do provide insight into how the magnetic fluctuations, impurity temperature, and density fluctuations vary with discharge parameters. For each of the coarse parameter scans, data is presented for line-averaged impurity ion temperature $\bar{T}_z$, B_P toroidal harmonic amplitudes, B_P toroidal harmonic frequencies, B_P and B_T fluctuations, and $\bar{n}_e$ fluctuations. First, the edge safety factor q_a is scanned at fixed $\bar{n}_e$ and toroidal field B_T by varying only the the plasma current I_P. Second, I_P and B_T is fixed for a constant q_a while $\bar{n}_e$ is varied by adjusting gas puffing. Third, $\bar{n}_e$ and edge safety factor are held constant while varying B_T and I_P at a fixed ratio to scan the equilibrium magnetic field and Ohmic input power.

After the coarse scans, detailed fluctuation analysis for select q_a values of interest are

presented. These data sets are obtained from several repeated discharges with total averaged time typically being about 40 ms. Autopower, wavenumber, and coherence spectra from 1 cm spaced dense array coils at the edge are presented to characterize the fluctuations up to 1 MHz. This is followed by frequency analysis of toroidal array coils and insertable probe coils to characterize edge and internal magnetic fluctuations of 1-100 kHz, the frequency band where significant variation is observed.

Frequency analysis on the FIR interferometer chord signals is presented in order to characterize the $\bar{n}_e$ fluctuations for the select q_a cases. This data set includes autopower spectra of the $\bar{n}_e$ fluctuations, coherence spectra for chords with different radial separation, and coherence spectra between edge $\tilde{B}_P$ and $\bar{n}_e$ fluctuations.

Finally, frequency analysis from the capacitive probe measurements in the select q_a cases is presented to characterize the plasma potential $\tilde{\Phi}_P$ and radial electric field $\tilde{E}_r$ fluctuations, the coherence between $\tilde{\Phi}_P$ and edge $\tilde{B}_P$, the coherence between $\tilde{\Phi}_P$ and $\bar{n}_e$ fluctuations, and the dependence of $\tilde{\Phi}_P$ and $\tilde{E}_r$ on $\bar{n}_e$. This chapter concludes with a summary and discussion of the observations.

5.1 Edge Safety Factor Scan

The edge safety factor scan over the range $0.4 \leq q_a \leq 0.9$ is performed at an applied B_T = 0.13 T. $\bar{n}_e$ was fixed at 2×10^{18} m^{-3} for this scan; this value is chosen because it is low enough to produce high $\bar{T}_z$ but high enough to suppress electron runaway and allow for good discharge reproducibility. Plots of core B-IV $\bar{T}_z$, B_P toroidal harmonic amplitudes, and B_P toroidal harmonic frequencies vs. q_a are shown in Figure 5.1. Note that data for q_a values of 0.5 and 0.95 are not present. These values of q_a are avoided due to the tendency of their modes to spontaneously lock to the vessel wall and greatly perturb the discharge. The B-IV $\bar{T}_z$ plot shows a strong dependence of impurity temperature on q_a with a large increase at

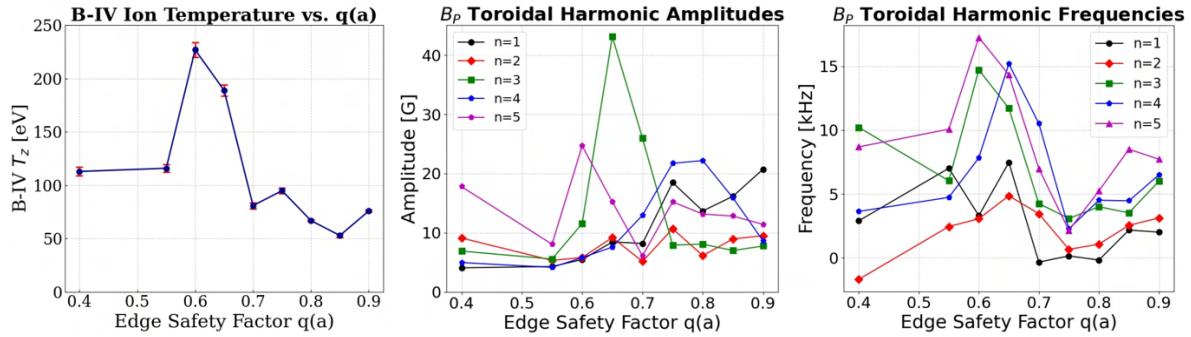

Figure 5.1: (Left) A plot of average B-IV impurity temperature vs. q_a. (Middle) A plot of B_P toroidal harmonic amplitudes vs. q_a. (Right) A plot of B_P toroidal harmonic frequencies vs. q_a.

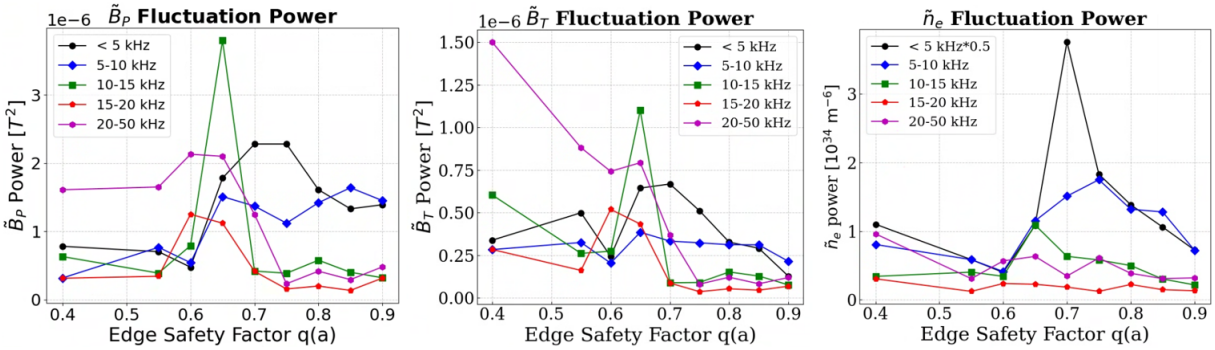

Figure 5.2: (Left) A plot of $\tilde{B}_P$ fluctuation power vs. q_a, measured by dense-array coil. (Middle) A plot of $\tilde{B}_T$ fluctuation power vs. q_a, measured by dense array coil. (Right) A plot of core (chord #6, "P06") line-averaged $\tilde{n}_e$ fluctuation power vs. q_a (note that the <5 kHz bin has been scaled by 0.5 for readability).

$q_a = 0.6, 0.65$. Notice that the peaks in B_P amplitudes for the $n = 3, 5$ harmonics align with the peak in $\bar{T}_z$, and these peaks occur when the q_a value is near the major rational values of 3/5 and 2/3. Also note that the $n = 3, 5$ frequencies have peak values of ∼15 kHz at $q_a \approx 0.6$, the same q_a value where $\bar{T}_z$ peaks.

Fluctuation power spectra also vary significantly with q_a. Figure 5.2 shows a plot of $\tilde{B}_P$, $\tilde{B}_T$, and $\bar{n}_e$ fluctuation power in several frequency bins for the q_a scan. Notice that the higher-frequency magnetic fluctuations, particularly the 10-15, 15-20, and 20-50 kHz bins, show a trend similar to $\bar{T}_z$. The increase in 10-20 kHz magnetic fluctuation amplitudes near $q_a = 0.65$ is consistent with the increase in $n = 3$ harmonic frequency to ∼15 kHz. There is

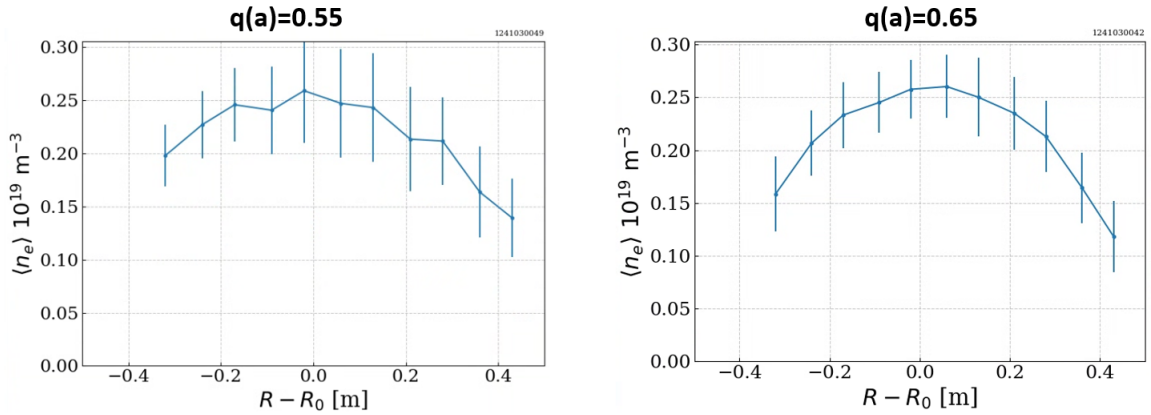

Figure 5.3: $\bar{n}_e(r)$ profiles for $q_a = 0.55$ and 0.65. $\bar{n}_e$ is averaged over 4 ms, and the error bars represent the standard deviations of the data points. R_0 refers to the geometric axis.

also a similar trend between $\bar{n}_e$ fluctuation amplitudes and $\bar{T}_z$ for the 10-15 and 20-50 kHz bins. However, note that the <5 kHz bin has been scaled down by a factor of 2× in this plot for readability; so, the highest-amplitude $\bar{n}_e$ fluctuations do not show a trend similar to that of $\bar{T}_z$.

An interesting observation in the q_a scan is the significant decrease in $\bar{T}_z$ and fluctuation amplitudes as q_a is decreased from 0.6 to 0.55. The $\bar{n}_e(r)$ profile in ULq plasmas is flattened compared to the standard tokamak, but there this always some degree of core-peaking which is mostly independent of q_a for the $\bar{n}_e \leq 4 \times 10^{18}\ m^{-3}$ discharges studied in this work. Figure 5.3 shows a comparison of the $\bar{n}_e(r)$ profiles for discharges with $q_a = 0.55$ and 0.65. $\bar{T}_z(r)$ profiles for the $q_a = 0.55$ and $q_a = 0.65$ cases are shown in Figure 5.4. The $q_a = 0.55$ case has lower average $\bar{T}_z$ and exhibits temperature peaking near the outboard mid-radius, and the $q_a = 0.65$ discharge exhibits a core-peaked $\bar{T}_z(r)$ profile which is nearly symmetric about the expected location of the magnetic axis. The $q_a = 0.55$ $\bar{T}_z(r)$ profile is surprising since the $\bar{n}_e(r)$ does not appear to have an outboard shift. This could be caused by a helical structure lying on an outboard-shifted magnetic axis, but explaining this feature of the $q_a = 0.55$ discharge will require future work.

In summary, the scan of I_P over the range of $0.4 \leq q_a \leq 0.9$ shows that the discharge

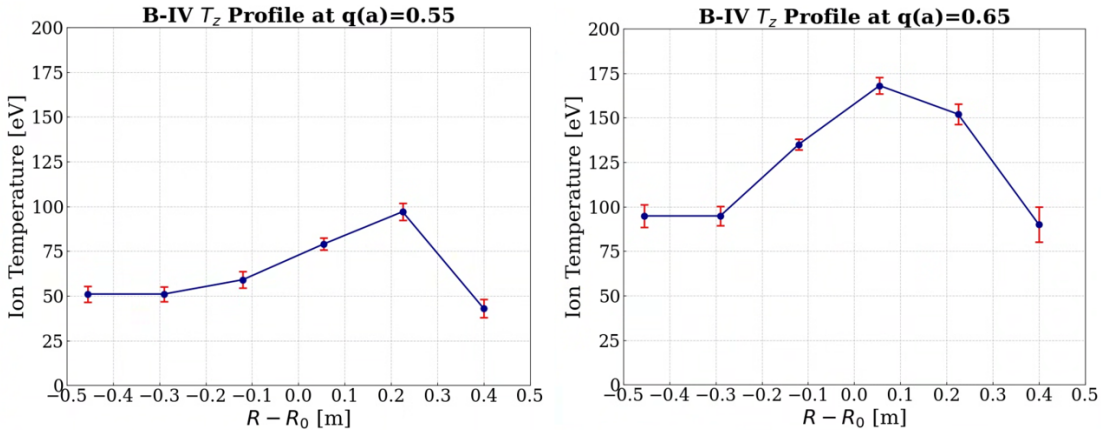

Figure 5.4: B-IV $\bar{T}_z(r)$ profiles for q_a =0.55 and 0.65. Each profile was constructed by taking two simultaneous measurements at adjacent radial locations and shifting those locations over 3 repeated discharges. The measurements were averaged over 4 ms during a period of steady parameters. R_0 refers to the geometric axis.

behavior is strongly dependent on the value of q_a. $\bar{T}_z$ and R_P tend to increase as q_a is lowered towards $q_a \approx 0.65$. Decreasing to $q_a \approx 0.6$ results in a decrease in R_P and an increase in $\bar{T}_z$, and decreasing further to $q_a \approx 0.55$ results in a significant decrease in R_P and $\bar{T}_z$. The trend in $\bar{T}_z$ is similar to the trend in $\tilde{B}_T$ and $\tilde{B}_P$ amplitudes at 10-50 kHz, and the strong fluctuations with frequencies of 10-20 kHz are consistent with the rotation frequencies of the dominant $n = 3, 5$ harmonics. The trend in high-frequency $\bar{n}_e$ fluctuation amplitudes is similar to the trend in $\bar{T}_z$, but not for the highest-amplitude fluctuations which have frequencies below 10 kHz. These observations suggest that the rotation of large-amplitude helical resonant modes and the resulting fluctuations are associated with the impurity ion heating.

5.2 Plasma Density Scan

A scan of $\bar{n}_e$ over the range $1 \leq \bar{n}_e \leq 4 \times 10^{18}\ m^{-3}$ is performed at an applied $B_T = 0.13$ T and plasma current of $I_P = 180$ kA. The value of $q_a = 0.65$ is chosen for this scan because it exhibits high $\bar{T}_z$ and its plasma conditions permit good $\bar{T}_z$ measurements. Plots of B-IV $\bar{T}_z$

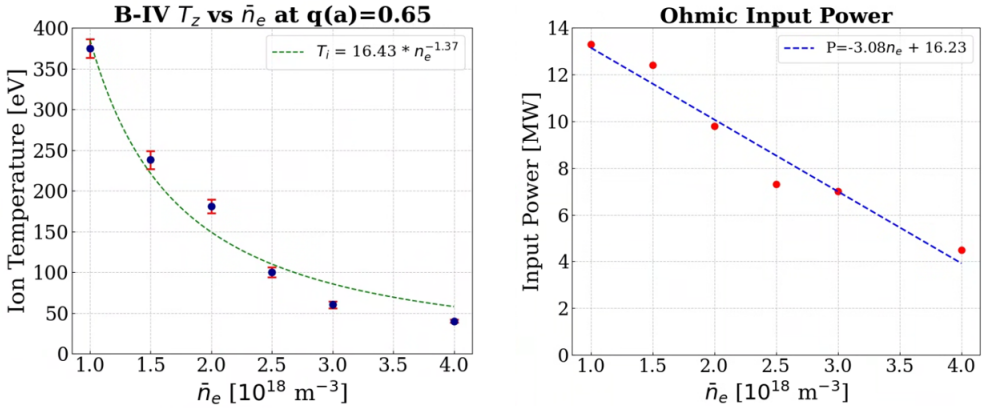

Figure 5.5: (Left) Plot of B-IV impurity temperatures vs. $\bar{n}_e$. (Right) Plot of Ohmic input power vs. $\bar{n}_e$.

and Ohmic input power for the $\bar{n}_e$ scan are shown in Figure 5.5. Notice that $\bar{T}_z$ rises greater than linearly with decreasing $\bar{n}_e$ with an approximate scaling of $\bar{T}_z \propto \bar{n}_e^{-4/3}$, and Ohmic input power increases roughly linearly as $\bar{n}_e$ is decreased. This behavior is not observed in tokamaks or RFP plasmas which generally exhibit decreasing input power with decreasing $\bar{n}_e$. For ULq plasmas with $\bar{n}_e \geq 5 \times 10^{18}\ m^{-3}$, the trend inverts and Ohmic input power increases with increasing $\bar{n}_e$. It is notable that the low-density discharges which exhibit the inverse relationship between $\bar{n}_e$ and input power are also the discharges where strong impurity heating is observed.

Magnetic fluctuations also vary significantly with $\bar{n}_e$. Figure 5.6 shows plots of B_P toroidal harmonic frequencies and amplitudes for the $\bar{n}_e$ scan. The B_P toroidal harmonic amplitudes do not vary significantly throughout the scan and do not exhibit clear trend with $\bar{n}_e$. However, the toroidal rotation frequencies of the dominant $n = 3, 5$ harmonics show a clear trend of increasing with decreasing $\bar{n}_e$ which is similar to the trend in $\bar{T}_z$. These rotation frequencies correspond to rotation velocities of 15 to 45 km/s for the $n = 3$ harmonic.

Figure 5.7 shows the $\tilde{B}_P$, $\tilde{B}_T$ and $\bar{n}_e$ fluctuation power for the $\bar{n}_e$ scan. For the $\tilde{B}_P$ fluctuations, there is a trend of <10 kHz fluctuation amplitudes decreasing with decreasing $\bar{n}_e$ while high-frequency fluctuations at 20-50 kHz increase with decreasing $\bar{n}_e$. The intermediate

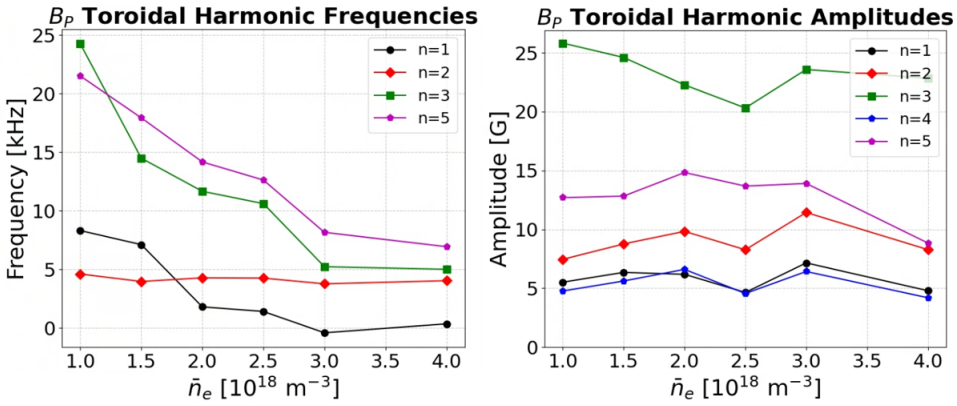

Figure 5.6: (Left) Plot of B_P toroidal harmonic frequencies vs. $\bar{n}_e$. (Right) Plot of B_P toroidal harmonic amplitudes vs. $\bar{n}_e$.

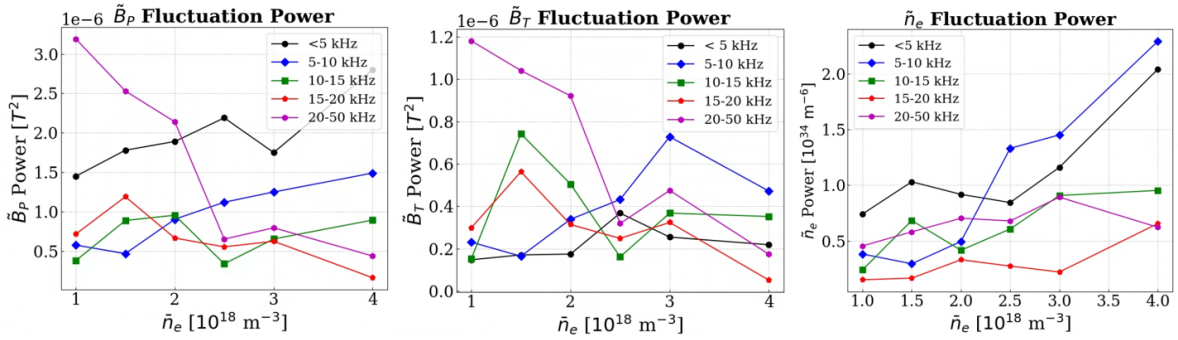

Figure 5.7: (Left) A plot of $\tilde{B}_P$ fluctuation power vs. $\bar{n}_e$, measured by dense-array coil. (Middle) A plot of $\tilde{B}_T$ fluctuation power vs. $\bar{n}_e$, measured by dense array coil. (Right) A plot of core (chord #6, "P06") line-averaged $\tilde{n}_e$ fluctuation power vs. $\bar{n}_e$.

frequency bins do not show a clear trend likely due to the broadband structure of the spectra, the size of the frequency bins, and the limited data set for time-averaging. The $\tilde{B}_T$ fluctuation amplitude trends are not as clear as the $\tilde{B}_P$ trends, but there is still a consistent increase in 20-50 kHz $\tilde{B}_T$ fluctuation amplitudes with decreasing $\bar{n}_e$. The $\bar{n}_e$ fluctuation amplitudes show a trend of decreasing with decreasing $\bar{n}_e$, especially for the dominant fluctuations with frequencies <10 kHz. Notice that at higher $\bar{n}_e$ the spectra are dominated by 1-10 kHz fluctuations, and the spectra become more broadband as $\bar{n}_e$ decreases.

In summary, the $\bar{n}_e$ scan shows that there is a greater than linear increase in B-IV $\bar{T}_z$ as $\bar{n}_e$ decreases while Ohmic input power increases roughly linearly. This suggests that the anomalous impurity heating power is increasing with decreasing $\bar{n}_e$, and the increasing $\bar{T}_z$

cannot be attributed to enhanced energy confinement. The trend in $\bar{T}_z$ is similar to the trend of increasing rotation frequency of the dominant $n = 3$ B_P harmonic and an increase in amplitude of broadband magnetic fluctuations of 20-50 kHz. At high $\bar{n}_e$, the $\bar{n}_e$ fluctuation amplitudes are highest at frequencies <10 kHz, but the spectra become more broadband at low $\bar{n}_e$. These observations suggest that the increase in $\bar{T}_z$ and the increase in high-frequency magnetic fluctuation amplitudes are associated with the increasing rotation speeds of large-amplitude resonant modes or the conditions which cause the increase in rotation frequencies.

5.3 Toroidal Field Scan

A scan of B_T and I_P over the range $766 \leq B_T \leq 1270$ G and $108 \leq I_P \leq 180$ kA is performed to vary the equilibrium magnetic field and Ohmic input power at a fixed $q_a = 0.65$. Plasma density is held constant at $\bar{n}_e = 2 \times 10^{18}$ m^{-3}. Plots of B-IV $\bar{T}_z$, R_P, and Ohmic input power for the B_T scan is shown in Figure 5.8. $\bar{T}_z$ increases approximately linearly with increasing B_T while the global plasma resistance is nearly constant and Ohmic power increases quadratically.

Plots of B_P toroidal harmonic amplitudes and frequencies through the B_T scan are shown

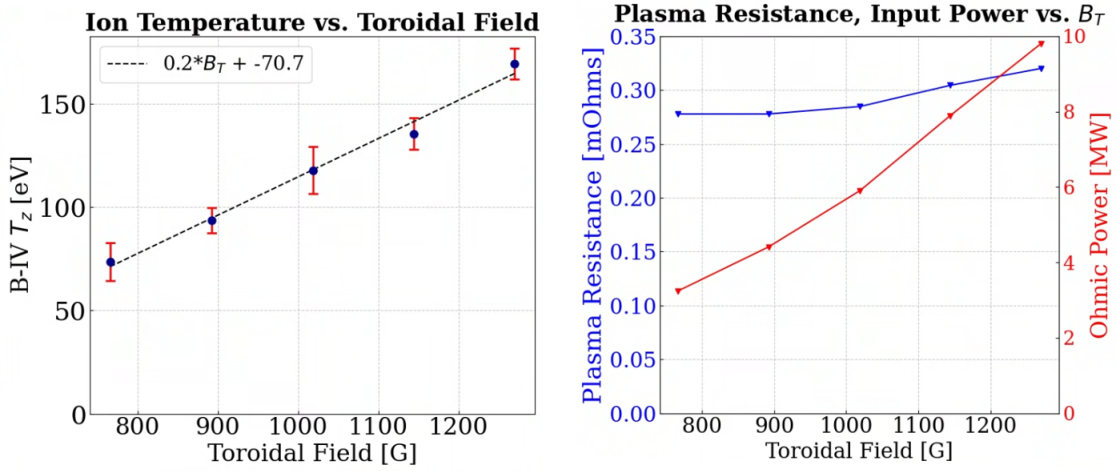

Figure 5.8: (Left) B-IV impurity temperature vs. B_T. (Right) Global plasma resistance and Ohmic input power vs. B_T.

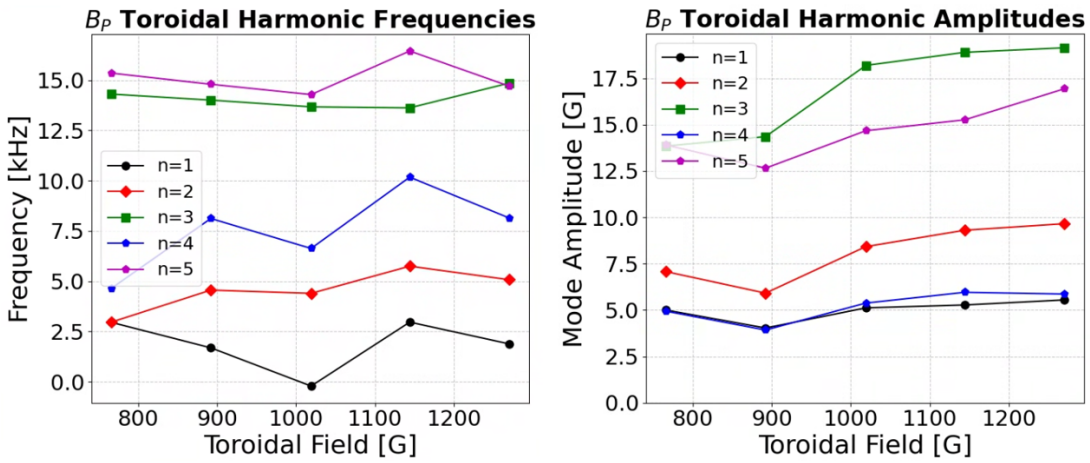

Figure 5.9: (Left) Plot of B_P toroidal harmonic frequencies vs. B_T. (Right) Plot of B_P toroidal harmonic amplitudes vs. B_T.

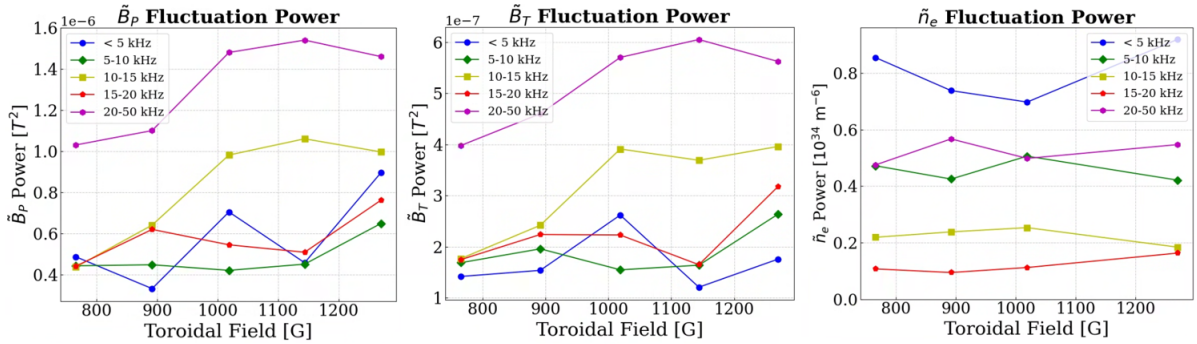

Figure 5.10: (Left) A plot of $\tilde{B}_P$ fluctuation power vs. B_T, measured by dense-array coil. (Middle) A plot of $\tilde{B}_T$ fluctuation power vs. B_T, measured by dense array coil. (Right) A plot of core (chord #6, "P06") line-averaged $\tilde{n}_e$ fluctuation power vs. B_T.

in Figure 5.9. The B_P toroidal harmonic frequencies are nearly constant with increasing B_T, and there is a slight increase in amplitudes of the dominant $n = 3, 5$ harmonics. However, normalized fluctuation amplitudes decrease slightly.

Figure 5.10 shows plots of $\tilde{B}_P$, $\tilde{B}_T$ and $\bar{n}_e$ fluctuation power for the B_T scan. For the $\tilde{B}_P$ and $\tilde{B}_T$ fluctuations, there is a trend of increasing amplitudes with increasing B_T for fluctuations in the 10-15 kHz and 20-50 kHz bands, and normalized amplitudes remain nearly constant. The $\tilde{n}_e$ fluctuation amplitudes are nearly constant and exhibit no trend with increasing B_T.

In summary, increasing B_T at fixed q_a and $\bar{n}_e$ results in a linear increase in $\bar{T}_z$ and

quadratic increase in Ohmic input power while R_P remains nearly constant. As B_T increases, the dominant B_P toroidal harmonic amplitudes increase slightly while their frequencies remain nearly constant. High-frequency magnetic fluctuation amplitudes increase with increasing B_T, but the $\bar{n}_e$ fluctuation amplitudes show no significant change. These observations suggest that the increasing $\bar{T}_z$ is associated with the increase in 10-50 kHz magnetic fluctuation amplitudes and possibly also an increase in impurity energy confinement time.

5.4 Fluctuation Analysis of Select Edge Safety Factor Values

Fluctuation analysis in this section focuses on select q_a values for which several repeated shots were performed and long periods of steady parameters were maintained, with a total of ∼40 ms averaged typically. The discharges analyzed in this section have edge safety factors of $q_a = 0.7$, 0.65, and 0.55. These q_a values were chosen because they have comparable I_P and there is a significant change in $\bar{T}_z$ among them. First, analysis of fluctuations measured by the toroidal array and dense array coil sets characterizes the frequency spectra and spatial scale of magnetic fluctuations at the plasma edge. Next, analysis of internal magnetic fluctuations measured with an insertable probe array is presented to show how the radial profile of magnetic fluctuation spectra varies with q_a. Then, frequency analysis of the $\bar{n}_e$ fluctuations is presented which characterizes the radial profile of the $\bar{n}_e$ autopower spectra, coherence between interferometer chords, and coherence between $\bar{n}_e$ fluctuations and magnetic fluctuations. Finally, analysis of capacitive probe measurements is presented to characterize the plasma potential Φ_P and radial electric field E_r fluctuation amplitudes and spectra. This includes the variation of their spectra with q_a and $\bar{n}_e$, the coherence between $\tilde{\Phi}_P$ and edge $\tilde{B}_P$, the coherence between $\tilde{\Phi}_P$ and $\bar{n}_e$ fluctuations, and the coherence between $\tilde{E}_r$ measurements with radial separation.

5.4.1 Magnetic Fluctuations at the Plasma Edge

The dense array coil set provides edge $\tilde{B}_P$ and $\tilde{B}_T$ fluctuation measurements with a bandwidth of 3 MHz and minimum coil separation of 1 cm. A plot of the $\tilde{B}_P$ and $\tilde{B}_T$ autopower spectra for the three q_a cases is shown in Figure 5.11. Notice the broad spectra and that for all cases the slope of the spectrum is increasing in magnitude with frequency, suggesting that a fluctuation cascade with some frequency-dependent or wavelength-dependent dissipation is involved. This effect is especially noticeable for the q_a =0.55 case which shows a large change in slope near 90 kHz, which suggests the onset of dissipation. The $\tilde{B}_P$ and $\tilde{B}_T$ fluctuation spectra display similar features for each q_a case, but the $\tilde{B}_T$ fluctuations tend to be lower amplitude but within an order of magnitude of the $\tilde{B}_P$ amplitudes. The region of the spectra which vary significantly between q_a cases is the 5-30 kHz band. The q_a =0.7 case spectra peak near 4 kHz, and the q_a = 0.65 case has its peak shifted to 15 kHz. The q_a = 0.65 case, which has the highest $\bar{T}_z$, also has the highest fluctuation amplitudes in the 10-20 kHz band. The q_a = 0.55 case has significantly lower fluctuation amplitudes below 50 kHz, but it has slightly higher amplitudes than the other two cases for frequencies between 50 and 100 kHz.

For the q_a = 0.65 case, plots of the coherence and wavenumber spectra between two B_P coils with 1 cm separation and between two B_T coils with 1 cm separation are shown in Figure 5.12. Note that the pitch angle of the equilibrium field for this case is approximately 27° at the edge. Both $\tilde{B}_T$ and $\tilde{B}_P$ show strong coherence for fluctuations up to 1 MHz. In the $\tilde{B}_T$ coherence spectrum, the feature near 750 kHz is due to noise pickup from the MST power supplies and should be disregarded. Notice that the toroidal and poloidal wavenumbers increase with frequency and saturate near 20 radian/m; this wavenumber saturation is not observed in RFP plasmas until frequencies over 1 MHz at a wavenumber

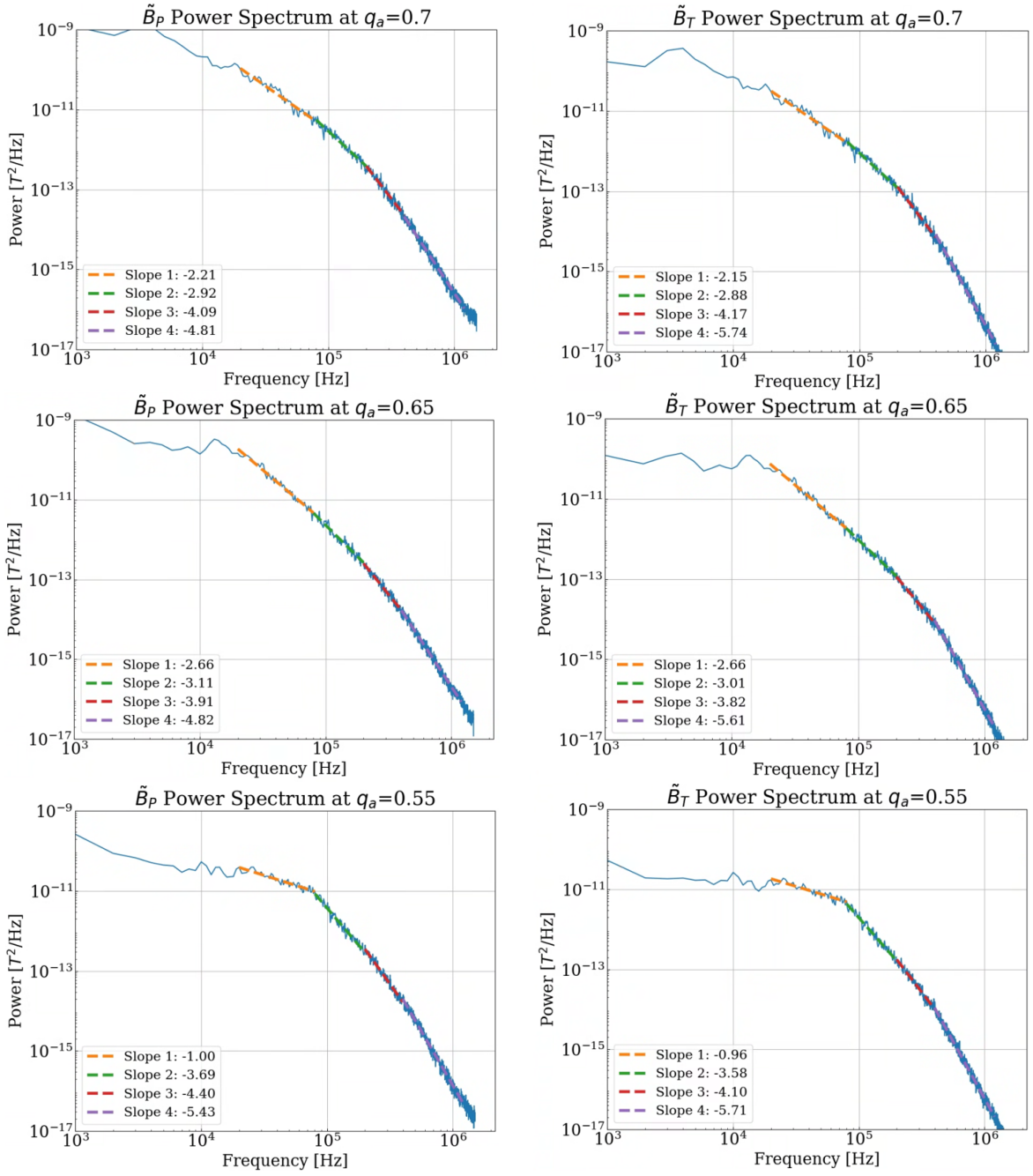

Figure 5.11: $\tilde{B}_P$ (Left) and $\tilde{B}_T$ (Right) autopower spectra from dense array coils at the plasma edge for the three q_a cases.

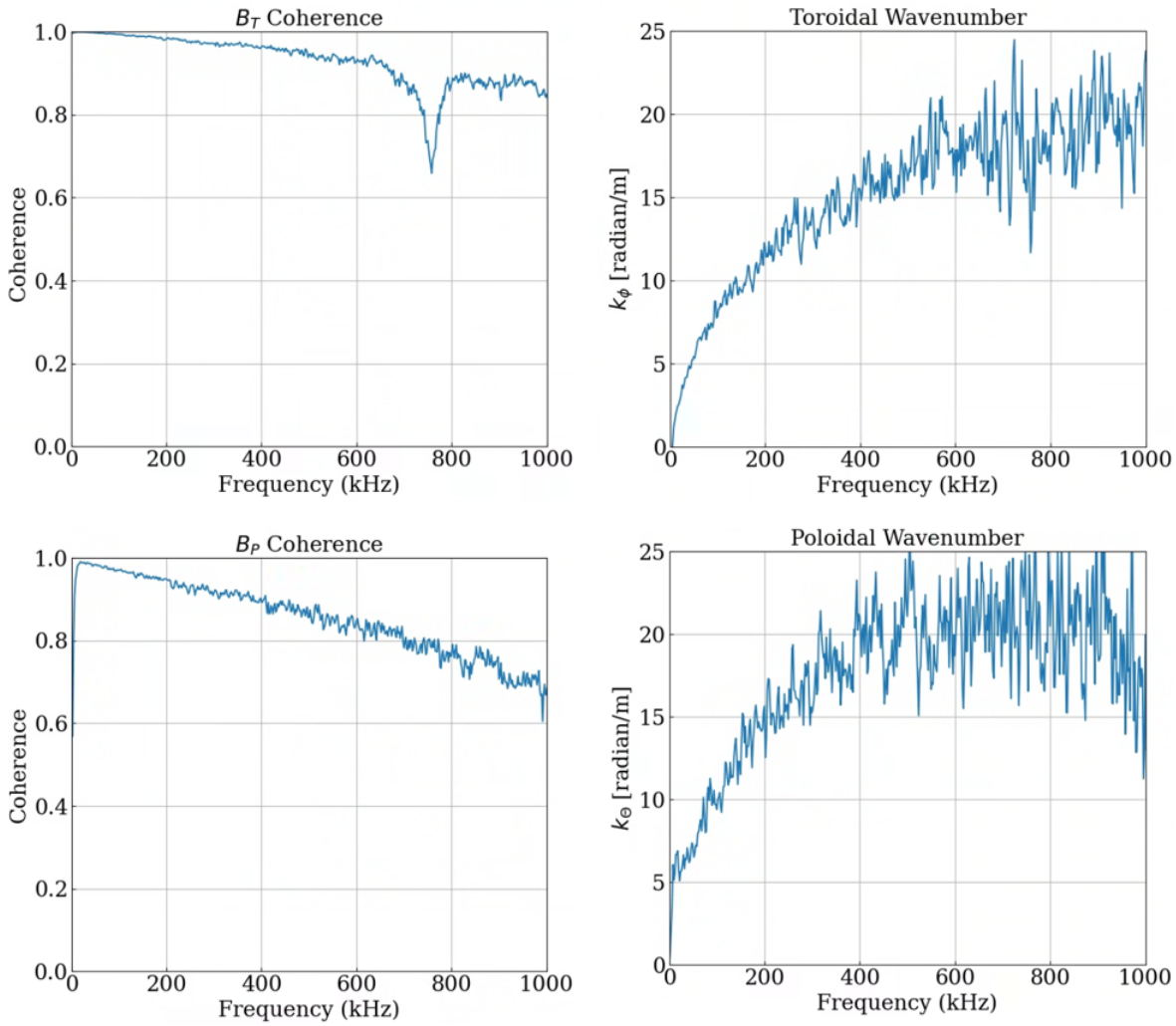

Figure 5.12: $\tilde{B}_T$ and $\tilde{B}_P$ coherence and wavenumber spectra for the q_a =0.65 discharge. B_T coils have a toroidal separation of 1 cm, and B_P coils have poloidal separation of 1 cm. The feature at 750 kHz in the B_T coherence spectrum is due to power supply noise pickup and should be disregarded.

of order 100 radian/m. The wavelengths of these fluctuations in ULq plasmas vary from meters at low frequency to about 30 cm at high frequency. Using the relation for the phase velocity of $v_{ph} = \omega/k$ gives phase velocities of 45-65 km/s for the 50-100 kHz fluctuations. At 1 MHz, phase velocities are approximately 300 km/s, which is much less than the Alfven speed estimate of 2000 km/s.

Linear plots of the autopower spectra measured by B_P and B_T toroidal array coils for the three q_a cases are shown in Figure 5.13. These signals are analog-integrated, and they

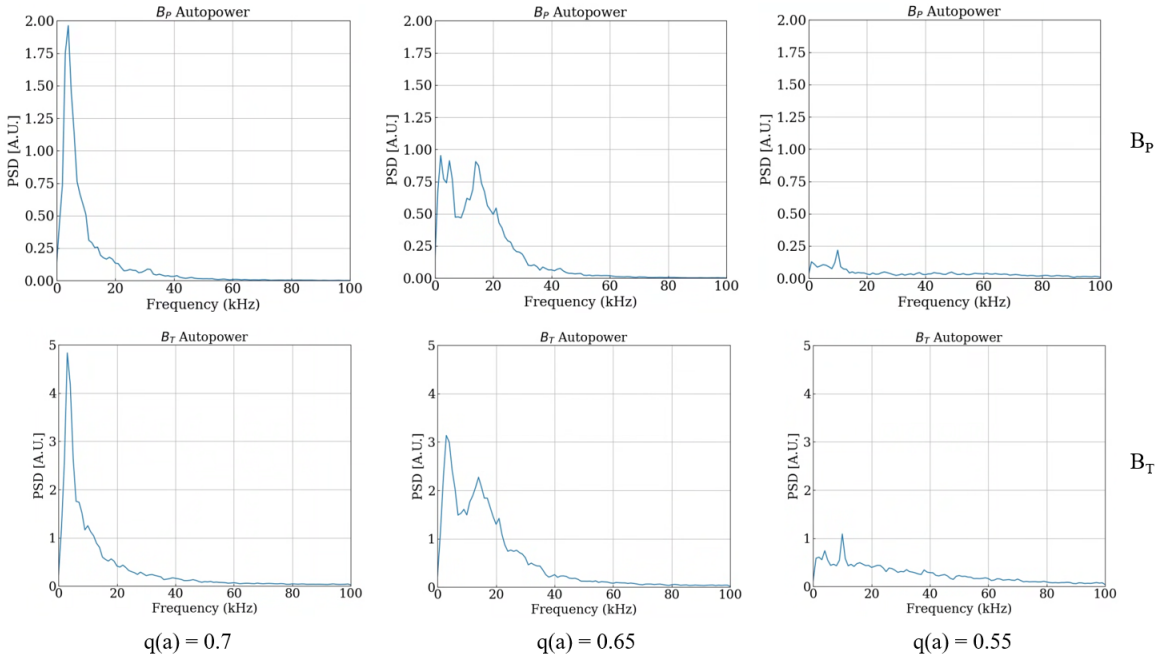

Figure 5.13: $\tilde{B}_P$ and $\tilde{B}_T$ autopower spectra measured by toroidal array coils for the three q_a cases. The units of the vertical axis are arbitrary and not equal for the $\tilde{B}_T$ and $\tilde{B}_P$ plots.

have sufficient bandwidth for the frequency range shown. The analog-integrated signals more accurately measure low-frequency activity, which tends to be noisy in the numerically-integrated $\dot{B}$ signals from the dense array. Each q_a case has similar spectra for $\tilde{B}_P$ and $\tilde{B}_T$ fluctuations, but the spectra change significantly as q_a is varied. The q_a =0.7 case has the largest amplitude fluctuations with a peak near 4 kHz and no discernible features at higher frequencies. This is consistent with the observations from the q_a scan of the $n = 3$ harmonic being dominant with a frequency of a few kHz. When q_a is decreased to 0.65, the low-frequency peak decreases by about 50% and a broadband peak of similar amplitude appears near 17 kHz. This is also consistent with q_a scan data which shows growth of the $n = 3$ harmonic with its frequency increasing to ∼15 kHz. Decreasing q_a further to 0.55 results in a significant decrease in low-frequency fluctuation amplitudes and slight increase in higher-frequency fluctuation amplitudes. The narrow peak at 10 kHz is due to the 10 kHz feedback power supply driving I_P and B_T. This 10 kHz peak is not observed in the other

cases since their fluctuation amplitudes around 10 kHz are large enough to obscure the peak.

These measurements at the plasma edge are less sensitive to fluctuations originating near the core, where greater $\bar{T}_z$ is observed, which motivates measurements with the insertable probe coil array to characterize the internal magnetic fluctuations.

5.4.2 Internal Magnetic Fluctuations

Several discharges were repeated with the magnetic coil array probe inserted to 35 cm within the plasma edge at a 15° angle above the outboard midplane at 180° toroidal. These discharges all have densities of $1.5 \leq \bar{n}_e \leq 2 \times 10^{18}\ m^{-3}$. It must be noted that the discharge behavior when the probe is inserted may be different from those without the probe. Particle transport appears to change significantly such that $\bar{n}_e$ is easier to control and requires less fueling when the probe is inserted. Otherwise, discharges are reproducible and exhibit very similar behavior to the non-probed discharges which allows these probe measurements to provide insight to the internal structure of the ULq discharges.

Autopower spectra from the B_P coil signals at several outboard radial locations for the three q_a cases are shown in Figure 5.14. For the $q_a = 0.7$ case, the $\tilde{B}_P$ spectra peak near 2 kHz, and amplitudes are strongest towards the core and weaken significantly as the edge is approached. For the $q_a = 0.65$ case, the spectra have a broad peak near 17 kHz and the amplitudes are highest near $r = 24$ cm. There is also low-frequency activity which increases in amplitude from core to edge. When safety factor is decreased to $q_a = 0.55$, the fluctuation amplitudes decrease significantly and the spectra become more broadband. The spectra peak near 1 kHz and amplitudes decrease from core to edge.

Autopower spectra from the B_T coil signals at several outboard radial locations is shown in Figure 5.15. The $\tilde{B}_T$ autopower spectra are similar to the $\tilde{B}_P$ spectra but with several notable differences. For the $q_a = 0.7$ case, the spectra again peak at low frequency but appear

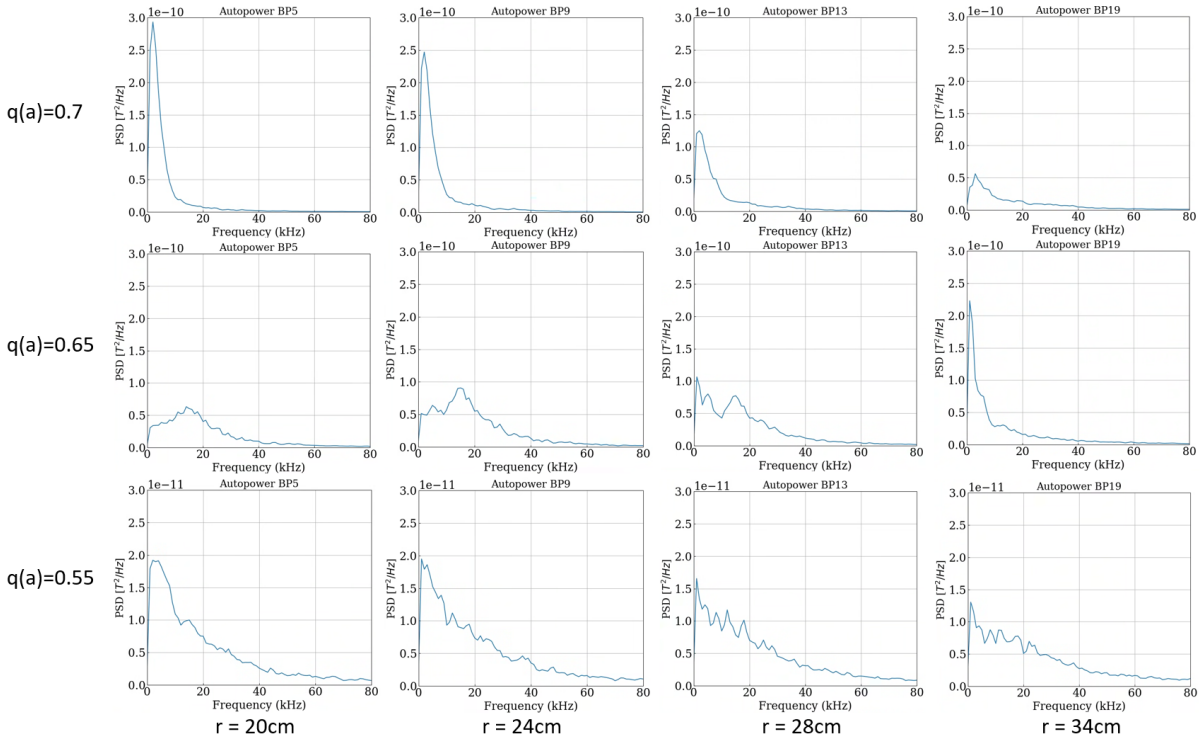

Figure 5.14: $\tilde{B}_P$ fluctuation autopower spectra from insertable probe coils at several radial locations for three different q_a cases. Note that the scale of the vertical axis is different for the $q_a = 0.55$ case.

more uniform across the radius rather than decreasing significantly towards the edge. There is also evidence of a peak near 5 kHz. The broadband 20-40 kHz fluctuations also appear to be increasing towards the edge. For the $q_a = 0.65$ case, the low-frequency peak decreases from core to edge, which is opposite to the behavior of the $\tilde{B}_P$ spectra. The broadband 17 kHz peak is also seen in the B_T fluctuations and appears localized to mid-radius; however, the amplitudes are highest at $r = 28$ cm rather than $r = 24$ cm. At $r = 34$ cm, the 17 kHz peak is still significant in the $\tilde{B}_T$ spectra while it is hardly discernible in the $\tilde{B}_P$ spectra at this location. At $q_a = 0.55$, there is a low-frequency peak near 1 kHz which was not present in the $\tilde{B}_P$ spectra, and its amplitude decreases significantly from core to edge. Broadband fluctuations at higher frequencies slightly increase from core to edge. There is also a narrow peak at 10 kHz, but this is likely due to the 10 kHz feedback power supply driving the B_T.

Autopower spectra from the B_r coil signals at several outboard radial locations is shown

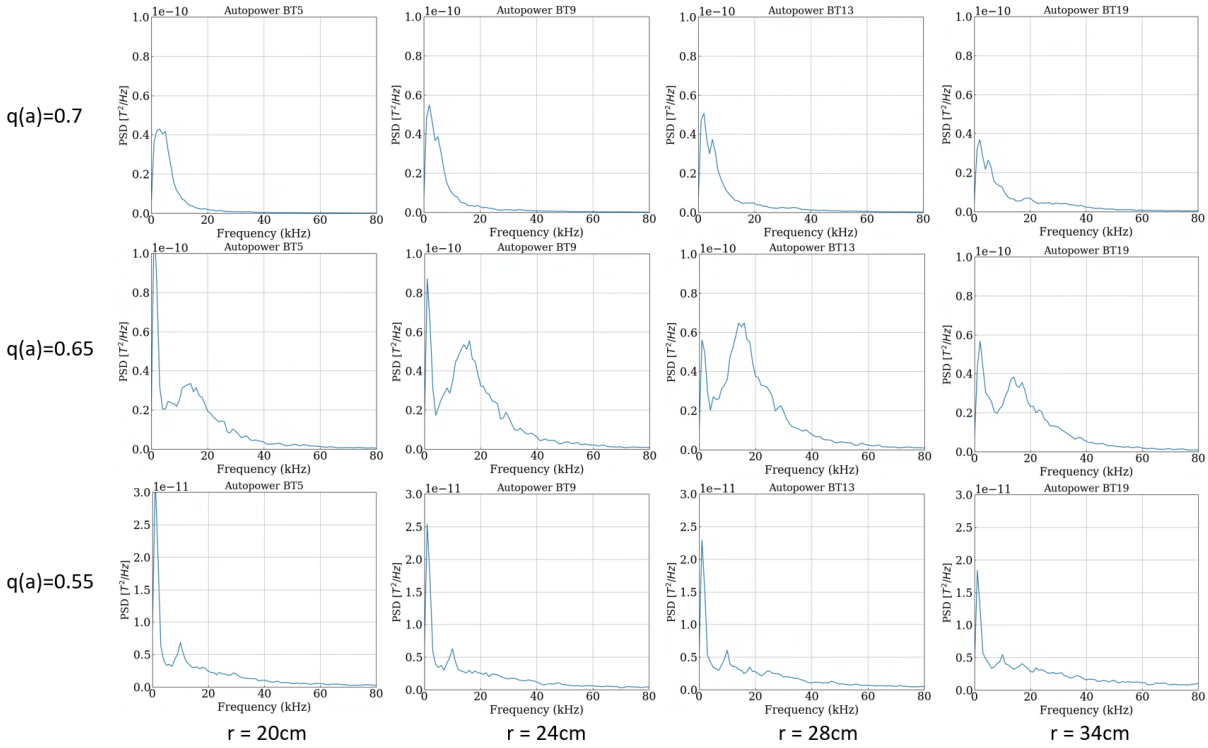

Figure 5.15: $\tilde{B}_T$ fluctuation autopower spectra from insertable probe coils at several radial locations for three different q_a cases. Note that the scale of the vertical axis is different for the $q_a = 0.55$ case.

in Figure 5.16. For the $q_a = 0.7$ case, the $\tilde{B}_r$ spectra are very similar to the $\tilde{B}_P$ spectra including a decrease in amplitudes from core to edge. The $q_a = 0.65$ case $\tilde{B}_r$ spectra also closely resemble its $\tilde{B}_P$ and $\tilde{B}_T$ spectra but with reduced low-frequency content. There is again a peak near 17 kHz with the strongest fluctuations being near $r = 24$ cm, and amplitudes decrease significantly at $r = 34$ cm as is seen in the $\tilde{B}_P$ spectra. For the $q_a = 0.55$ case, the $\tilde{B}_r$ spectra again closely resemble the $\tilde{B}_P$ spectra being broadband and decreasing in amplitude from core to edge.

The internal magnetic fluctuation spectra of the $q_a = 0.7$ case peak at $\leq$5 kHz, which is consistent with the frequency of the dominant $n = 3$ harmonic measured by the toroidal array B_P coils. The $\tilde{B}_P$ and $\tilde{B}_r$ amplitudes decrease from core to edge, which is consistent with the mode being localized near the core. However, it is not clear why the $\tilde{B}_T$ amplitudes

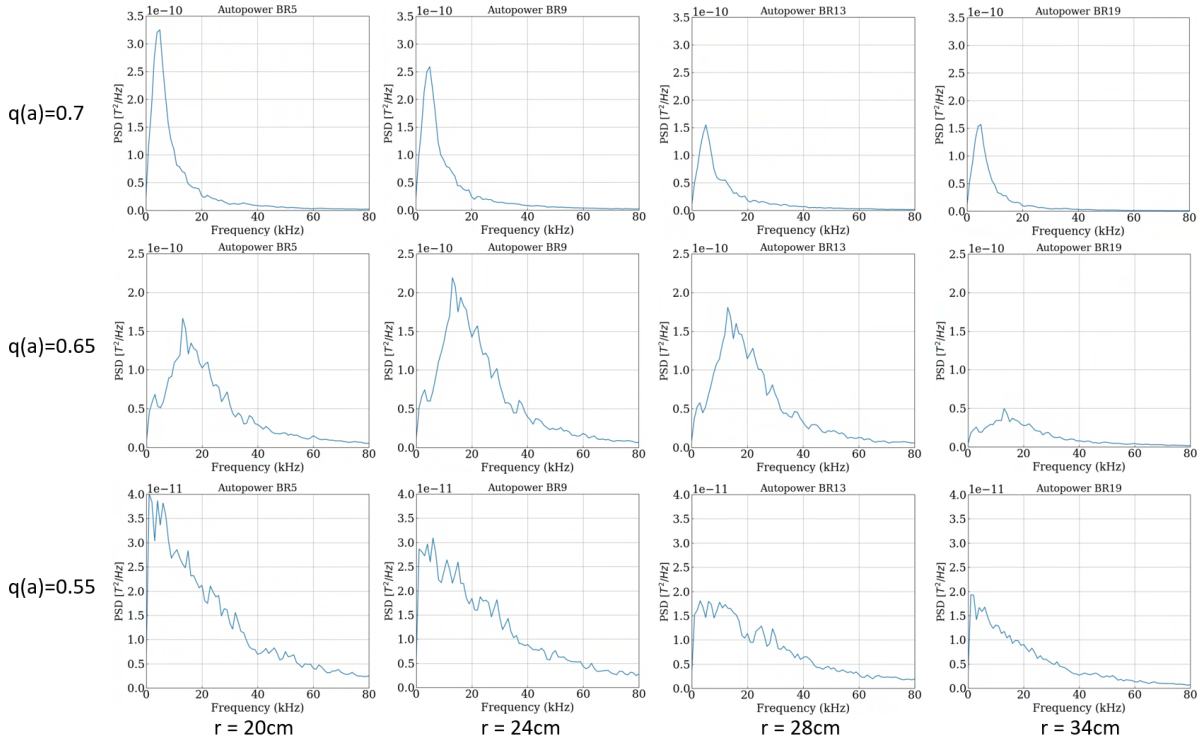

Figure 5.16: $\tilde{B}_r$ fluctuation autopower spectra from insertable probe coils at several outboard radial locations for three different q_a cases. Note that the vertical axis differs for all three q_a cases.

are more uniform across the plasma radius. The internal magnetic fluctuation spectra of the $q_a = 0.65$ show a strong broadband peak near 17 kHz, which is consistent with the increase in amplitude and frequency of the dominant $n = 3$ B_P harmonic. The location of the highest-amplitude fluctuations being near mid-radius suggests that the mode is localized to the mid-radius, which is consistent with the outward shift the the $q(r) = 2/3$ rational surface expected with the change in q_a. However, it is not clear why the 17 kHz peak at $r = 34$ cm remains high in the $\tilde{B}_T$ spectra but is significantly reduced in the $\tilde{B}_P$ and $\tilde{B}_r$ spectra. It is also unclear why there is low-frequency peak which increases from core to edge in the $\tilde{B}_P$ spectra, decreases from core to edge in the $\tilde{B}_T$ spectra, and is absent in the $\tilde{B}_r$ spectra. The internal magnetic fluctuations of the $q_a = 0.55$ case show very broadband spectra for the $\tilde{B}_P$ and $\tilde{B}_r$ fluctuations which peak at 1 kHz and decrease in amplitude from

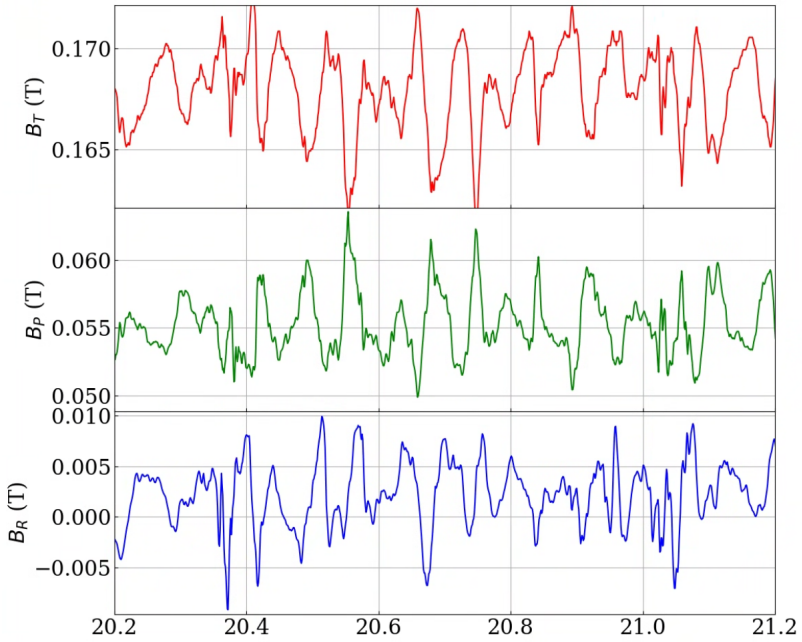

Figure 5.17: B_T, B_P, and B_r vs. time for q_a=0.65 discharge.

core to edge. The $\tilde{B}_T$ spectra are also broadband but show a much stronger 1 kHz peak which decreases from core to edge. The loss of the high-frequency peak is consistent with the loss of the $q(r) = 2/3$ rational surface and $n = 3$ B_P harmonic. The magnetic fluctuations appear to be sourced by a core-localized mode or multiple modes. Analysis of the toroidal array suggests that the $n = 5$ B_P harmonic is largest in this case, but there is no clear peak in the spectra. These observations would be consistent with the emergence of a $q(r) = 2/5$ rational surface and $n = 5$ mode near the core if the mode frequency were fluctuating rapidly to produce the very broadband spectrum.

Time traces for the B_T, B_P, and B_r components at a single radial location for the $q_a = 0.65$ case is shown in Figure 5.17. These nearly-periodic fluctuations are typical for the $q_a = 0.65$ case. Notice that the B_T and B_P traces are 180° out of phase and the B_r trace is 90° out of phase with the other two components. Plots of $B_T - B_P$ crossphase for the three q_a cases at several outboard radial locations is shown in Figure 5.18. Notice that the phase difference between B_P and B_T fluctuations is always ∼180° for frequencies of 3-80 kHz. This

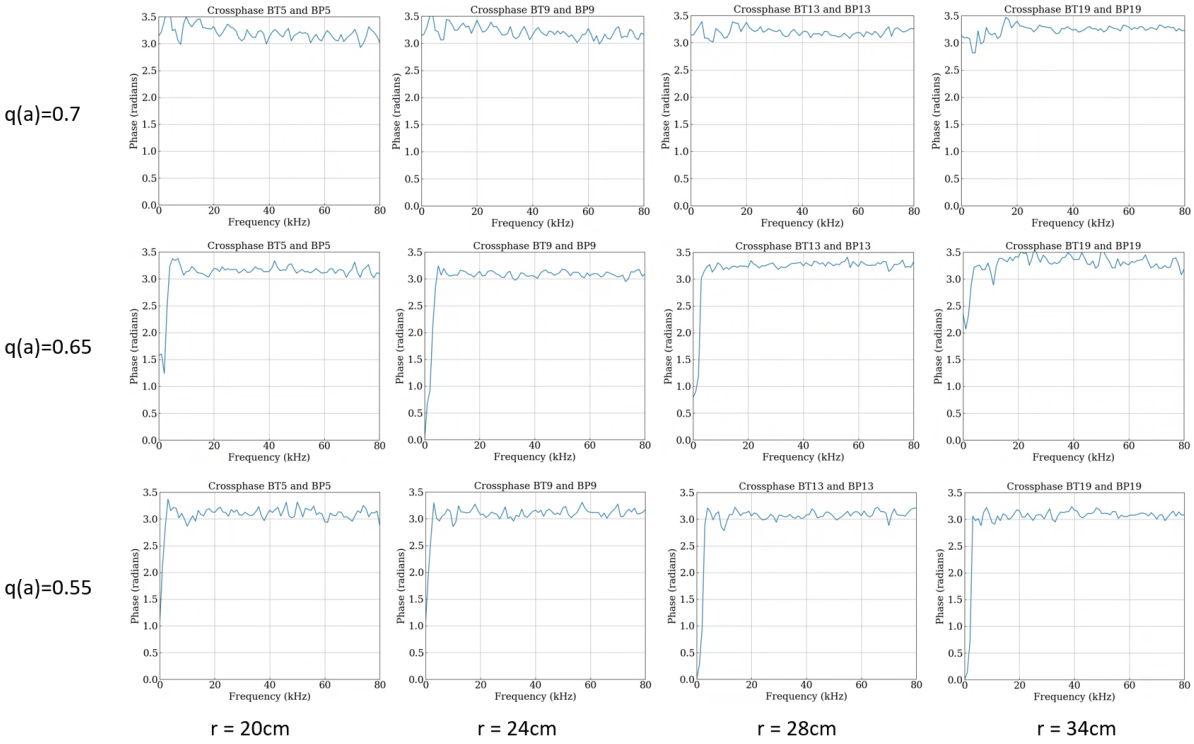

Figure 5.18: $B_T - B_P$ crossphase spectra from insertable probe coils at several outboard radial locations for three different q_a cases.

is observed for all three q_a cases and all radial locations sampled.

A plot of coherence between B_P coil signals with increasing radial separation for the three q_a cases is shown in Figure 5.19. For the $q_a = 0.7$ case, coherence is strongest at very low frequencies, and for frequencies above 10 kHz, coherence decays to the noise level within 12 cm of radial separation. For the $q_a = 0.65$ case, there is strong broadband coherence around 17 kHz, and the coherence is reduced nearly to the noise level at a separation of 12 cm. For the $q_a = 0.55$ case, coherence is broadband at low frequencies and decays to the noise level by 8 cm of radial separation. These coherence lengths are small compared to the minor radius which suggest that the magnetic fluctuations are sourced by radially localized perturbations that lose coherence as they propagate away from the source.

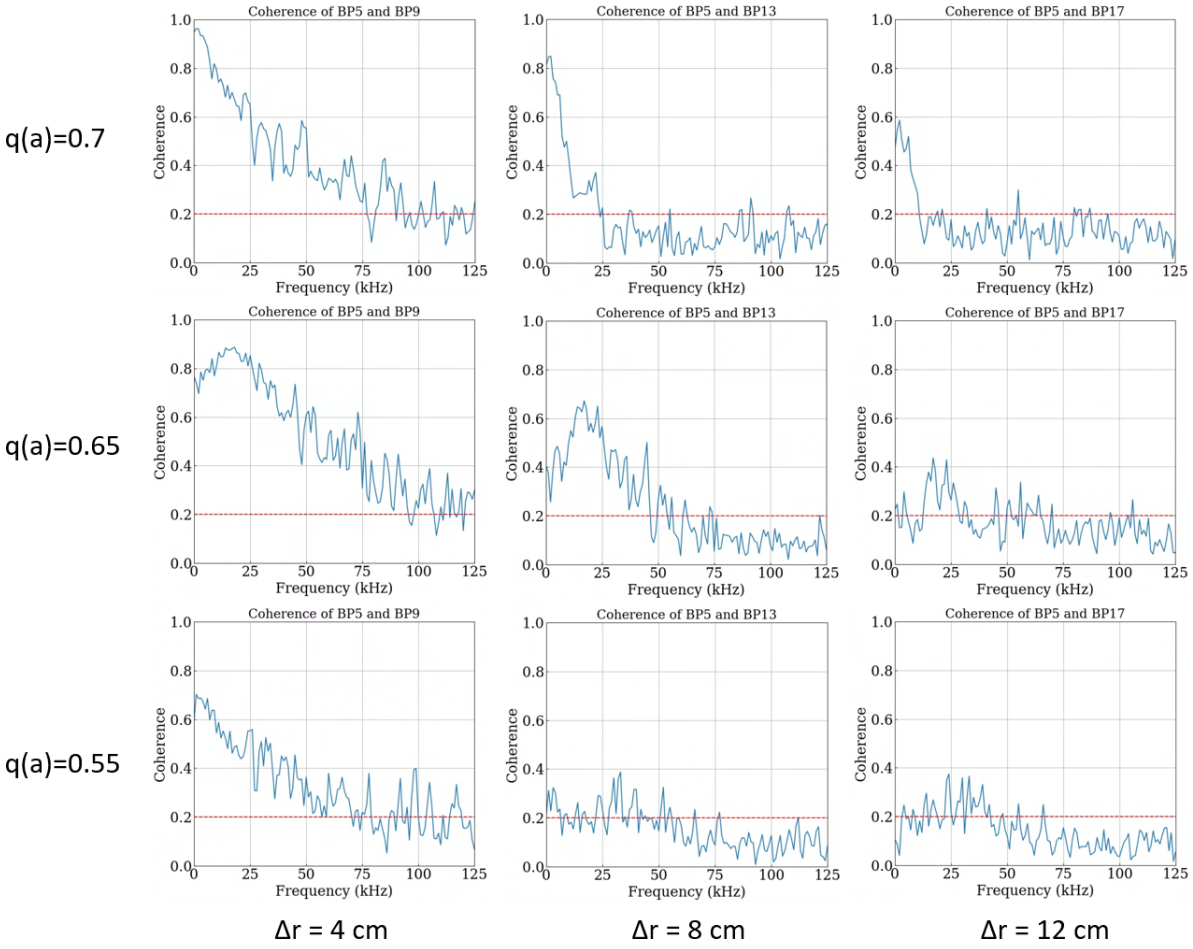

Figure 5.19: Coherence between B_P coil signals with increasing radial separation for the three q_a cases. Statistical noise level indicated with dashed horizontal lines.

5.4.3 Line-integrated Density Fluctuations

$\bar{n}_e$ measurements do not show the same autopower spectra or radial variation in amplitudes as the internal magnetics, possibly because they are line-integrated measurements while the magnetic fluctuations are local measurements. A plot of $\bar{n}_e$ fluctuation autopower spectra from FIR interferometer chords across the inboard radius of the three different q_a cases is shown in Figure 5.20, and the outboard chord autopower spectra are shown in Figure 5.21. Note that these spectra are from the discharges with the magnetics probe inserted to allow direct comparison to the magnetic fluctuations.

For the $q_a = 0.7$ case, the $\bar{n}_e$ fluctuation spectra have peaks at 1 kHz and 4 kHz. The 1 kHz

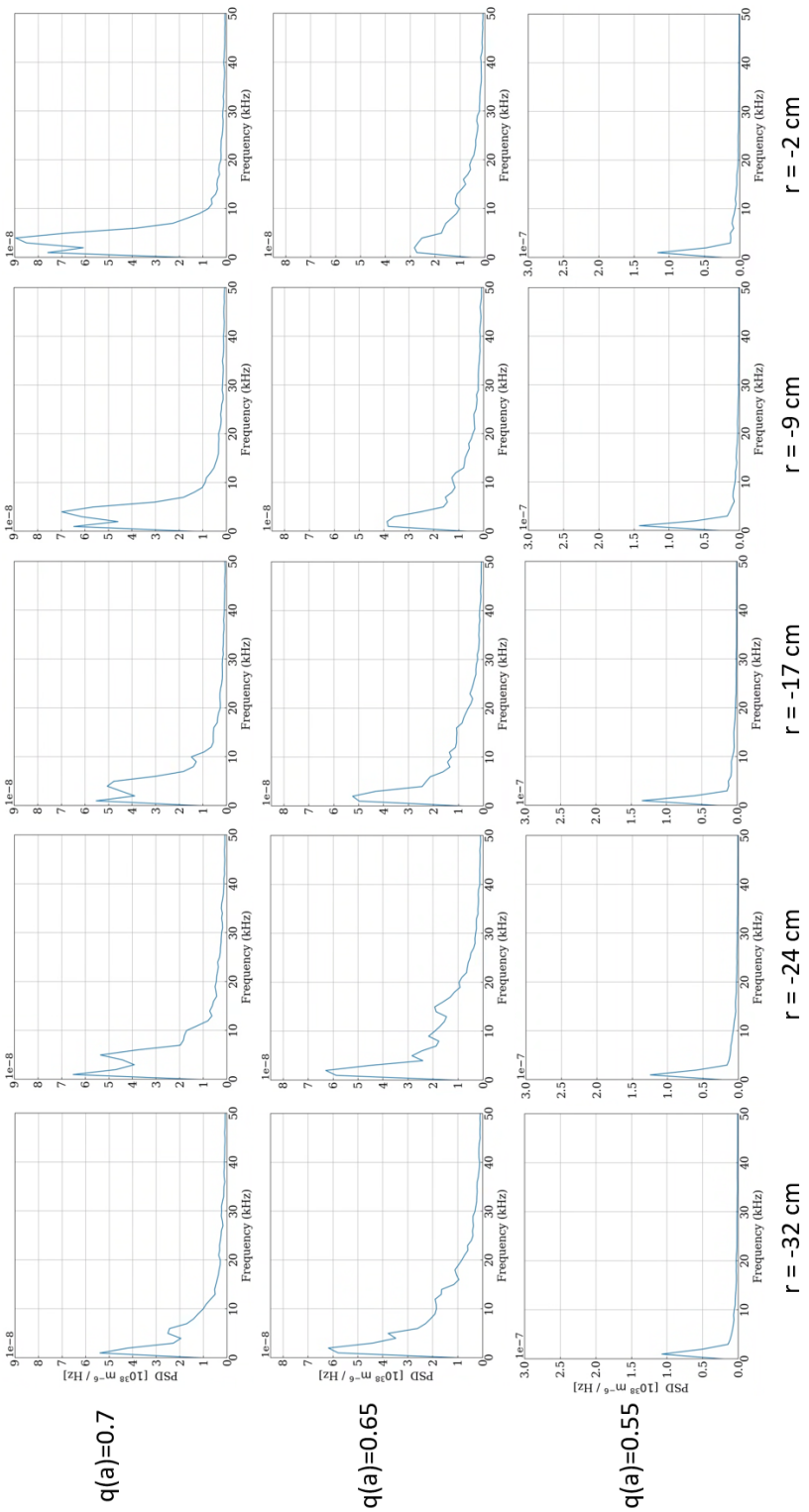

Figure 5.20: $\bar{n}_e$ fluctuation autopower spectra from inboard FIR interferometer chords for three different q_a cases.

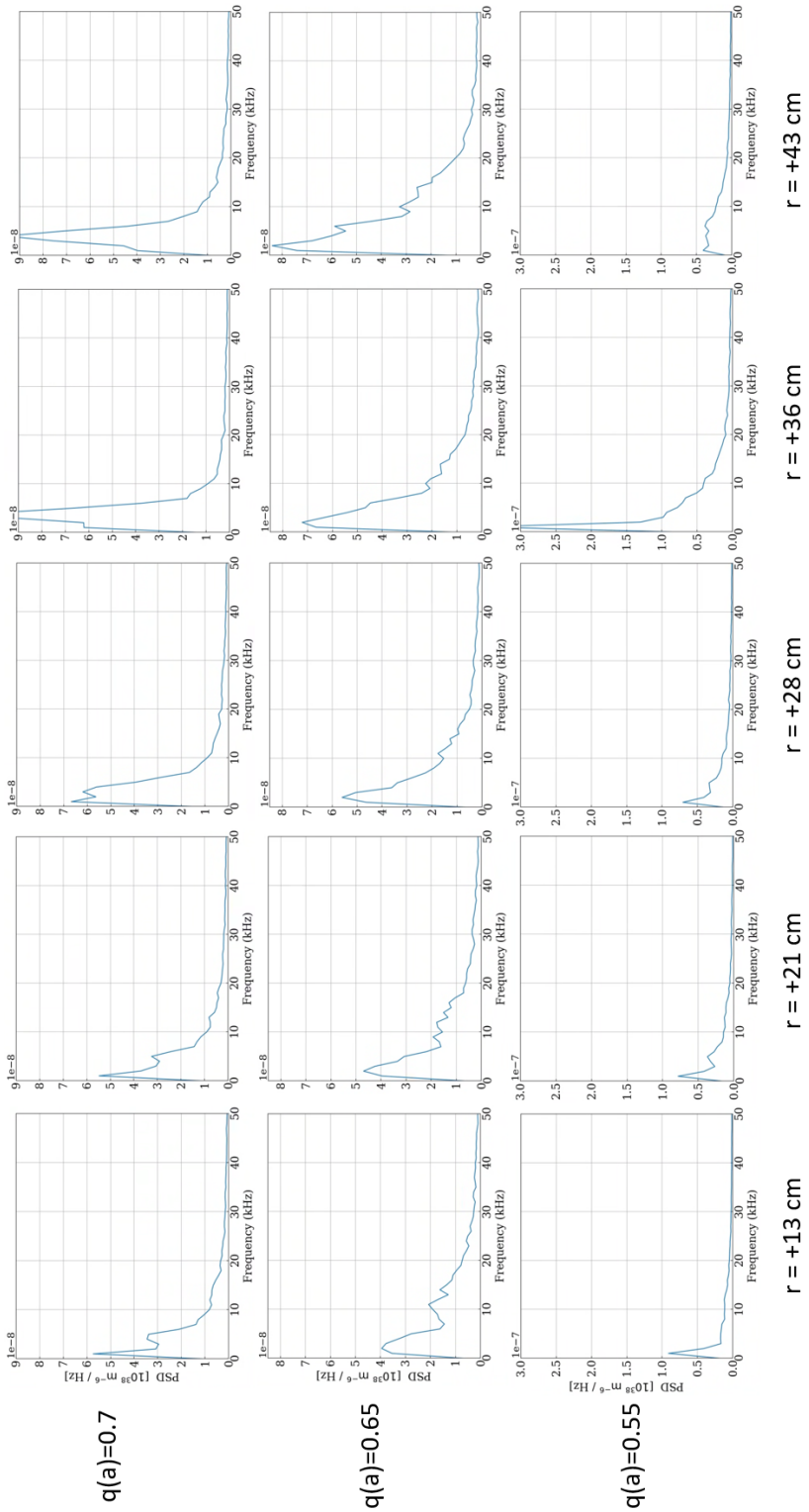

Figure 5.21: $\bar{n}_e$ fluctuation autopower spectra from outboard FIR interferometer chords for three different q_a cases.

peak is nearly uniform across all chords, but the 4 kHz peak amplitude varies significantly with radial location. On the inboard side, amplitudes increase from edge to core, but on the outboard side, amplitudes increase from core to edge. The 4 kHz peak is consistent with the frequency of $n = 3$ harmonic observed in edge B_P fluctuations, but the radial profile of the $\bar{n}_e$ fluctuation amplitudes is puzzling. This may be due to the observation of an outboard-shifted helical structure, but explaining this feature will require future work.

For the $q_a = 0.65$ case, $\bar{n}_e$ fluctuation spectra peak at 2 kHz and increase from core to edge on both inboard and outboard sides. Broadband fluctuation amplitudes at 10-20 kHz are higher than in the $q_a = 0.7$ case. The $\bar{n}_e$ fluctuation amplitudes increasing towards the edge where the $\bar{n}_e$ gradients are strongest is consistent with interchange modes dominating the $\bar{n}_e$ fluctuations. It would also be consistent with a rotating helical structure perturbing the $\bar{n}_e$ gradient.

For the $q_a = 0.55$ case, the $\bar{n}_e$ fluctuation spectra on the inboard side peak at 1 kHz and have relatively low broadband fluctuation amplitudes, and the spectra are nearly uniform across the inboard radius. On the outboard side, the spectra also peak at 1 kHz but with more broadband content as the outboard edge is approached. At r = 36 cm, there is a large increase in fluctuation amplitudes at 1 kHz and increase in broadband fluctuations up to 10 kHz. The magnetic fluctuations are broadband and increase in amplitude towards the core, which suggests that the highest-amplitude $\bar{n}_e$ fluctuations may not be directly related to the magnetic fluctuations. The large increase in amplitudes in the region of the outboard density gradient is suggestive of ballooning modes dominating the $\bar{n}_e$ fluctuations.

The radial coherence length scale of the $\bar{n}_e$ fluctuations is estimated by computing the coherence between interferometer chords with increasing radial separation. Plots of the coherence spectra between interferometer chords with different radial separation for the $q_a = 0.65$ case is shown in Figure 5.22. $\bar{n}_e$ fluctuations at frequencies $<$20 kHz are coherent at 4

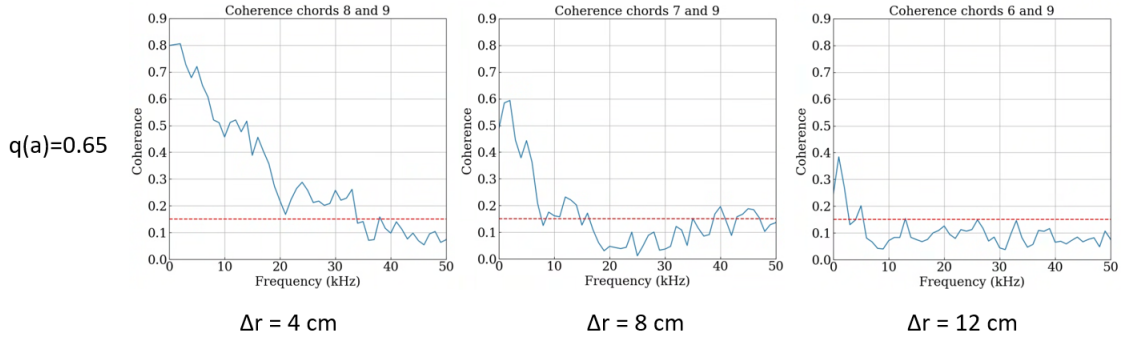

Figure 5.22: Coherence between $\bar{n}_e$ signals with increasing radial separation for the $q_a = 0.65$ case. Statistical noise level indicated with horizontal dashed lines

cm separation. Fluctuations at frequencies <8 kHz remain coherent at 8 cm separation, and only frequencies <2 kHz are coherent at 12 cm separation. Like the magnetic fluctuations, the broadband $\bar{n}_e$ fluctuations have short radial coherence lengths compare to plasma minor radius.

5.4.4 Density and Magnetic Fluctuation Correlation

Notably, no significant coherence was observed between any interferometer chords and the coil signals from the insertable probe array which was separated from the interferometer chords toroidally by about 75°. However, coherence analysis between interferometer signals and toroidal array B_P coils at the closest toroidal angle to the interferometer chords does show significant coherence. Plots of coherence spectra between the edge B_P coil and inboard interferometer chords is shown in Figure 5.23, and coherence spectra for outboard chords is shown in Figure 5.24. For the $q_a = 0.7$ case, coherence between $\tilde{B}_P$ and $\bar{n}_e$ fluctuations peaks near 4-5 kHz at all radial locations, and the coherence is marginally higher at r = -2 and -9 cm. For the $q_a = 0.65$ case, the coherence of fluctuations in the 10-25 kHz band increases significantly at r = -24, -17, +13, and +21 cm. There is also significant coherence at frequencies <5 kHz which is highest near the inboard edge. The $q_a = 0.55$ case does not show significant changes in coherence spectra across the plasma radius. There is a small

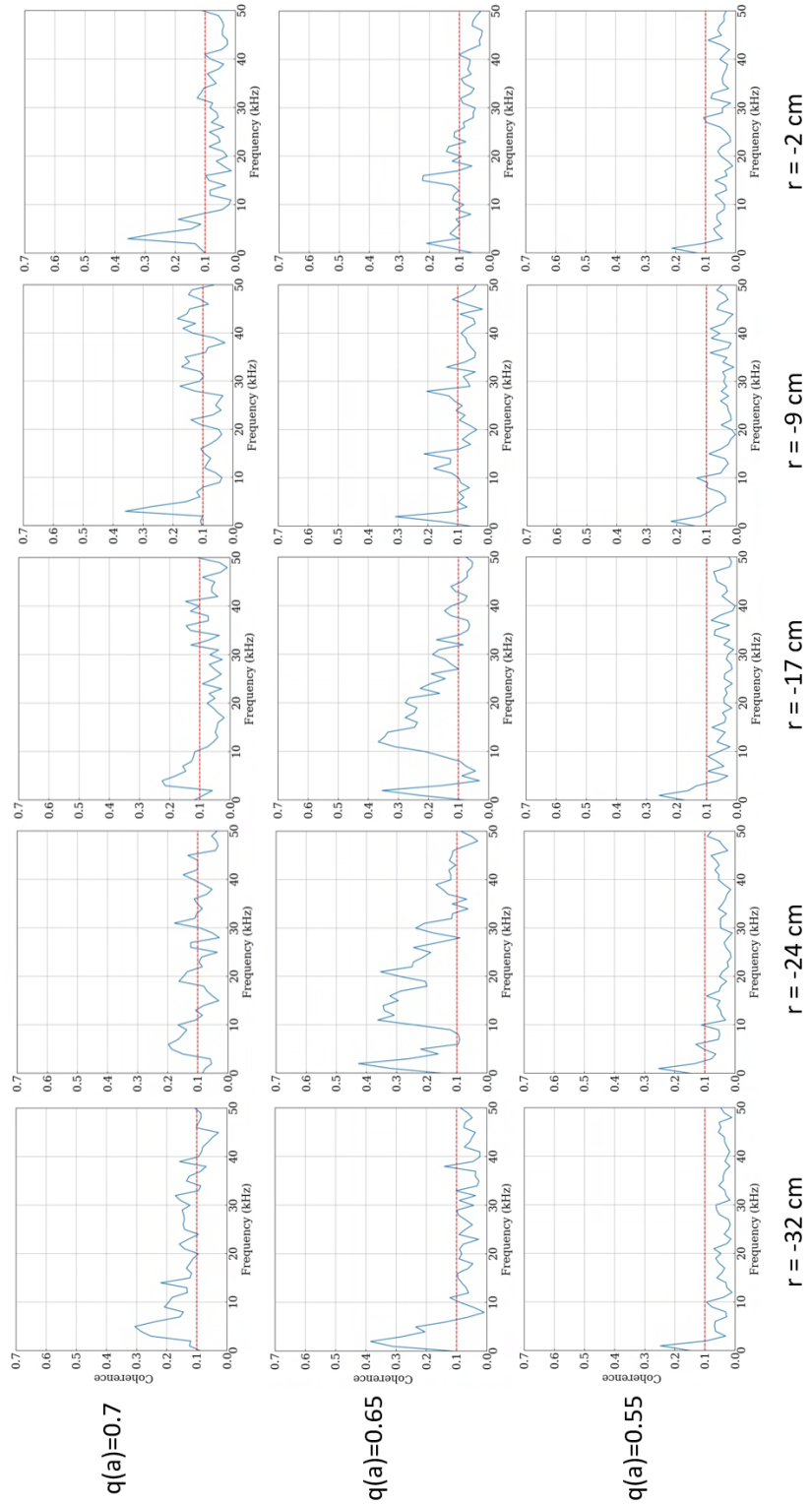

Figure 5.23: Coherence between toroidal array B_P coil signal and $\bar{n}_e$ signals from inboard FIR chords at several radial locations for three different q_a cases. The coil and FIR chords have toroidal separation of 1° to 6°.

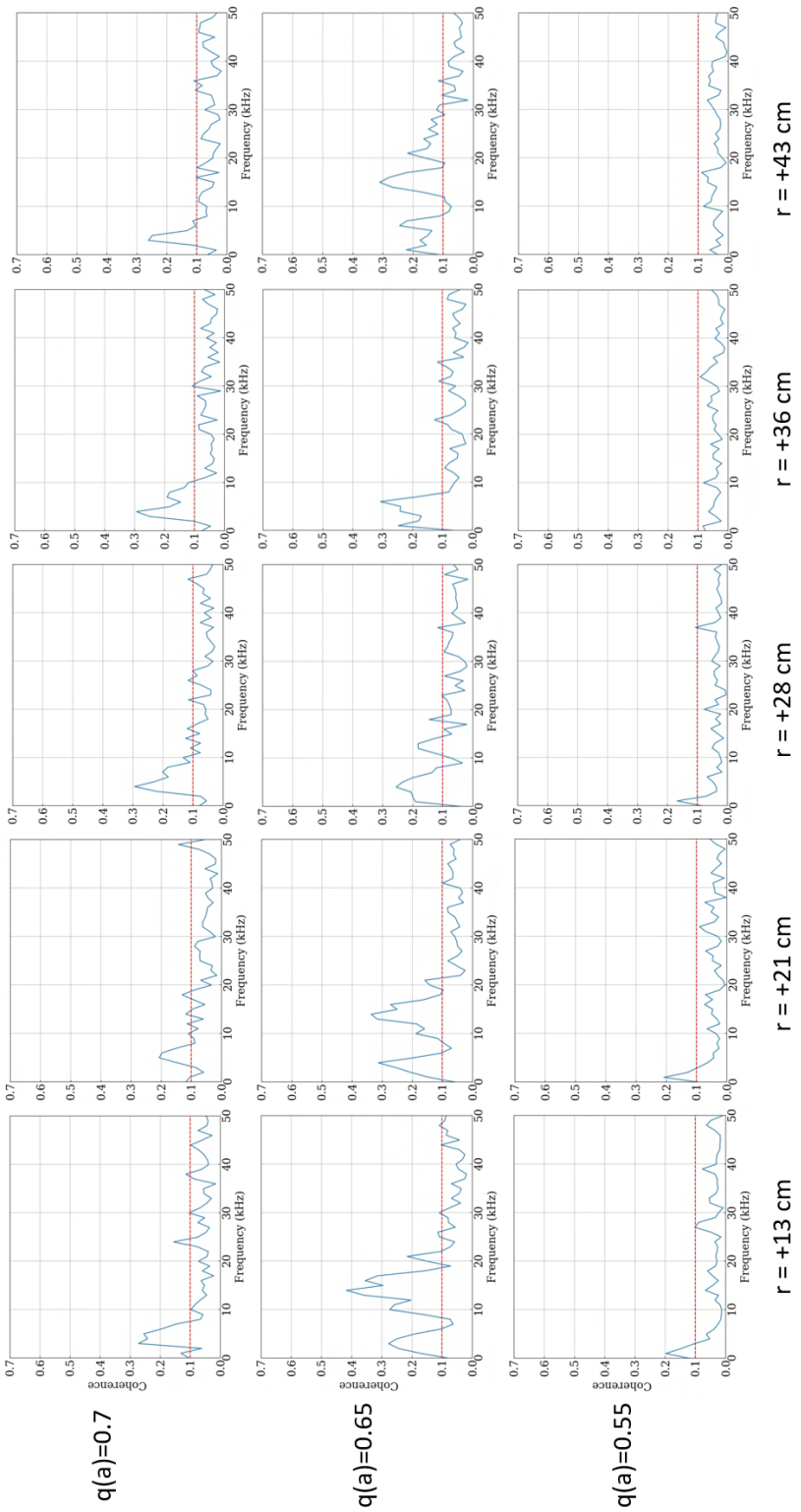

Figure 5.24: Coherence between toroidal array B_P coil signal and $\bar{n}_e$ signals from inboard FIR chords at several radial locations for three different q_a cases. The coil and FIR chords have toroidal separation of 1° to 6°.

peak at 1 kHz, but this peak lies just above the noise level and may not be significant. The lack of coherence may be due to the large distance between the edge coil and the apparent core-localized mode(s) sourcing the $\tilde{B}_P$ fluctuations, or it may indicate that the $\tilde{B}_P$ and $\bar{n}_e$ fluctuations are truly incoherent. This analysis shows that there is significant coherence between $\bar{n}_e$ and $\tilde{B}_P$ at the frequencies of the dominant B_P toroidal harmonics, which would be expected for a large-scale helical structures. However, much of the $\bar{n}_e$ fluctuation power is incoherent with $\tilde{B}_P$ measured at the edge.

5.4.5 Plasma Potential and Radial Electric Field Fluctuations

Measurements of broadband magnetic and $\bar{n}_e$ fluctuations have been presented, but non-collisional ion heating by these fluctuations must be facilitated by an associated fluctuating electric field. This motivated the use of the insertable capacitive probe for measurements of the plasma potential Φ_P and radial electric field E_r. The capacitive probe is mounted at a poloidal angle of 90° and toroidal angle of 275°.

$\tilde{\Phi}_P$ autopower spectra measured at 7.5 cm within the plasma edge for the three q_a cases is shown in Figure 5.25. Notice that the spectra for all three q_a cases resemble their magnetic

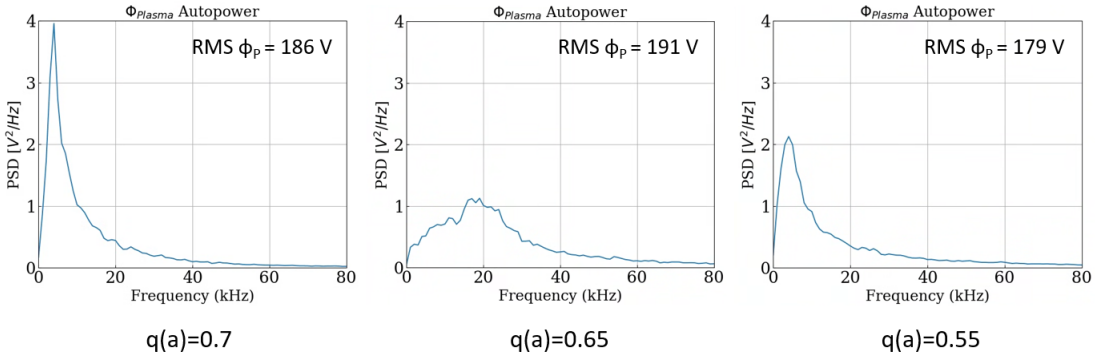

Figure 5.25: $\tilde{\Phi}_P$ autopower spectra and RMS values measured at 7.5 cm within the plasma edge for the three q_a cases at $\bar{n}_e \approx 1.5 \times 10^{18}\ m^{-3}$.

fluctuation spectra with the $q_a = 0.7$ spectrum peaking at 5 kHz, the $q_a = 0.65$ spectrum

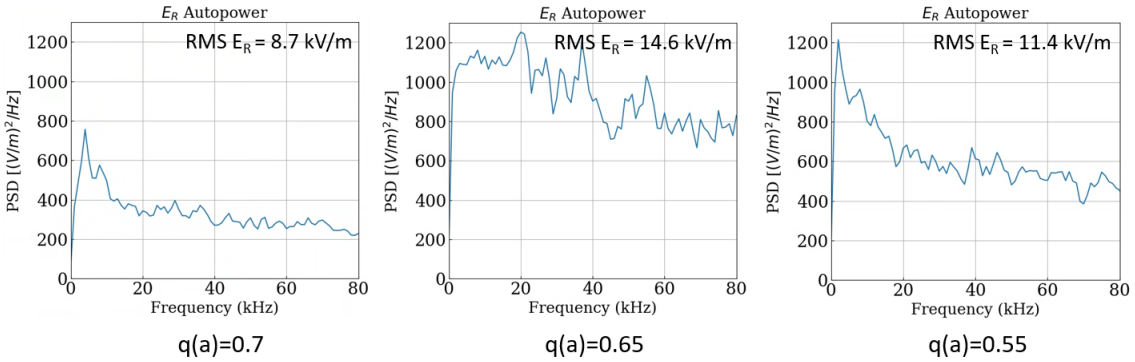

Figure 5.26: $\tilde{E}_r$ autopower spectra and RMS values at 7.5 cm within the plasma edge for the three q_a cases.

peaking at 18 kHz, and the $q_a = 0.55$ spectrum peaking at 4 kHz. The RMS $\tilde{\Phi}_P$ values are similar for the three cases.

The E_r fluctuations were measured by taking the difference between simultaneously measured Φ_P signals at two locations separated radially by 7 mm. Plots of $\tilde{E}_r$ autopower spectra for the three q_a cases are shown in Figure 5.26. Notice that the $\tilde{E}_r$ spectra are very broadband and RMS values are high, up to 14.6 kV/m. Although the RMS $\tilde{\Phi}_P$ values for the three cases were nearly equal, RMS $\tilde{E}_r$ amplitudes increase significantly from $q_a = 0.7$ to $q_a = 0.65$ and then decrease at $q_a = 0.55$.

The broadband $\tilde{E}_r$ fluctuations are observed to have very short coherence lengths. Using the two inner and two outer capacitive sensors, two independent $\tilde{E}_r$ measurements are made with radial separation of 1.4 cm. Plots of the coherence spectra between these two radially-separated $\tilde{E}_r$ measurements for the three q_a cases are shown in Figure 5.27. Notice that each case shows marginal to significant coherence at frequencies where the $\tilde{\Phi}_P$ power spectra peak but no coherence across much of the spectrum where significant $\tilde{E}_r$ amplitudes are observed.

Significant coherence is observed between $\tilde{\Phi}_P$ and magnetic fluctuations measured at the edge. Plots of coherence between the $\tilde{\Phi}_P$ and $\tilde{B}_P$ for the three q_a cases are shown in Figure 5.28. The $q_a = 0.7$ and 0.65 cases exhibit significant coherence at their peak frequencies of

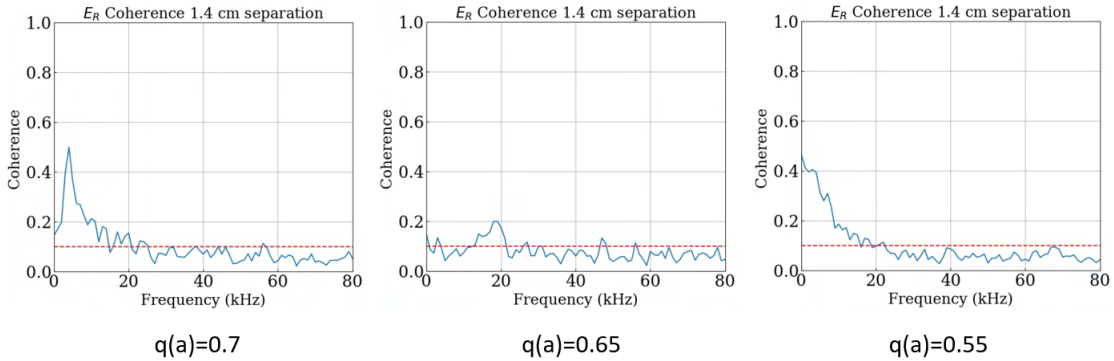

Figure 5.27: Coherence spectra between two independent $\tilde{E}_r$ measurements separated by 1.4 cm for the three q_a cases.

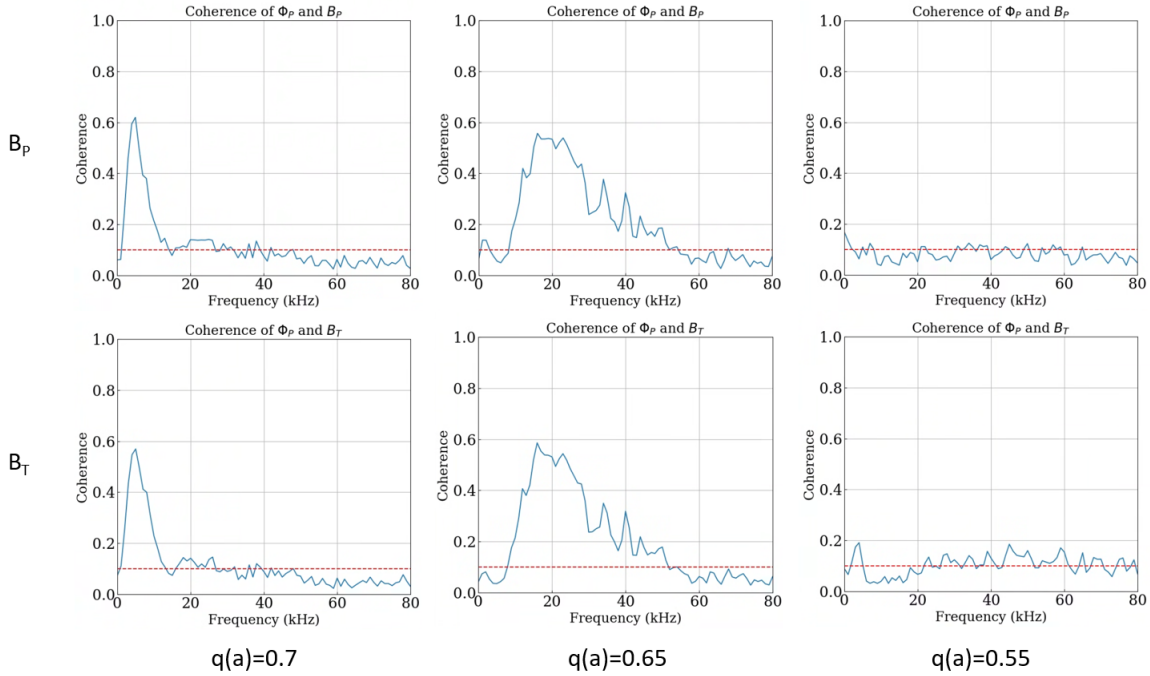

Figure 5.28: Coherence spectra between $\tilde{\Phi}_P$ and $\tilde{B}_P$ for the three q_a cases. $\tilde{\Phi}_P$ is measured by the capacitive sensor at 7.5 cm within the plasmas edge, and $\tilde{B}_P$ is measured by a dense array coil. The measurements have a toroidal separation of $\sim$29° and poloidal separation of $\sim$122°.

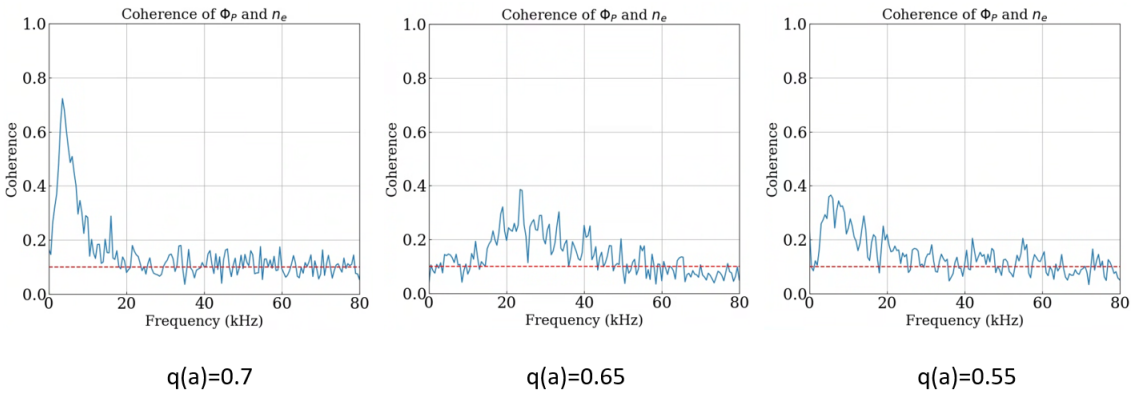

Figure 5.29: Coherence spectra between $\tilde{\Phi}_P$ and $\bar{n}_e$ fluctuations for the three q_a cases. $\tilde{\Phi}_P$ is measured by the capacitive sensor at 7.5 cm within the plasmas edge, and $\bar{n}_e$ is measured by a tangential interferometer chord (chord #11, "P43") intersecting the midplane at $r = 43$ cm.

$\sim$5 kHz and $\sim$20 kHz respectively, but the $q_a = 0.55$ case shows no significant coherence. The lack of coherence for the $q_a = 0.55$ case may be due to the distance from the wall-mounted coils to the core-localized magnetic fluctuations.

Coherence is also observed between the $\tilde{\Phi}_P$ and $\bar{n}_e$ fluctuations at the same frequencies. Plots of coherence between the $\tilde{\Phi}_P$ and $\bar{n}_e$ fluctuations measured near the edge for the three q_a cases is shown in Figure 5.29. Note that the $\bar{n}_e$ measurement is line-averaged and separated poloidally from the $\tilde{\Phi}_P$ measurement by about 90°. Still, significant coherence is observed at the same peak frequencies.

The $\tilde{\Phi}_P$ fluctuation amplitudes and spectra also show a strong dependence on plasma density. Plots of $\tilde{\Phi}_P$ fluctuation spectra and RMS amplitudes for different values of $\bar{n}_e$ in the $q_a = 0.65$ case are shown in Figure 5.30. Notice that, as $\bar{n}_e$ decreases, the fluctuation spectra shift to higher frequency and become significantly more broadband while the RMS amplitudes also increase. A $\bar{n}_e$ dependence is also seen in the $\tilde{E}_r$ autopower spectra, RMS amplitudes, and coherence spectra. Plots of $\tilde{E}_r$ autopower spectra, RMS amplitudes, and coherence spectra for $\tilde{E}_r$ measurements with radial separation of 1.4 cm are shown for different values of $\bar{n}_e$ in Figure 5.31. Notice that the $\tilde{E}_r$ RMS amplitudes increase and autopower

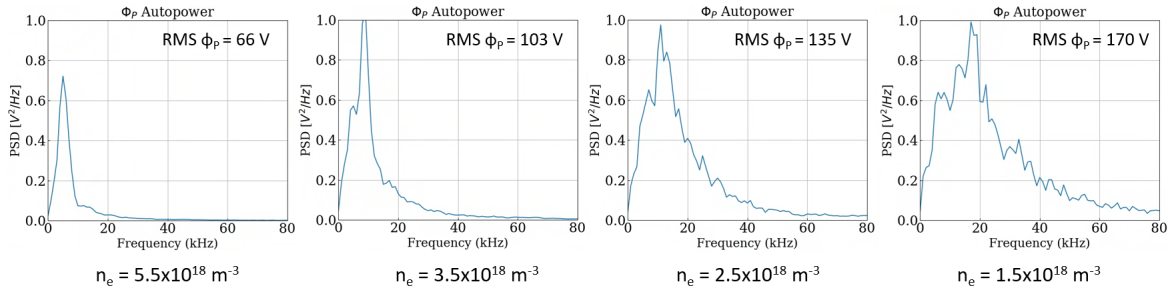

Figure 5.30: $\tilde{\Phi}_P$ autopower spectra and RMS values for four different core $\bar{n}_e$ values at $q_a = 0.65$.

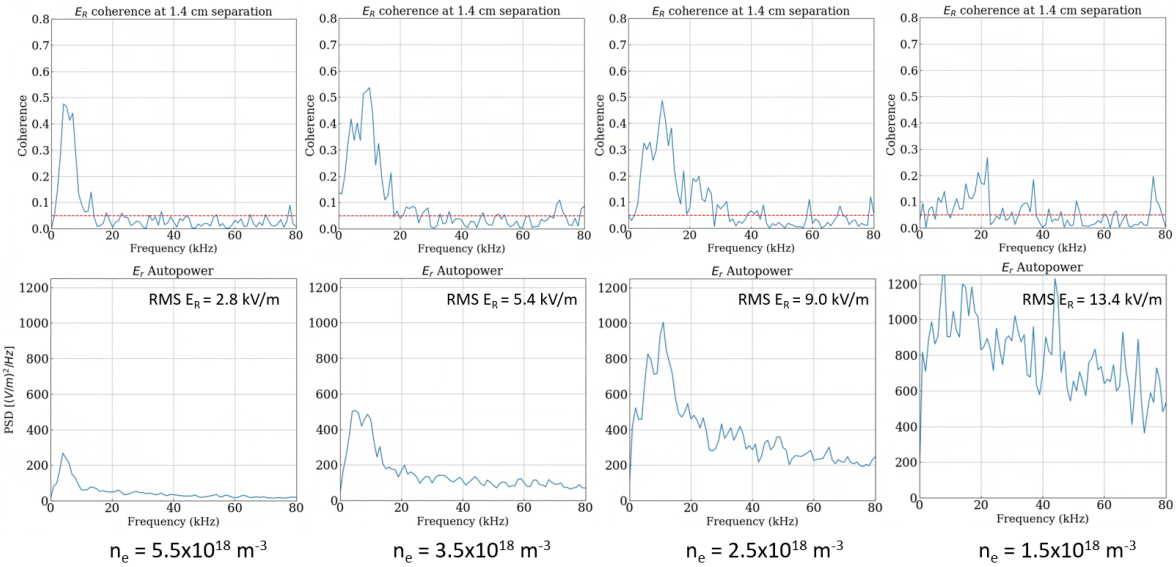

Figure 5.31: For four different values of core $\bar{n}_e$ at $q_a = 0.65$, (Top) $\tilde{E}_r$ coherence spectra for measurements separated radially by 1.4 cm. (Bottom) $\tilde{E}_r$ autopower spectra and RMS amplitudes.

spectra shift to higher frequency and broaden significantly as $\bar{n}_e$ decreases. The $\tilde{E}_r$ coherence spectra broaden, shift to higher frequency, and decrease in amplitude as $\bar{n}_e$ decreases.

These measurements demonstrate that high-amplitude $\tilde{\Phi}_P$ and $\tilde{E}_r$ are driven in ULq plasmas with a strong dependence on q_a and $\bar{n}_e$. The significant coherence between $\tilde{\Phi}_P$, $\tilde{B}_P$, and $\bar{n}_e$ fluctuations at the rotation frequencies of the dominant B_P toroidal harmonics suggests that the fluctuations are associated with the rotation of large-scale resonant modes. The observation of high-amplitude, short coherence length $\tilde{E}_r$ fluctuations suggests that stochastic heating may be significant in these plasmas, and the trends of $\tilde{E}_r$ amplitudes

increasing and coherence decreasing as $\bar{n}_e$ decreases is consistent with the trend in $\bar{T}_z$.

5.5 Summary and Discussion

The scan of edge safety factor over the range of $0.4 \leq q_a \leq 0.9$ shows that ULq discharge behavior is strongly dependent on the value of q_a. B-IV $\bar{T}_z$ and R_P vary significantly with q_a, and $\bar{T}_z$ is highest at $q_a \approx$ 0.6-0.65. This range of q_a is also where the $n = 3, 5$ B_P harmonics have peak amplitudes and peak rotation frequencies. The trend in $\bar{T}_z$ is similar to the trend in $\tilde{B}_T$ and $\tilde{B}_P$ fluctuation amplitudes of 10-50 kHz, and the highest amplitudes at frequencies of 10-15 kHz are consistent with the rotation frequencies of the dominant B_P harmonics. A similar trend is observed between high-frequency $\bar{n}_e$ fluctuation amplitudes and $\bar{T}_z$, but not for the highest-amplitude $\bar{n}_e$ fluctuations which are $\leq$5 kHz. ULq plasmas have core-peaked $\bar{n}_e(r)$ profiles, and the $\bar{T}_z(r)$ profile at $q_a = 0.65$ exhibits a similar core-peaked structure.

The $\bar{n}_e$ scan at $q_a = 0.65$ shows that there is a greater than linear increase in $\bar{T}_z$ as $\bar{n}_e$ decreases while Ohmic input power increases roughly linearly. The trend in $\bar{T}_z$ is similar to the trend of increasing frequency of the dominant $n = 3$ B_P harmonic and the increase in broadband magnetic fluctuations at 10-50 kHz. This suggests that the rotation of the resonant modes, or the conditions responsible for their increase in rotation, are involved in the impurity heating. The low-frequency, high-amplitude $\bar{n}_e$ fluctuations decrease as $\bar{n}_e$ decreases, which suggests that the dominant $\bar{n}_e$ fluctuations are not directly involved in the impurity heating.

The scan of B_T and I_P at $q_a = 0.65$ and constant $\bar{n}_e$ shows that $\bar{T}_z$ increases with equilibrium magnetic field and Ohmic input power while R_P remains nearly constant. The increase in magnetic field causes a small increase in B_P toroidal harmonic amplitudes, but the normalized amplitudes decrease slightly. B_P toroidal harmonic frequencies remained nearly constant. High-frequency magnetic fluctuation amplitudes increase with increasing B_T and

I_P, and their normalized amplitudes remained nearly constant. $\bar{n}_e$ fluctuation amplitudes showed no significant change. These observations suggest that the increasing high-frequency magnetic fluctuation amplitudes, and possibly an increase in impurity energy confinement time, are associated with the increase in the $\bar{T}_z$ in this scan.

Magnetic, $\bar{n}_e$, and Φ_P fluctuations are analyzed in detail for three edge safety factor cases of $q_a = 0.7$, 0.65, and 0.55 which are selected due to their significant change fluctuations and $\bar{T}_z$ with small changes in plasma current. As q_a is decreased from 0.7 to 0.65, there is a $\sim$10% increase in R_P and over a factor of 2$\times$ increase in $\bar{T}_z$. When q_a is decreased to 0.55, there is a $>$50% decrease in R_P and a $\sim$50% decrease in $\bar{T}_z$.

The radial variation of the $\tilde{B}_P$ and $\tilde{B}_r$ fluctuations of the $q_a = 0.7$ case suggests that there is a mode localized near the core which sources fluctuations around 4 kHz. This is consistent with the observations of a low-frequency, high-amplitude $n = 3$ B_P harmonic and the expectation of a $q(r) = 2/3$ rational surface located near the core. The radial variation of the $\tilde{B}_P$, $\tilde{B}_T$, and $\tilde{B}_r$ fluctuations of the $q_a = 0.65$ case suggests that there is a large mode localized near mid-radius sourcing broadband magnetic fluctuations around 17 kHz, and this frequency is consistent with the observed dominant $n = 3$ B_P harmonic frequency of 15-20 kHz. This suggests that the lowering of q_a causes the $q(r) = 2/3$ rational surface to shift towards mid-radius, the mode amplitude to increase, and mode rotation speed to increase. The radial variation of $\tilde{B}_P$, $\tilde{B}_T$, and $\tilde{B}_r$ fluctuations of the $q_a = 0.55$ case suggests that there is a mode or multiple modes localized near the core. Compared to the other q_a cases, the fluctuation amplitudes are reduced by a factor of 5-10$\times$, and the $\tilde{B}_P$ and $\tilde{B}_r$ fluctuation spectra are significantly more broadband than the higher q_a cases. The observation of the $n = 5$ B_P harmonic being dominant is consistent with the loss of the $q(r) = 2/3$ rational surface and the emergence of a $q(r) = 2/5$ surface near the core as q_a is lowered to 0.55. The magnetic fluctuations are observed to have radial coherence lengths which are short

compared to the minor radius which suggests that the fluctuations are sourced by radially-localized perturbations.

Frequency analysis of the $\bar{n}_e$ fluctuations show spectra and radial variation different from the magnetic fluctuations. $\bar{n}_e$ fluctuation amplitudes are always highest at frequencies $<$5 kHz even when the highest-amplitude magnetic fluctuations are $>$10 kHz. This difference between magnetic and $\bar{n}_e$ fluctuation spectra suggests that the modes responsible for the dominant $\bar{n}_e$ fluctuations may not be the same modes which dominate the magnetic fluctuation spectra. Low-frequency $\bar{n}_e$ fluctuation amplitudes tend to increase in the regions of strong $\bar{n}_e$ gradient near the edge, but radial profiles of the $\bar{n}_e$ fluctuation amplitudes vary significantly with q_a. There is not a clear explanation for these observations, but they could be due to interchange modes, ballooning modes, or helical density perturbations. Weak but significant coherence is observed between $\bar{n}_e$ fluctuations and $\tilde{B}_P$ measured at the edge at frequencies where the $\tilde{B}_P$ autopower spectra peak. This suggests that the rotation of the resonant modes contributes to the $\bar{n}_e$ fluctuations, but most of the $\bar{n}_e$ fluctuations are incoherent with edge magnetics. The radial coherence lengths of the $\bar{n}_e$ fluctuations are also small compared to the minor radius.

Capacitive probe measurements show that high-amplitude $\tilde{\Phi}_P$ and $\tilde{E}_r$ fluctuations are driven in ULq plasmas with a strong dependence on q_a and $\bar{n}_e$. RMS $\tilde{\Phi}_P$ amplitudes shown little variation with q_a; however, the $\tilde{\Phi}_P$ autopower spectra broaden significantly and shift to higher frequencies at $q_a = 0.65$. At low $\bar{n}_e$, $\tilde{E}_r$ autopower spectra are very broadband and have the highest RMS amplitudes at $q_a = 0.65$. The $\tilde{\Phi}_P$ spectra show significant coherence with $\tilde{B}_P$ measured at the edge around the frequencies where the $\tilde{\Phi}_P$ and $\tilde{B}_P$ autopower spectra peak. Coherence is also observed between $\tilde{\Phi}_P$ and $\bar{n}_e$ fluctuations at the same frequencies. As $\bar{n}_e$ decreases in the $q_a = 0.65$ case, $\tilde{\Phi}_P$ RMS amplitudes increase, and the autopower spectra broaden and shift to higher frequencies. Also, the $\tilde{E}_r$ RMS amplitudes

increase, the autopower spectra shift from a low-frequency peak to very broadband, and the coherence between two radially-separated $\tilde{E}_r$ measurements decreases significantly.

These observations suggest that the impurity heating in ULq plasmas may be driven by strong $\tilde{E}_r$ fluctuations associated with the rotation of large-scale, radially-localized, resonant modes. The presence, location, and amplitude of the modes is strongly dependent on q_a; and the mode rotation frequencies and $\tilde{E}_r$ amplitudes are strongly dependent on $\bar{n}_e$. A power balance and estimate of possible ion heating mechanisms is presented in the following chapter.

Chapter 6

Evaluation of Potential Ion Heating Mechanisms

This chapter analyzes the $q_a = 0.65$ discharge with $\bar{n}_e = 2 \times 18^{18}\ m^{-3}$ to determine if an ion heating mechanism can be inferred from the experimental data. First, a 0-D power balance and the primary energy loss mechanisms for the B^{3+} impurities are determined, and a range of values for these loss rates are estimated. From this, an estimate of the impurity heating power necessary to sustain the observed $\bar{T}_z$ is estimated. Finally, estimates of the heating power from ion cyclotron resonance damping, stochastic heating, and viscous damping are calculated to determine their potential contributions to the B^{3+} temperatures of $\bar{T}_z \approx 150$ eV.

Some assumptions must be made about parameters for this discharge due to lack of diagnostics to measure T_e, the deuterium majority T_i, and the concentration of B^{3+} ions. Thomson scattering data from comparable ULq discharges in RFX-mod [8] shows that $T_e(r)$ at $q_a \approx 0.65$ ranges from 75 to 150 eV. For this discharge, an average of $\bar{T}_e = 125$ eV is assumed, which is consistent with the observation that B^{3+} and B^{3+} are the terminal charge states for these impurities. It is shown in the following sections that the energy loss rates

are sensitive to the deuterium majority T_i; so, they will be evaluated for minimum and maximum values of $\bar{T}_i = 10$ and 125 eV. The use of this range is informed by data from ULq experiments in REPUTE [25] which showed that majority $\bar{T}_i$ was generally less than impurity $\bar{T}_z$ but comparable to $\bar{T}_e$. Impurity studies on MST RFPs have shown that the concentration of boron impurities is typically in the range of $n_z \approx$ 0.1-0.5% of n_e [70] [71]. A B^{3+} concentration of 0.1% of the plasma density or $\bar{n}_z \approx 2 \times 10^{15}\ m^{-3}$ is assumed. The plasma volume V_P is approximately 8 m^3.

6.1 Power Balance

A power balance equation for majority ions is derived in [72] beginning with the Braginskii fluid equations for continuity and energy transport [53]. This derivation results in the power balance equation

$$\frac{d}{dt}U_{therm} = P_{cond} + P_{flow} + P_{eq} + P_{ionize} + P_{CX}\ , \tag{6.1}$$

where $\frac{d}{dt}U_{therm}$ is time rate of change of ion thermal energy, P_{eq} is the rate of energy change due to temperature equilibration with other species, P_{cond} is the rate of energy change due to thermal conduction, P_{ionize} is the rate of energy change due ions being sourced by ionization, P_{CX} is the rate of energy loss due to loss of ions via charge exchange reactions, and P_{flow} is the rate of energy change due to convection and compression. Radiated power is neglected since it primarily depletes electron thermal energy and is not a direct energy sink for the ions. This power balance is modified and simplified for a 0-D power balance estimate for the impurity B^{3+} ions in ULq plasmas as follows.

In an ULq plasma with steady parameters the B^{3+} $\bar{T}_z$ is roughly constant and $\bar{n}_z$ is assumed constant such that $\frac{d}{dt}U_{therm} \approx 0$. To reach this equilibrium, $\bar{T}_z$ increases until the energy loss rate from the B^{3+} ions balances the heating power delivered to them. P_{eq} is assumed to have two components $P_{eq} = P_{z-i} + P_{z-e}$ where P_{z-i} is the power lost to collisional

cooling on majority ions and P_{z-e} is the power lost to collisional cooling on electrons. P_{flow} and P_{cond} are combined into one term $P_{trans.} = P_{flow} + P_{cond}$ which represents the total power loss due to cross-field particle transport and conduction of thermal energy out of the impurity species. Compression is neglected. Since n_z is constant and B^{+4} species are not observed, the loss rate of B^{3+} particles due to charge exchange reactions and recombination must be balanced by ionization of B^{+2} to B^{3+}. It is assumed that the B^{+2} ions which are ionized to B^{3+} are cold such that $P_{ionize} \approx 0$. An additional term, $P_{rec.}$, is added to represent the loss of power due to hot B^{3+} ions recombining with electrons to form B^{+2}. $\bar{T}_e < \bar{T}_z$ is assumed such that electrons can not heat the impurities, and it is shown in the following sections that the collisional coupling between electrons and impurities, and any potential heating by the electrons, is negligible. An additional term, $P_{anom.}$, is added which represents the anomalous ion heating power from some non-collisional heating mechanism. The power balance for the B^{3+} ions, with heating terms on the left and cooling terms on the right, in this simplified model is

$$P_{anom.} = P_{trans.} + P_{z-i} + P_{z-e} + P_{CX} + P_{rec.} \tag{6.2}$$

In the following section, each of the terms in equation 6.2 are estimated to determine what anomalous heating power $P_{anom.}$ is required to sustain the observed B^{3+} $\bar{T}_z$.

6.1.1 Transport Losses

To estimate the energy loss rate from loss of B^{3+} particles leaving the plasma due to cross-field transport, it is assumed that the B^{3+} ions have the same energy confinement as the bulk plasma. This may be an overestimate of the B^{3+} transport losses as the electron transport and radiative loss rates are likely greater than the impurity energy loss rate. Still, this provides an upper bound on the B^{3+} transport loss rate and a value to compare to the other

terms in power balance.

The global energy confinement time τ_E can be approximated by

$$\tau_E = \frac{W_P}{P_{Ohm}} \approx \frac{\frac{3}{2}\bar{n}_e(\bar{T}_i + \bar{T}_e)V_P}{I_P V_{Loop}} \tag{6.3}$$

where W_P is the plasmas thermal energy, P_{Ohm} is the Ohmic input power, and V_{Loop} is the applied loop voltage. The Ohmic input power for this discharge is $P_{Ohm} \approx 10$ MW. Evaluating for $\bar{n}_e = 2 \times 18^{18}\ m^{-3}$ and the two majority $\bar{T}_i$ values of 10 and 125 eV yields an energy confinement time of $\tau_E \approx$ 50-100 μs. Assuming the B^{3+} energy confinement is equal to the global energy confinement, the energy loss rate is calculated with

$$P_{trans.} \approx \frac{W_z}{\tau_E} \approx \frac{\frac{3}{2}n_z\bar{T}_z V_P}{\tau_E}\ , \tag{6.4}$$

where W_z is the thermal energy of the B^{3+} species with $\bar{n}_z \approx 2 \times 10^{15}\ m^{-3}$. Using the energy confinement time estimates of τ_e between 50 to 100 μs gives a loss rate of $P_{trans.}$ between 5 to 11 kW.

6.1.2 Collisional coupling to majority ions

The energy relaxation rate for two thermal particle distributions, notated here for an impurity "α" relaxing with majority ions "i", $\bar{\nu}_\epsilon^{\alpha/i}$ is approximated by [73]

$$\bar{\nu}_\epsilon^{\alpha/i} = \frac{n_i e^4 Z_\alpha^2 Z_i^2 \ln\Lambda_{\alpha i}}{m_i m_\alpha \pi^{3/2}\epsilon_0^2 v_{T_{\alpha i}}^3}\ , \tag{6.5}$$

where $v_{T_{\alpha i}}$ is defined as

$$v_{T_{\alpha i}} = \left(\frac{2T_\alpha}{m_\alpha} + \frac{2T_i}{m_i}\right)^{1/2}\ . \tag{6.6}$$

Using values for B^{3+} and deuterium at T_i = 10-125 eV yields an energy equilibration time scale of $\tau_\epsilon^{\alpha/i} \approx$ 30-260 μs. Repeating the calculation for B^{3+} impurities equilibrating with other boron ions or carbon ions with $\bar{T}_z = 150$ eV results in a $\tau_\epsilon^{\alpha/i} \geq$1.5 ms. Comparing these

values to the global energy confinement time of ∼100 μs implies that B^{3+} impurities have insignificant collisional coupling to other minority species, but the cooling on the majority deuterium ions is significant. The collisional cooling rate of B^{3+} ions on the deuterium majority is calculated with

$$P_{z-i} = V_P \, \bar{\nu}_\epsilon^{\alpha/i} \, n_z (\bar{T}_z - \bar{T}_i) \; , \tag{6.7}$$

where $n_z \approx 2 \times 10^{15} \; m^{-3}$ is the density of B^{3+} ions. Evaluating for the assumed values of $\bar{T}_i$ between 10 and 125 eV yields cooling rates of P_{z-i} between 0.25 to 11 kW.

6.1.3 Collisional coupling to electrons

The collisional energy transfer rate from ions to electrons, $\bar{\nu}_\epsilon^{\alpha/e}$, can be calculated using equation 6.5 and replacing the majority ion parameters with values for electrons. Evaluating for $\bar{T}_e = 125$ eV gives a value of $\tau_\epsilon^{\alpha/e} \approx$12 ms which is much longer than the global energy confinement time. The impurity-electron cooling power is calculated with

$$P_{z-e} = V_P \, \bar{\nu}_\epsilon^{\alpha/e} \, n_z (\bar{T}_z - \bar{T}_e) \; . \tag{6.8}$$

Evaluating this gives a cooling rate of $P_{z-e} \approx 5$ W which is negligible compared to the impurity cooling on the majority ions P_{z-i}.

Since the $\bar{T}_e$ is expected to be less than $\bar{T}_z$, the electrons should not couple any heating power to the B^{3+} species via thermal relaxation at steady-state. However, suppose that $\bar{T}_e > \bar{T}_z$ with $\bar{T}_e = 200$ eV and $\bar{T}_z = 150$ eV so that electron-impurity heating can occur. The temperature relaxation time scale then becomes $\tau_\epsilon^{\alpha/e} \gtrsim 20$ ms, and the collisional heating of the B^{3+} ions by electrons is $P_{e-z} \approx 5$ W. Thus, even if $\bar{T}_e$ were greater than $\bar{T}_z$, the energy transfer rate would be far too low to contribute significantly to the observed $\bar{T}_z$. The electrons are mostly decoupled from the impurities, and P_{e-z} and P_{z-e} are both negligible.

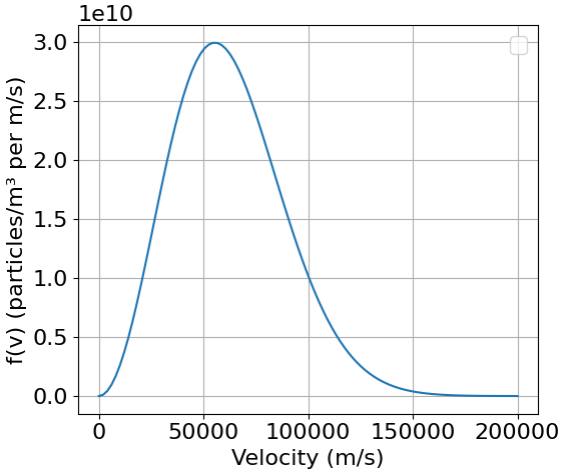

Figure 6.1: Maxwellian distribution of B^{3+} ions at 0.1% concentration as a function of ion velocity.

6.1.4 Charge exchange and recombination

The rate of B^{3+} particle loss due to charge-exchange with neutral deuterium can be estimated using values of the charge exchange cross-section and an estimate of the neutral density. The rate of charge-exchange reactions R_{CX} is calculated with [74]

$$R_{CX} = V_P \, n_n \int_0^\infty f(v)\sigma(v)v \, dv \ , \tag{6.9}$$

where n_n is the neutral deuterium particle density, $f(v)$ is the distribution of B^{3+} particles as a function of velocity, $\sigma(v)$ is the total charge-exchange cross-section for B^{3+} and neutral deuterium as a function of velocity, and v is the relative velocity between B^{3+} and deuterium neutrals. Assuming the distribution of B^{3+} ion velocities is Maxwellian of the form

$$f(v) = n_z \left(\frac{1}{\pi v_{th}^2} \right)^{3/2} 4\pi v^2 \exp\left(-\frac{v^2}{v_{th}^2} \right) \ , \tag{6.10}$$

a particle distribution as a function of v is generated using $\bar{T}_z = 150$ eV and a B^{3+} ion density of $n_z = 2{\times}10^{15}\ m^{-3}$, shown in Figure 6.1. From [75], the total cross section σ_{CX} for neutral hydrogen charge-exchanging with B^{3+} is given for several values of relative velocity. A value of $\sigma_{CX} \approx 3 \times 10^{16}\ cm^2$ is provided for a relative velocity of $2{\times}10^5$ m/s which is the

lowest relative velocity provided in this dataset. This velocity is greater than but comparable to the thermal velocity of the B^{3+} distribution in this calculation, and σ_{CX} has a trend of decreasing towards lower relative velocities. A constant value of $\sigma_{CX} = 3 \times 10^{-16}\ cm^2$ is assumed. The power lost from the B^{3+} population can be calculated by multiplying the integrand by the ion kinetic energy

$$P_{CX} = V_P\, n_n \int_0^\infty f(v)\sigma(v)v \left(\frac{1}{2}mv^2\right) dv\ , \tag{6.11}$$

If an ionization fraction of 90% for an average neutral density of $n_n = 2 \times 10^{17}\ m^{-3}$ is assumed, the calculation gives a B^{3+} charge-exchange loss rate of $R_{CX} = 5.5{\times}10^{18}\ s^{-1}$ and a charge-exchange power loss of $P_{CX} \approx 260$ Watts. If an ionization fraction of 99% is assumed, the charge-exchange power loss decreases to $P_{CX} \approx 20$ Watts. These values are negligible compared to the other terms in the power balance.

The rate of free electron recombination $R_{rec.}$ can be estimated with [74]

$$R_{rec} \approx V_P\, n_e n_z \alpha_{rec}\ , \tag{6.12}$$

where α_{rec} is the total rate coefficient for dielectronic and radiative recombination at a given $\bar{T}_e$. From [76], the total rate coefficient α_{rec} for free electron recombination with helium-like carbon C^{4+} is given as $\alpha_{rec} \approx 10^{-18}\ m^3/s$ at $T_e = 125$ eV. Since data for helium-like boron B^{3+} is not readily available, this value of α_{rec} is assumed for this estimate. Evaluating the recombination rate equation with $\bar{n}_e = 2 \times 10^{18}\ m^{-3}$ and $\bar{n}_z = 2 \times 10^{15}\ m^{-3}$ gives a recombination rate of $R_{rec.} \approx 3 \times 10^{16}\ s^{-1}$. This value is 1 to 2 orders of magnitude smaller than the rate of particle loss due to charge-exchange; so, the loss of B^{3+} particles due to free electron recombination is negligible.

6.1.5 Anomalous heating power estimate

Using the estimates above, the anomalous impurity heating power can now be inferred. These estimates are summarized in Table 6.1

Table 6.1: Estimates of heating and loss rates for B^{3+} impurities.

Process	**Power Estimate**
Transport losses (P_{trans})	5–11 kW
Cooling on majority ions ($P_{z\text{-}i}$)	0.25–11 kW
Cooling on electrons ($P_{z\text{-}e}$)	∼5 W
Heating from electrons ($P_{e\text{-}z}$)	∼5 W
Charge exchange (P_{CX})	20–260 W
Recombination ($P_{\text{rec.}}$)	<20 W
Coupling to other impurities	Negligible

Neglecting the insignificant contributions from P_{z-e}, P_{CX} , and $P_{rec.}$, the B^{3+} power balance becomes

$$P_{anom.} = P_{trans.} + P_{z-i} \ . \tag{6.13}$$

Using the ranges of power loss rates gives an anomalous B^{3+} heating power of $P_{anom.} \approx$ 5-22 kW. In the following section, impurity ion heating mechanisms are evaluated to determine if any of the mechanisms can deliver this anomalous heating power.

6.2 Ion Cyclotron Resonance Heating

The ion gyro frequency ω_{ci} is given by

$$\omega_{ci} = \frac{qB}{m_i}, \tag{6.14}$$

and a B^{3+} ion in a magnetic field of 1400-1700 G has a gyro frequency of $\omega_{ci} \approx 3.6 - 4.4 \times 10^6$ radian/s or $f_{ci} \approx$ 580-700 kHz. For an electromagnetic wave with a left-hand polarized electric field component, the heating power density from ICR damping is given by

$$Q_{ICR} = \int \gamma(\omega) \frac{\tilde{B}^2(\omega)}{2\mu_0} d\omega \ , \tag{6.15}$$

where $\tilde{B}$ is the amplitude of the magnetic field fluctuation, and γ is the damping rate. The measurements needed to determine the polarization of the electric field component, characterize the wavenumbers of the internal magnetic fluctuations, and properly calculate $\gamma(\omega)$ were not available. However, a simple estimate using reasonable assumptions can be used to determine if it is feasible that the measured magnetic fluctuations can supply the estimated impurity heating power.

For an upper limit estimate of the ICR heating power, it is assumed that all of the magnetic fluctuations in the 450-850 kHz band can couple to B^{3+} ions and that the fluctuation amplitudes are uniform over the plasma volume. This frequency band is chosen arbitrarily to ensure that all frequencies that can potentially ICR damp are included; it is almost certainly an overestimate of the resonance band. The analog-integrated insertable magnetics probe measurements are limited in bandwidth to 250 kHz, and they show no significant change in fluctuation amplitudes with radius at 100 kHz. The fluctuations measured by a dense array B_P coil at the edge are used for this estimate, and it is assumed that the high-frequency fluctuations at the edge are uniform throughout the plasma volume. The ICR damping is evaluated for weak damping with $\gamma(\omega) = 0.01\omega$ and strong damping with $\gamma(\omega) = 0.1\omega$. This calculation gives a heating power estimate of P_{ICR} between 14 and 140 W for this range of damping rates.

If ICR damping is responsible for the impurity heating, then the fluctuation power in frequencies near ω_{ci} may show a trend similar to the B^{3+} $\bar{T}_z$ throughout the parameter scans. Plots of $\tilde{B}_P$ fluctuation power in the 450-850 kHZ band and $\bar{T}_z$ from the q_a scan are shown in Figure 6.2. Note that R_P does decrease significantly at $q_a \approx 0.55$-0.6 (see Figure 4.3), and a gradual decrease in $\bar{T}_e$ is expected as q_a decreases (see Figure 2.8). So, energy confinement may be changing significantly across the q_a scan. Notice that the $\tilde{B}_P$ fluctuation power varies significantly but does not show a similar trend to that seen in $\bar{T}_z$. Although not conclusive,

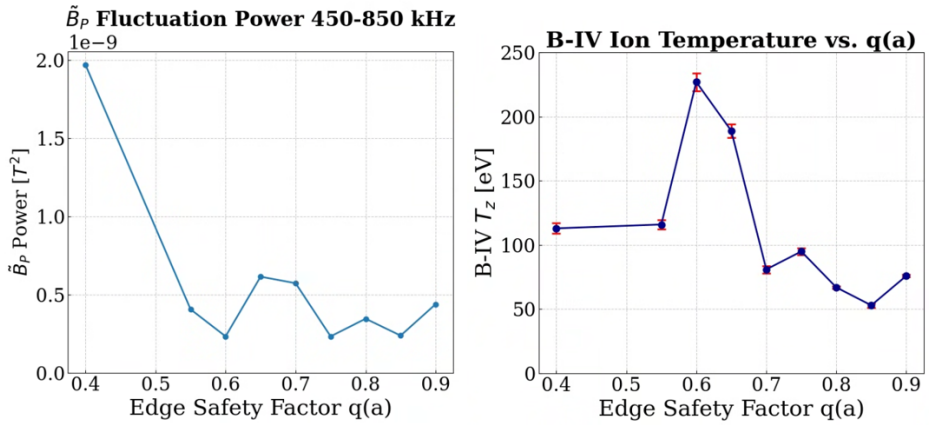

Figure 6.2: (Left) $\tilde{B}_P$ fluctuation power integrated from 450 to 850 kHz vs q_a. Fluctuation spectrum from dense array coil is used. (Right) B^{3+} $\bar{T}_z$ vs. q_a

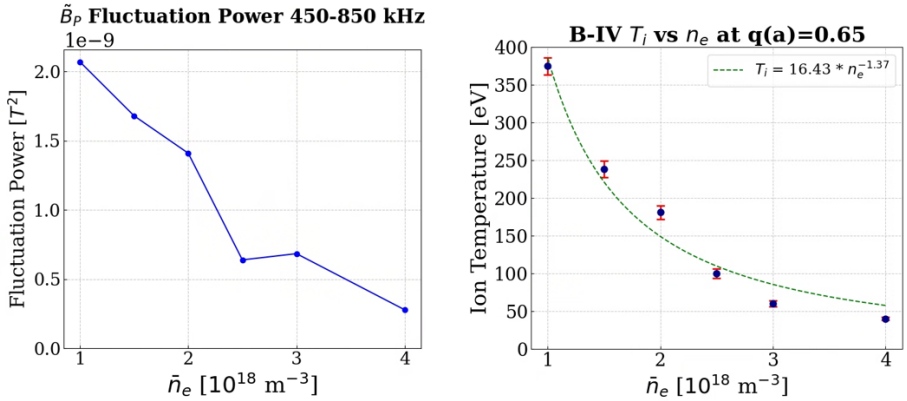

Figure 6.3: (Left) $\tilde{B}_P$ fluctuation power integrated from 450 to 850 kHz vs $\bar{n}_e$. (Right) B^{3+} $\bar{T}_z$ vs. $\bar{n}_e$

this scan does not show a clear relation between $\tilde{B}_P$ power and $\bar{T}_z$.

Plots of $\tilde{B}_P$ fluctuation power over the 450-850 kHZ band and $\bar{T}_z$ from the $\bar{n}_e$ scan are shown in Figure 6.3. Notice that the increase in $\tilde{B}_P$ fluctuation power shows a trend similar to the increase in B^{3+} $\bar{T}_Z$.

The small values of $P_{ICR} \approx$ 14-140 W suggest that the fluctuation amplitudes are too small for ICR damping to account for the B^{3+} $\bar{T}_z$ observed. The dissimilar trends in $\tilde{B}_P$ fluctuation amplitudes and $\bar{T}_z$ suggest that ICR damping is not responsible for the variation in $\bar{T}_z$ during the q_a scan. However, a similar trend in $\tilde{B}_P$ fluctuation amplitudes and $\bar{T}_z$ is observed in the $\bar{n}_e$ scan, which suggests that high-frequency $\tilde{B}_P$ may play a role in impurity

heating, but the heating power from the ICR damping estimate is too small to explain the observations. Together, these observations suggest that ICR damping is not the dominant impurity heating mechanism in ULq plasmas.

6.3 Stochastic Heating

Experimental evidence and modeling of stochastic ion heating due to large-amplitude drift waves is described in [51]. In this model, stochastic heating becomes possible when the ion displacement due to polarization drift becomes comparable to the perpendicular wavelength of the wave. This is condition is characterized by the parameter α defined as

$$\alpha = \frac{k_\perp^2 m_i \Phi_0}{q B_0^2} \quad , \tag{6.16}$$

where $k_\perp$ is the perpendicular wavenumber of the potential fluctuations, m_i is the mass of the ion, Φ_0 is the peak amplitude of the potential fluctuations, q is the charge of the ion, and B_0 is the equilibrium magnetic field strength. In this model, stochastic heating becomes possible when $\alpha \geq 1$. In chapter 5, $\tilde{\Phi}_P$ for the $q_a = 0.65$ case was shown to be dominated by $\sim$18 kHz fluctuations. These $\tilde{\Phi}_P$ fluctuations have $k_r \approx 7.5$ radian/m or a wavelength of $\sim$80 cm and an average peak potential of $\Phi_0 \approx 250$ V. Evaluating the α parameter with these values gives a value of $\alpha \approx 0.02$. Thus, stochastic heating from these large-scale fluctuations would not be possible in MST ULq experiments in this model. The coherent $\tilde{\Phi}_P$ fluctuations up to 100 kHz have similar k_r with lower amplitudes and would also be insufficient to heat in this model. However, observations in Chapter 5 also show that there are broadband $\tilde{E}_r$ fluctuations with significant amplitudes that are incoherent at a separation of 1.4 cm.

Ion heating in the presence of stochastic magnetic fields and high-amplitude electric field fluctuations was modeled in [24]. In this model, the time rate of change in average perpendicular kinetic energy of ions experiencing random cross-field motion due to radially-

wandering stochastic magnetic field lines through an uncorrelated $\tilde{E}_r$ is given by

$$K(t) = \frac{1}{2} m_i v_\perp^2(t) \approx \frac{1}{2} m_i t D_v = \frac{1}{2\tau} m_i v_E^2 t, \tag{6.17}$$

where $D_v = v_E^2/\tau$ is the perpendicular velocity diffusion coefficient, $v_E = E_r/B_0$ is the perpendicular drift velocity, and the time step $\tau \approx \delta_r^2/D_\perp$ is estimated as the average time for an ion to traverse the radial correlation length of the electric field δ_r. The stochastic heating power density Q_{stoch} is then

$$Q_{stoch} = n_i \frac{dK}{dt} = n_i \frac{m_i v_E^2}{2\tau} = n_i \frac{m_i D_\perp \tilde{E}_r^2}{2\delta_r^2 B_0^2} \, . \tag{6.18}$$

$D_\perp$ is calculated using the stochastic magnetic diffusivity D_M with

$$D_\perp = c_s D_M = c_s \pi q R_0 \left(\frac{\tilde{B}_r}{B_0} \right)^2 , \tag{6.19}$$

where c_s is the plasma sound speed. The RMS amplitude of B_r fluctuations is $\sim$1.6 mT, which gives a value of $\frac{\tilde{B}_r}{B_0} = 0.01$ for a $B_0 \approx 0.16$ T. Using these parameters and a sound speed estimate of $c_s = 5.4 \times 10^4$ m/s gives $D_\perp \approx 16.5\ m^2/s$. As shown in chapter 5, the average amplitude of the $\tilde{E}_r$ fluctuations is $\sim$11 kV/m, and no significant coherence is measured with a radial separation of 1.4 cm, which indicates a short correlation length of $\delta r < 2$ cm. Using these parameters and $\delta_r = 2$ cm results in a stochastic heating power of $P_{stoch.} \approx 26$ kW for the B^{3+} impurities.

It is interesting to note that the $D_\perp$ from stochastic diffusion is small considering the global energy confinement of the plasma. An approximation for the thermal diffusion coefficient χ_T is given by [15]

$$\chi_T \approx \frac{a^2}{4\tau_E} \, , \tag{6.20}$$

where a is the plasma minor radius, and τ_E is the energy confinement time. This approximation gives a value of $\chi_T \gtrsim 600\ m^2/s$. This suggests that the observed energy confinement properties of ULq plasmas cannot be explained by stochastic transport alone. If $D_\perp$ is

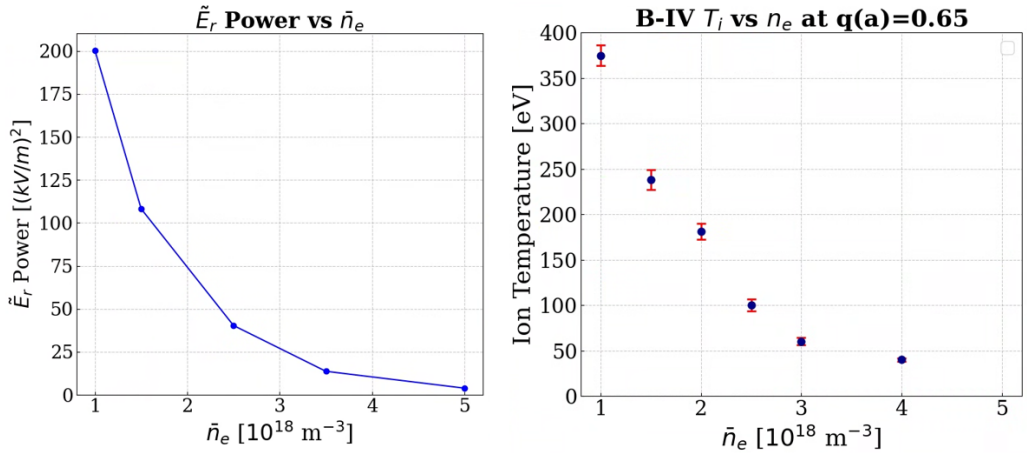

Figure 6.4: For the $q_a = 0.65$ case, (Left) $\tilde{E}_r$ fluctuation power vs. $\bar{n}_e$. $\tilde{E}_r$ power spectrum was integrated for frequencies up to 200 kHz, and low-frequency fluctuations which were coherent at 1.4 cm separation were excluded. (Right) $\bar{T}_z$ vs. $\bar{n}_e$.

comparable to χ_T then this calculation of stochastic heating power may be an underestimate since the particle transport may be significantly higher than the stochastic transport estimate. However, it is unknown how much radiative losses contribute to the energy confinement properties or how a different transport mechanism would change this stochastic heating model.

It was shown in chapter 5 that, as $\bar{n}_e$ decreases, the RMS amplitude of the $\tilde{E}_r$ fluctuations increases and their power spectra broaden significantly. A plot of the integrated $\tilde{E}_r$ fluctuation power for several $\bar{n}_e$ values is shown in 6.4 and compared to the $\bar{T}_z$ values from the $\bar{n}_e$ scan. The $\tilde{E}_r$ spectra were integrated for frequencies up to 200 kHz. The lower frequency bound was varied in order to exclude fluctuations which had significant coherence at 1.4 cm separation. Notice that the trend in $\tilde{E}_r$ power values resembles the trend in $\bar{T}_z$ quite well.

It was also shown in chapter 5 that, as q_a was varied, the RMS amplitude of the $\tilde{E}_r$ fluctuations and their spectra varied significantly. A plot of the $\tilde{E}_r$ fluctuation power for several q_a values at fixed $\bar{n}_e \approx 2 \times 10^{18}\ m^{-3}$ is shown in 6.5 and compared to the $\bar{T}_z$ values from the q_a scan. As in the previous plot, low frequency coherent fluctuations were excluded

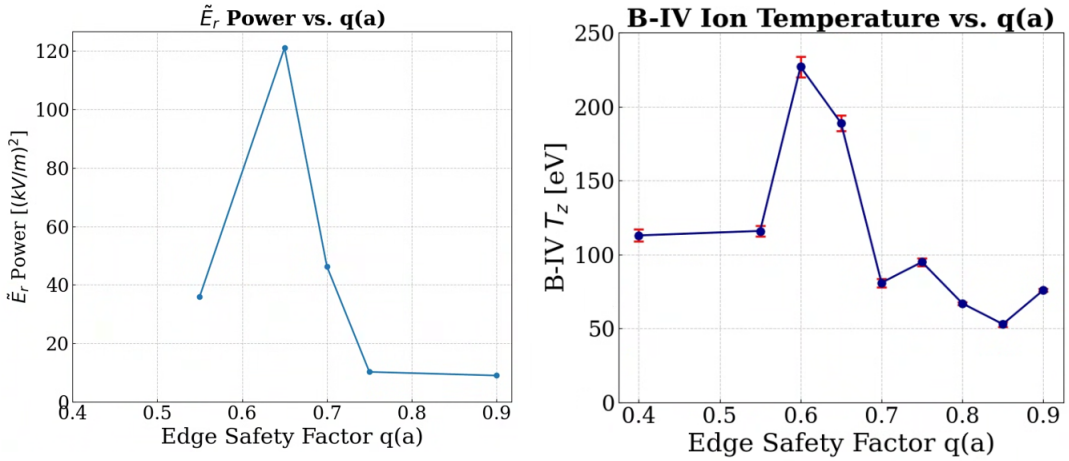

Figure 6.5: At fixed $\bar{n}_e$, (Left) $\tilde{E}_r$ power vs. q_a. $\tilde{E}_r$ power spectrum was integrated for frequencies up to 200 kHz, and low-frequency fluctuations which were coherent at 1.4 cm separation were excluded. (Right) $\bar{T}_z$ vs. q_a.

from the power spectra integration. Notice that the trend in $\tilde{E}_r$ power values again resembles the trend in $\bar{T}_z$.

The estimated stochastic heating power of $P_{stoch.} \approx 26$ kW is consistent with the estimate of the required anomalous heating power of $P_{anom} \approx$ 5-22 kW. This suggests that the measured $\tilde{B}_r$ and $\tilde{E}_r$ fluctuation amplitudes and $\tilde{E}_r$ coherence lengths are sufficient to account for the observed $\bar{T}_z$ via stochastic heating. The trend in $\tilde{E}_r$ fluctuation power is very similar to the $\bar{T}_z$ trend from the $\bar{n}_e$ scan, which suggests that the increase in broadband $\tilde{E}_r$ fluctuations contributes to the significant increase in $\bar{T}_z$ with decreasing $\bar{n}_e$. The trends in $\tilde{E}_r$ fluctuation power and $\bar{T}_z$ are also similar in the q_a scan. These observations suggest that the observed impurity heating is a result of stochastic heating by broadband $\tilde{E}_r$ fluctuations.

6.4 Viscous Heating

The dissipation per unit volume due to a radial shear in toroidal flow speed v_ϕ is calculated with

$$Q_{visc} = \eta_\perp \left(\frac{dv_\phi}{dr} \right)^2 , \tag{6.21}$$

where $\eta_\perp$ is the perpendicular viscosity. A simple slab geometry model can be used to estimate the upper limit of the heating from viscous dissipation. For this estimate, suppose that an island chain is formed at the $q(r) = 2/3$ rational surface which rotates toroidally at the velocity of the $n = 3$ mode while the rest of the plasma is stationary. Assume that this rotation forms a linear flow shear layer between the island chain and the bulk plasma with a layer thickness of Δr. The total viscous dissipation on both side of the island is

$$P_{visc} = 2\, V_l\, \eta_\perp \left(\frac{\partial v_\phi}{\partial r}\right)^2 = 2\left(4\pi^2 r_i R \Delta r\right) \eta_\perp \left(\frac{\Delta v_\phi}{\Delta r}\right)^2 . \tag{6.22}$$

where V_l is the volume of the shear flow layer, r_i is the radial distance of the resonant surface from the geometric axis, and R is the major radius. $\eta_\perp$ is given by

$$\eta_\perp = \frac{3}{10} n_i m_i \tau_{ii} \frac{v_{th}}{\omega_{ci}} , \tag{6.23}$$

where n_i is the ion density, m_i is the ion mass, τ_{ii} is the ion-ion collision timescale, and v_{th} is the ion thermal speed. This gives a viscosity of $\eta_\perp \approx 1.5 \times 10^{-10}\ Pa \cdot s$. The fastest toroidal rotation speed measured for this discharge was the $n = 3$ at 45 km/s. Using values of r_i=35 cm, Δv_ϕ = 45 km/s, and Δr = 5 cm gives a viscous dissipation of ~100 W for the majority deuterium ions. If the layer thickness is reduced to Δr = 1 cm, the viscous dissipation increases to ~600 W. Since the density of B^{3+} is orders of magnitude lower than the majority, it is unlikely that viscous dissipation can account for the heating power necessary to sustain the observed $\bar{T}_z$.

Chapter 7

Conclusion

In this thesis work, novel experiments have been performed to characterize the discharge behavior and anomalous impurity heating observed in ULq plasmas in MST. ULq plasmas lie in the regime of toroidal pinch plasmas between the tokamak and RFP. The tokamak with $q_a > 2$ has $q(r) \gtrsim 1$ and significant magnetic shear which gives it good average field line curvature and stability to pressure-driven modes. The RFP with $q_a < 0$ has $q(r) < 1$ which gives it bad field line curvature and would make the configuration susceptible to interchange modes; however, the RFP $q(r)$ profile also gives it strong magnetic shear which stabilizes interchange across much of the plasma radius and yields confinement properties comparable to the tokamak.

ULq plasmas with $0 < q_a < 1$ have both $q(r) < 1$ and very small magnetic shear which causes them to be unstable to ideal interchange modes. Particle and energy confinement is significantly degraded in ULq plasmas compared to the tokamak and RFP which causes them to have high global plasma resistance, and their high resistivity has made them difficult to sustain and study in past experiments. In MST, ULq plasmas can now be sustained for durations much greater than their energy confinement time due to the external-kink stabilization of its conducting shell, high-bandwidth feedback power supplies which can

apply up to 120 loop volts, and this thesis work which has determined how to operate and sustain ULq plasmas with steady parameters. These plasmas provide a unique platform for experimental research in a regime rich in unexplored physics which was not previously available. ULq plasmas exhibit strong magnetic, electron density, and plasma potential fluctuations which may be due to a combination of both tearing and interchange modes.

In the RFP, closely-spaced magnetic islands exhibit sudden non-linear interactions during sawtooth events, and the resulting global reconnection events drive bursts of non-collisional ion heating. There is also a continuous non-collisional ion heating mechanism active in the RFP, but no significant non-collisional ion heating is observed in the tokamak. Impurity temperatures in ULq plasmas are anomalously high with B^{3+} $\bar{T}_z$ up to $3\times T_e$ observed. When other parameters are steady, $\bar{T}_z$ is nearly continuous and does not appear correlated with fluctuations in I_P or B_T. Discrete relaxation events like the RFP sawtooth and tokamak sawtooth are not observed in sustained ULq plasmas. $\bar{T}_z$ has a strong dependence on q_a, $\bar{n}_e$, and equilibrium magnetic field strength. Measurements of B_r and E_r fluctuations, an approximation of the impurity power balance, and estimates of the possible heating mechanisms suggest that the high impurity temperatures are due to stochastic heating. This heating mechanism may also play a role in the RFP ion heating.

7.1 Summary of Observations

Compared to tokamak conditions in MST, ULq plasmas require much greater deuterium fueling rates in order to maintain comparable plasma densities. ULq plasma startup is most reproducible when the applied loop voltage and I_P ramp rate are maximized and a large amount of gas is puffed 5 ms before beginning the current ramp. Insufficient I_P ramp rate or deuterium fueling results in disruption-like behavior featuring strong magnetic fluctuations, bursts of x-rays, loss of plasma density, and loss of I_P. The global plasma resistance is

highly dependent on q_a and is observed to increase roughly linearly with decreasing $\bar{n}_e$ for discharges with $\bar{n}_e < 5 \times 10^{18}\ m^{-3}$. Above this threshold value of $\bar{n}_e$, the trend inverts and plasma resistance increases with increasing $\bar{n}_e$ which is the typical behavior for tokamak and RFP plasmas. In the low-density regime, ULq plasmas are minimally responsive to increases in neutral fueling rates. It is notable that this threshold $\bar{n}_e$ value is the same value where $\bar{T}_z$ becomes high enough to be resolved by the available diagnostic, and $\bar{T}_z$ increases with decreasing $\bar{n}_e$.

In ULq plasmas, $\tilde{B}_P$ amplitudes can reach up to ~5% of the edge B_P, significantly greater than the normalized amplitudes in the tokamak and RFP. The magnetic fluctuations tend be dominated by resonant helical modes whose value of m/n is closest to q_a. As q_a is decreased from 1 to 0.6, the dominant B_P toroidal harmonics will transition through $n = 1, 4, 3, 5$ as the $q(r) = 1, \frac{3}{4}, \frac{2}{3}, \frac{3}{5}$ rational surfaces emerge near the core, approach the plasma edge, and leave the plasma. This is consistent with observations in simulations and experiments of ULq plasmas in RFX-mod [8]. The B_P toroidal harmonic amplitudes and rotation speeds are highly dependent on q_a and $\bar{n}_e$, and the rotation speeds can reach a significant fraction of the ion sound speed in the low-density regime. The direction of rotation is typically opposite to the direction of rotation in the RFP. Both the $\bar{n}_e(r)$ profiles and the poloidal asymmetry factors of ULq plasmas indicate that the current density profiles and pressure profiles are flattened compared to the tokamak and RFP. However, core-peaked pressure profiles are still observed.

The scan of q_a over the range $0.4 < q_a < 0.9$ shows that $\bar{T}_z$ and global plasma resistance tend to increase as q_a is lowered towards $q_a \approx 0.65$, and decreasing further to $q_a \approx 0.55$ results in a significant decrease in plasma resistance, magnetic fluctuation amplitudes, and $\bar{T}_z$. The trend in $\bar{T}_z$ is similar to the trend in $\tilde{B}_T$ and $\tilde{B}_P$ fluctuation amplitudes at 10-50 kHz as well as the amplitudes and rotation frequencies of the dominant B_P toroidal harmonics.

There is also a similar trend in high-frequency $\tilde{n}_e$ fluctuation amplitudes, but not for the highest-amplitude fluctuations which have frequencies $\leq$5 kHz. At $q_a = 0.65$, the $\bar{n}_e(r)$ and the $\bar{T}_z(r)$ profiles are core-peaked and symmetric about the expected location of the magnetic axis. These observations suggest that the impurity heating is associated with fluctuations resulting from the rotation of large-amplitude resonant modes.

The scan of $\bar{n}_e$ over the range $1 \leq \bar{n}_e \leq 4 \times 10^{18}\ m^{-3}$ shows that there is a greater than linear increase in $\bar{T}_z$ as $\bar{n}_e$ decreases while Ohmic input power increases roughly linearly. The trend in $\bar{T}_z$ is similar to the trend of increasing rotation frequency of the dominant $n = 3$ B_P harmonic and increasing 10-50 kHz magnetic fluctuation amplitudes. At high $\bar{n}_e$, the $\bar{n}_e$ fluctuations are predominantly at frequencies $\leq$5 kHz, but the spectra become more broadband at low $\bar{n}_e$ without significant change in higher-frequency fluctuation amplitudes. These observations suggest that the impurity heating is associated with the increase in rotation frequency of the resonant modes or the change in conditions which causes the increase in rotation speeds.

An increase of B_T and I_P at fixed $q_a = 0.65$ results in a linear increase in $\bar{T}_z$ as well as a slight increase in B_P toroidal harmonic amplitudes; however, normalized amplitudes slightly decrease. B_P toroidal harmonic rotation frequencies remain nearly constant in this scan. High-frequency magnetic fluctuation amplitudes increase with increasing B_T and I_P, but the $\bar{n}_e$ fluctuation amplitudes show no significant change through the scan. These observations suggest that the increase in $\bar{T}_z$ in this scan is associated with increasing broadband magnetic fluctuation amplitudes and possibly enhanced impurity energy confinement from the increasing magnetic field.

The discharges with $q_a = 0.7$, 0.65, and 0.55 are characterized more thoroughly due to their significant change in magnetic fluctuation amplitudes, $\bar{T}_z$, and global plasma resistance. Beginning with magnetic fluctuations at the plasma edge, the $q_a = 0.7$ case has the

largest-amplitude fluctuations with a spectral peak near 4 kHz and no discernible peaks at higher frequencies. When q_a is decreased to 0.65, the low-frequency amplitudes decrease by about 50% and a broadband peak of similar amplitude appears near 17 kHz. Decreasing to $q_a = 0.55$ results in a significant decrease in low-frequency fluctuation amplitudes and slight increase in higher-frequency fluctuation amplitudes, resulting in a very broadband spectrum. Fluctuations in the $q_a = 0.7$ and 0.65 cases are both dominated by an $n = 3$ B_P harmonic which increases in amplitude and frequency in the $q_a = 0.65$ case. The $q_a = 0.55$ case has no clear dominant harmonic, but the $n = 5$ does appear to have marginally larger amplitude than other components.

Internal magnetic fluctuations for the three q_a cases are characterized with measurements from an insertable probe coil array inserted to 35 cm within the plasma edge. Outboard radial profiles of $\tilde{B}_P$, $\tilde{B}_T$, and $\tilde{B}_r$ fluctuation autopower spectra show significant change as q_a is varied. The observations suggest that a low-frequency, core-localized $m/n = 2/3$ mode increases in amplitude and frequency and shifts to mid-radius as q_a is decreased from 0.7 to 0.65. Decreasing to $q_a = 0.55$ results in a loss of the $m/n = 2/3$ mode and appearance of a core-localized mode sourcing lower-amplitude, broadband fluctuations. This is consistent with the loss of $q(r) = 2/3$ and emergence of a $q(r) = 2/5$ rational surface near the core, but the broadband fluctuations and distance from the core the the toroidal array coils make it difficult clearly identify a dominant harmonic. The phase relationships between the three magnetic field components are consistent with the rotation of global helical structures. The radial coherence length scales of the magnetic fluctuations are 8 cm to 15 cm, which is consistent with fluctuations sourced by radially-localized perturbations rather than coherent motion of the whole plasma column. This coherence length scale is also consistent with the coherence being limited by the stochastic fields between multiple resonant modes.

$\bar{n}_e$ fluctuations for the three q_a cases were characterized by an 11-chord far-infrared

interferometer system spanning most of the plasma diameter. Frequency analysis of the $\bar{n}_e$ fluctuations show spectra and radial variation different from the magnetic fluctuations. $\bar{n}_e$ fluctuation autopower spectra always peak at frequencies <5 kHz even when the magnetic fluctuations peak at >10 kHz. This difference between magnetic and $\bar{n}_e$ fluctuation spectra suggests that the modes responsible for the highest-amplitude $\bar{n}_e$ fluctuations are not the same modes which dominate the magnetic spectra. In all three cases, the low-frequency $\bar{n}_e$ fluctuation amplitudes increase significantly towards the outboard edge or both the inboard and outboard edge. These are the regions where the $\bar{n}_e(r)$ gradients are strongest which is suggestive of ballooning modes, interchange modes, or helical structures perturbing the $\bar{n}_e$ gradient. Weak but significant coherence is observed between $\bar{n}_e$ fluctuations and $\tilde{B}_P$ measured at the edge at frequencies where the $\tilde{B}_P$ autopower spectra peak. This suggests that the rotation of the resonant modes contributes to the $\bar{n}_e$ fluctuations, but most of the $\bar{n}_e$ fluctuations are incoherent with edge magnetic fluctuations. The radial coherence length scales of $\bar{n}_e$ fluctuations is estimated at 4 cm to 20 cm depending on frequency.

$\tilde{\Phi}_P$ and $\tilde{E}_r$ fluctuations for the three q_a cases are characterized with a capacitive probe inserted to 6-8 cm within the plasma edge. RMS $\tilde{\Phi}_P$ amplitudes of 50-200 V and RMS $\tilde{E}_r$ amplitudes of 3-15 kV/m are observed. The $\tilde{\Phi}_P$ autopower spectra are very similar to the magnetic fluctuation spectra, and the $\tilde{E}_r$ autopower spectra are significantly more broadband. $\tilde{\Phi}_P$ shows significant coherence with edge $\tilde{B}_P$ and $\bar{n}_e$ fluctuations at frequencies where the $\tilde{\Phi}_P$ autopower spectra peak. The $\tilde{\Phi}_P$ fluctuations are strongly coherent for sensors with 2.1 cm radial separation. The radial length scales of these fluctuations appear to be much larger than the available 2.1 cm measurement separation, and the phase difference is not well-resolved. Radial wavelengths of 10's of cm to 1 m are estimated for the $\tilde{\Phi}_P$ fluctuations. RMS amplitudes of $\tilde{E}_r$ vary significantly with q_a and are largest at $q_a = 0.65$. $\tilde{\Phi}_P$ and $\tilde{E}_r$ amplitudes increase significantly as $\bar{n}_e$ is decreased. For the $q_a = 0.65$ case, the

$\tilde{E}_r$ autopower spectra gradually shift from a narrow peak near 5 kHz to very broadband spectra extending beyond 100 kHz as $\bar{n}_e$ decreases, and the coherence between independent $\tilde{E}_r$ measurements separated radially by 1.4 cm decreases.

7.2 Summary of Conclusions

Evidence is presented that suggests the strong magnetic and Φ_P fluctuations are a result of rotation of radially-localized, high-amplitude helical resonant modes. Increases in fluctuation frequencies and amplitudes are associated with increases in $\bar{T}_z$, and both depend strongly on q_a and $\bar{n}_e$. The large-scale Φ_P fluctuations observed are not expected to drive significant ion heating due to their weak $\tilde{E}_r$; however, strong broadband E_r fluctuations are also observed. These high-amplitude, broadband, short coherence length E_r fluctuations may be responsible for the impurity heating.

A power balance for the B^{3+} impurities in the $q_a = 0.65$ case is estimated to determine the anomalous heating power required to sustain the observed $\bar{T}_z = 150$ eV. Estimates of the energy loss rates suggest that the primary loss mechanisms for the B^{3+} impurities are cross-field transport losses and collisional cooling on the majority ions. The required anomalous heating power is estimated at $P_{anom.} \approx$ 5-22 kW. An estimate of the heating power from ICR damping based on the measured magnetic fluctuation amplitudes near ω_{ci} suggests that ICR damping is not able to sustain the observed $\bar{T}_z$. A heating power estimate from viscous dissipation based on the measured mode rotation speeds also results in a dissipation value too low to drive significant heating. The estimate of stochastic heating power based on the measured $\tilde{B}_r$ amplitudes and $\tilde{E}_r$ amplitudes is consistent with the anomalous heating power required to sustain the observed $\bar{T}_z$. The trends in $\tilde{E}_r$ fluctuation power are also consistent with the trends in $\bar{T}_z$ from the q_a scan and $\bar{n}_e$ scan. This work concludes that the anomalous impurity heating observed in ULq plasmas is likely the a result of stochastic

heating facilitated by strong B_r fluctuations and broadband E_r fluctuations associated with the fast rotation of resonant helical modes.

7.3 Suggestions for Future Work

7.3.1 Ion Heating

A direct continuation of this work on impurity heating would be to characterize other charge states of boron as well as other impurities and their charge states. This would be useful in determining the heating mechanism's dependence on charge and mass. In the stochastic heating model, the heating power is independent of the ion charge but proportional to mass, and ICR damping has a dependence on both charge and mass.

Since the pitch angle of the magnetic field in these ULq plasmas is $<35°$, the measurements of impurity temperatures in this work sample primarily $T_\perp$, and no conclusion about the anisotropy of the heating mechanism can be made. A set of collection optics could be developed and placed near the midplane in order to make measurements of $T_\parallel$. A demonstration of $T_\perp > T_\parallel$ would provide additional evidence for stochastic heating being the mechanism responsible for impurity heating.

Line-integrated measurements are sufficient for measuring equilibrium $\bar{T}_z$, but localized measurements would be needed in order to resolve the fluctuations in T_z and correlate with other localized measurements. This could be facilitated with the available ChERS diagnostic, but this would require fully-ionized impurity species. It is unlikely that the $\bar{T}_e$ necessary to fully ionize boron or carbon will be achieved in MST ULq plasmas. ChERS was attempted with fully-ionized helium, but the He-II emissions from the plasma edge were far too bright to allow for extraction of the active charge-exchange signal. However, it is possible that $\bar{T}_e$ is high enough to fully ionize lithium impurities if they were present. Background Li-III

emissions may be less intense than He-II emissions such that a charge-exchange signal could be extracted. It may be worthwhile to attempt doping ULq plasmas with small amounts of lithium to determine if ChERS measurements using lithium emissions are feasible.

The heating of the majority ions is also of interest, but majority ChERS is not feasible with the available diagnostic and is likely very challenging in these plasmas. A Rutherford scattering T_i diagnostic is available on MST, but it is currently not in a functional state. Reviving the Rutherford scattering diagnostic would provide valuable information on majority T_i and how the heating varies with different majority species. A neutral particle analyzer could also provide information on majority T_i.

7.3.2 ULq Discharge Properties

A critical piece of missing information in these experiments is the $T_e(r)$ profile. The $T_e(r)$ profile, along with the $T_i(r)$ and $\bar{n}_e(r)$ profiles, would provide good constraints for equilibrium reconstructions. These reconstructions could then be used to infer how the $q(r)$ profile varies with q_a. A fast Thomson scattering diagnostic is available at MST, but is not in a functional state. Reviving this diagnostic would provide valuable information on equilibrium $T_e(r)$ and how $\tilde{T}_e$ relates to T_z and other fluctuations.

Initial measurements of neutron flux during deuterium neutral beam injection suggest that fast ions have a confinement time greater than the global energy confinement time. Evidence of fast ion acceleration is also observed. There is no literature on fast ion confinement in ULq plasmas, and characterizing it in MST may be worthwhile since the neutral beam and neutron scintillator diagnostics are available.

The increase in Ohmic heating power with decreasing $\bar{n}_e$ in the low-density regime is puzzling, and one possible explanation could be a significant increase in radiated power. Radiated power diagnostics are currently being implemented on MST, and they would be

useful for quantifying radiated power as $\bar{n}_e$ and q_a vary. If not attributable to radiated power, then a study on the particle transport in ULq plasmas would be necessary to explain this effect. The minimal response to gas puffing in low-density regime is another puzzling feature of ULq plasmas, and it may be related to the decrease in energy confinement. If particle confinement is decreasing significantly with $\bar{n}_e$, then the neutrals may be ionized near the edge and lost before they can diffuse into the plasma. An experimental investigation as well as modeling may be required in order to explain this phenomenon.

7.3.3 Instabilities, Flow Drive, and Turbulence

Characterizing the disruption-like behavior resulting from insufficient I_P ramp rates or insufficient neutral fueling may be of interest. Also, during startup and throughout low-density ULq discharges, bursts of x-rays are commonly observed and are believed to be a result of suprathermal electrons impacting the vessel wall. A measurement of the energy spectrum of the x-rays would be useful in determining the energies of these fast electrons. An investigation may be warranted to determine if the acceleration is due to electron runaway caused by the strong applied toroidal electric field, or if instabilities are driving the electron acceleration.

This thesis characterizes large-scale resonant modes in ULq plasmas, and evidence suggests they are associated with the anomalous ion heating. However, the available measurements are insufficient to distinguish between tearing modes and resistive interchange. Computational work on the ULq regime is in progress [47] to determine which instability is more likely to be observed and what measurements can be made in experiment to verify the theory, as was done for the RFP [77].

Very fast toroidal mode rotation speeds are observed, but it is unknown why these modes are accelerated to such high speeds. $E \times B$ drifts are suspected to be the dominant source

of flow, but it is not clear how these strong electric fields are sustained or why some modes are accelerated more than others. It is also unknown why ULq plasma modes rotate in the opposite direction that RFP modes rotate. Spectroscopic measurements of flow velocity and an investigation into the mechanism of flow drive in ULq plasmas may be of interest.

Finally, broadband small-scale $\tilde{E}_r$ fluctuations appear responsible for the anomalous ion heating, but it is not clear how these fluctuations are generated from the large-scale fluctuations and if they are electromagnetic or electrostatic fluctuations. A probe which could simultaneously measure magnetic and Φ_P fluctuations at several locations would be useful in characterizing the turbulence in ULq plasmas and understanding how energy flows from the large scale fluctuations to ion thermal energy.

Bibliography

[1] J. Wesson, *Tokamaks*, 4th ed. Oxford University Press, 2011. (*Cited on pages 1, 5, 8*)

[2] S. E. Wurzel and S. C. Hsu, "Progress toward fusion energy breakeven and gain as measured against the lawson criterion," *Physics of Plasmas*, vol. 29, 6 2022. (*Cited on page 2*)

[3] A. Kappatou, M. Baruzzo, A. Hakola, E. H. H. JOFFRIN, D. Keeling, B. Labit, E. Tsitrone, N. Vianello, M. Wischmeier, I. Balboa, J. Bernardo, M. Bernert, T. Bosman, S. Brezinsek, D. Brida, I. S. Carvalho, P. Carvalho, L. Ceelen, C. D. Challis, I. H. Coffey, T. Dittmar, M. G. Dunne, M. Faitsch, A. R. Field, L. Frassinetti, L. Garzotti, Z. Ghani, C. Giroud, S. S. Henderson, R. Henriques, J. Hobirk, P. Jacquet, I. Jepu, Y. Kazakov, D. King, K. K. Kirov, D. Kos, K. Krieger, M. Lennholm, E. Lerche, X. L. Litaudon, E. Litherland-Smith, P. Lomas, C. G. Lowry, J. Mailloux, M. Mantsinen, M. Maslov, D. Matveev, A. Meigs, S. Menmuir, cameron Olde, C. P. von Thun, L. Piron, G. Pucella, H. Reimerdes, F. Rimini, O. Sauter, P. A. Schneider, B. Sieglin, S. A. Silburn, E. R. Solano, H. Sun, D. Valcarcel, D. V. Eester, R. Villari, A. Widdowson, S. Wiesen, M. Zlobinski, and V. K. Zotta, "Overview of the third jet deuterium-tritium campaign," *Plasma Physics and Controlled Fusion*, 3 2025. (*Cited on page 2*)

[4] J. P. Freidberg, *Plasma Physics and Fusion Energy*. Cambridge University Press, 2 2007. (*Cited on pages 2, 4, 6, 8, 12*)

[5] S. Li, H. Jiang, Z. Ren, and C. Xu, "Optimal tracking for a divergent-type parabolic pde system in current profile control," *Abstract and Applied Analysis*, vol. 2014, pp. 1–8, 2014. (*Cited on page 3*)

[6] M. G. Haines, "A review of the dense z-pinch," *Plasma Physics and Controlled Fusion*, vol. 53, p. 093001, 9 2011. (*Cited on page 4*)

[7] R. DAVIDSON and J. FREIDBERG, "Review of toroidal theta-pinch theory," *Pulsed High Beta Plasmas*, pp. 13–38, 1976. (*Cited on page 5*)

[8] M. Zuin, M. Agostini, F. Auriemma, D. Bonfiglio, S. Cappello, L. Carraro, R. Cavazzana, L. Cordaro, P. Franz, L. Marrelli, E. Martines, M. Puiatti, R. Piovan, G. Spizzo, D. Terranova, N. Vianello, P. Zanca, B. Zaniol, and L. Zanotto, "Dynamics of ultralow-q plasmas in the rfx-mod device," *Nuclear Fusion*, vol. 62, p. 066029, 6 2022. (*Cited on pages 6, 10, 11, 26, 28, 29, 106, 123*)

[9] I. G. J. Classen, "Imaging and control of magnetic islands in tokamaks," 2007. (*Cited on page 7*)

[10] J. P. Freidberg, *Ideal MHD*. Cambridge University Press, 6 2014. (*Cited on page 7*)

[11] B. Kadomstev, "Disruptive instability in tokamaks," *Soviet Journal of Plasma Physics*, vol. 1, pp. 389–391, 9 1975. (*Cited on page 8*)

[12] L. Marrelli, P. Martin, M. Puiatti, J. Sarff, B. Chapman, J. Drake, D. Escande, and S. Masamune, "The reversed field pinch," *Nuclear Fusion*, vol. 61, p. 023001, 2 2021. (*Cited on page 9*)

[13] Z. Yoshida, N. Inoue, T. Fujita, H. Morimoto, J. Matsui, S. Takeji, D. Nagahara, T. Okabe, H. Nihei, and J. Morikawa, "Experimental scaling of anomalous resistance in

ultra-low q discharges," *Nuclear Fusion*, vol. 31, pp. 1532–1535, 8 1991. (*Cited on pages 10, 24*)

[14] I. R. Goumiri, K. J. McCollam, A. A. Squitieri, D. J. Holly, J. S. Sarff, and S. P. Leblanc, "Simultaneous feedback control of toroidal magnetic field and plasma current on mst using advanced programmable power supplies," *Plasma Research Express*, vol. 2, p. 035012, 9 2020. (*Cited on pages 11, 41*)

[15] K. Miyamoto, *Fundamentals of Plasma Physics and Controlled Fusion*, 2000. (*Cited on pages 12, 64, 117*)

[16] P. Horling, G. Hedin, J. H. Brzozowski, E. Tennfors, and S. Mazur, "Ion temperature, heating and scaling relations at the extrap-t1 reversed-field pinch," *Plasma Physics and Controlled Fusion*, vol. 38, pp. 1725–1742, 10 1996. (*Cited on page 13*)

[17] M. Gobbin, M. Agostini, F. Auriemma, L. Carraro, R. Cavazzana, A. Fassina, P. Franz, L. Marrelli, B. Momo, R. Piovan, I. Predebon, M. Puiatti, G. Spizzo, D. Terranova, M. Zuin, and R. mod Team, "Ion heating and energy balance during magnetic reconnection events in the rfx-mod experiment," *Nuclear Fusion*, vol. 62, p. 026030, 2 2022. (*Cited on page 13*)

[18] A. Ejiri and K. Miyamoto, "Ion-heating model during magnetic reconnection in reversed-field pinch plasmas," *Plasma Physics and Controlled Fusion*, vol. 37, pp. 43–56, 1 1995. (*Cited on page 13*)

[19] S. Gangadhara, D. Craig, D. A. Ennis, D. J. D. Hartog, G. Fiksel, and S. C. Prager, "Ion heating during reconnection in the madison symmetric torus reversed field pinch," *Physics of Plasmas*, vol. 15, 5 2008. (*Cited on pages 13, 20, 22*)

[20] V. A. Svidzinski, G. Fiksel, V. V. Mirnov, and S. C. Prager, "Modeling of ion heating from viscous damping of reconnection flows in the reversed field pinch," *Physics of Plasmas*, vol. 15, 6 2008. (*Cited on pages 13, 34*)

[21] S. C. Guo, R. Paccagnella, and F. Romanelli, "Ion-temperature-gradient-driven instability and anomalous ion heating in reversed-field pinches," *Physics of Plasmas*, vol. 1, pp. 2741–2747, 8 1994. (*Cited on page 13*)

[22] V. Tangri, P. W. Terry, and G. Fiksel, "Anomalous impurity ion heating from alfvénic cascade in the reversed field pinch," *Physics of Plasmas*, vol. 15, 11 2008. (*Cited on pages 13, 30, 31, 32*)

[23] S. T. A. Kumar, A. F. Almagri, D. Craig, D. J. D. Hartog, M. D. Nornberg, J. S. Sarff, and P. W. Terry, "Charge-to-mass-ratio-dependent ion heating during magnetic reconnection in the mst rfp," *Physics of Plasmas*, vol. 20, 5 2013. (*Cited on page 13*)

[24] G. Fiksel, A. F. Almagri, B. E. Chapman, V. V. Mirnov, Y. Ren, J. S. Sarff, and P. W. Terry, "Mass-dependent ion heating during magnetic reconnection in a laboratory plasma," *Physical Review Letters*, vol. 103, p. 145002, 9 2009. (*Cited on pages 13, 21, 32, 33, 116*)

[25] T. Fujita, K. Saito, J. Matsui, Y. Kamada, H. Morimoto, Z. Yoshida, and N. Inoue, "Anomalous ion heating in repute-1 ultra-low q and reversed field pinch plasmas," *Nuclear Fusion*, vol. 31, pp. 3–14, 1 1991. (*Cited on pages 13, 24, 32, 107*)

[26] K. Wilhelm, E. Marsch, B. N. Dwivedi, and U. Feldman, "Observations of the sun at vacuum-ultraviolet wavelengths from space. part ii: Results and interpretations," *Space Science Reviews*, vol. 133, pp. 103–179, 12 2007. (*Cited on page 17*)

[27] T. A. Bowen, B. D. Chandran, J. Squire, S. D. Bale, D. Duan, K. G. Klein, D. Larson, A. Mallet, M. D. McManus, R. Meyrand, J. L. Verniero, and L. D. Woodham, "In situ signature of cyclotron resonant heating in the solar wind," *Physical Review Letters*, vol. 129, p. 165101, 10 2022. (*Cited on pages 17, 30*)

[28] S. R. Cranmer, G. B. Field, and J. L. Kohl, "Spectroscopic constraints on models of ion cyclotron resonance heating in the polar solar corona and high-speed solar wind," *The Astrophysical Journal*, vol. 518, pp. 937–947, 6 1999. (*Cited on pages 17, 30*)

[29] B. B. Jones and R. Wilson, "Spectroscopic studies of ion energies in zeta," *Nuclear Fusion Supplement*, vol. 3, 1962. (*Cited on page 18*)

[30] R. B. Howell and H. J. Karr, "Spectroscopic measurements of the plasma temperature in the zt-1 toroidal pinch," *The Physics of Fluids*, vol. 19, pp. 2012–2020, 12 1976. (*Cited on page 18*)

[31] R. B. Howell and Y. Nagayama, "Ion energy measurements on a reversed-field pinch experiment using doppler broadening," *The Physics of Fluids*, vol. 28, pp. 743–748, 2 1985. (*Cited on page 18*)

[32] E. Scime, S. Hokin, N. Mattor, and C. Watts, "Ion heating and magnetohydrodynamic dynamo fluctuations in the reversed-field pinch," *Physical Review Letters*, vol. 68, pp. 2165–2167, 4 1992. (*Cited on page 18*)

[33] R. Magee, "Ion energization during tearing mode magnetic reconnection in a high temperature plasma," 2011. (*Cited on pages 19, 30, 47*)

[34] Y. Ren, A. F. Almagri, G. Fiksel, S. C. Prager, J. S. Sarff, and P. W. Terry, "Experimental observation of anisotropic magnetic turbulence in a reversed field pinch plasma," *Physical Review Letters*, vol. 107, p. 195002, 10 2011. (*Cited on page 19*)

[35] M. Yamada and H. Ji, "Study of magnetic reconnection in collisional and collionless plasmas in magnetic reconnection experiment (mrx)," *Proceedings of the International Astronomical Union*, vol. 6, pp. 10–17, 9 2010. (*Cited on page 20*)

[36] Y. Ono, Y. Hayashi, T. Ii, H. Tanabe, S. Ito, A. Kuwahata, T. Ito, Y. Kamino, T. Yamada, and M. Inomoto, "Intermittent magnetic reconnection in ts-3 merging experiment," *Physics of Plasmas*, vol. 18, p. 111213, 11 2011. (*Cited on page 20*)

[37] S. C. Hsu, T. A. Carter, G. Fiksel, H. Ji, R. M. Kulsrud, and M. Yamada, "Experimental study of ion heating and acceleration during magnetic reconnection," *Physics of Plasmas*, vol. 8, pp. 1916–1928, 5 2001. (*Cited on page 20*)

[38] H. Tanabe, T. Yamada, T. Watanabe, K. Gi, K. Kadowaki, M. Inomoto, R. Imazawa, M. Gryaznevich, C. Michael, B. Crowley, N. Conway, R. Scannell, J. Harrison, I. Fitzgerald, A. Meakins, N. Hawkes, K. McClements, T. O'Gorman, C. Cheng, and Y. Ono, "Electron and ion heating characteristics during magnetic reconnection in the mast spherical tokamak," *Physical Review Letters*, vol. 115, p. 215004, 11 2015. (*Cited on page 20*)

[39] D. J. D. Hartog and D. Craig, "Isotropy of ion heating during a sawtooth crash in a reversed-field pinch," *Plasma Physics and Controlled Fusion*, vol. 42, pp. L47–L53, 12 2000. (*Cited on pages 23, 30*)

[40] R. M. Magee, D. J. D. Hartog, S. T. A. Kumar, A. F. Almagri, B. E. Chapman, G. Fiksel, V. V. Mirnov, E. D. Mezonlin, and J. B. Titus, "Anisotropic ion heating and tail generation during tearing mode magnetic reconnection in a high-temperature plasma," *Physical Review Letters*, vol. 107, p. 065005, 8 2011. (*Cited on pages 23, 24*)

[41] P. C. THONEMANN, E. P. BUTT, R. CARRUTHERS, A. N. DELLIS, D. W. FRY, A. GIBSON, G. N. HARDING, D. J. LEES, R. W. P. MCWHIRTER, R. S. PEASE, S. A. RAMSDEN, and S. WARD, "Controlled release of thermonuclear energy: Production of high temperatures and nuclear reactions in a gas discharge," *Nature*, vol. 181, pp. 217–220, 1 1958. (*Cited on page 24*)

[42] Z. Yoshida, S. ichi Ishida, K. ichi Hattori, Y. Murakami, J. Morikawa, H. Nihei, and N. Inoue, "Remarkes on relaxation phenomena in toroidal discharge," *Journal of the Physical Society of Japan*, vol. 55, pp. 450–453, 2 1986. (*Cited on page 24*)

[43] H. Yamada, K. Kusano, Y. Kamada, M. Utsumi, Z. Yoshida, and N. Inoue, "Observation of ultra low q equilibrium," *Nuclear Fusion*, vol. 27, pp. 1169–1173, 7 1987. (*Cited on page 24*)

[44] Y. Kamada, T. Fujita, Y. Murakami, T. Ohira, K. Saitoh, Y. Fuke, M. Utsumi, Z. Yoshida, and N. Inoue, "Recent results of ultra low q experiments in toriut-6 and repute-1," *Nuclear Fusion*, vol. 29, pp. 713–728, 5 1989. (*Cited on page 24*)

[45] H. TSUI, R. LaHAYE, and J. CUNNANE, "Sustainment of low-q tokamak, ultra-low-q and reversed field pinch discharges in hbtx-1c with a resistive shell," *Nuclear Fusion*, vol. 30, p. 59, 1990. (*Cited on page 25*)

[46] D. Bonfiglio, S. Cappello, R. Piovan, L. Zanotto, and M. Zuin, "3d nonlinear mhd simulations of ultra-low q plasmas," *Nuclear Fusion*, vol. 48, p. 115010, 11 2008. (*Cited on pages 26, 27*)

[47] K. Franco and C. Sovinec, "Computations of macroscale dynamics in the ultra-low safety factor regime," *2025 Sherwood Fusion Theory Conference*, 4 2025. (*Cited on pages 28, 30, 130*)

[48] C. Sovinec, A. Glasser, T. Gianakon, D. Barnes, R. Nebel, S. Kruger, D. Schnack, S. Plimpton, A. Tarditi, and M. Chu, "Nonlinear magnetohydrodynamics simulation using high-order finite elements," *Journal of Computational Physics*, vol. 195, pp. 355–386, 3 2004. (*Cited on page 28*)

[49] J. M. McChesney, R. A. Stern, and P. M. Bellan, "Observation of fast stochastic ion heating by drift waves," *Physical Review Letters*, vol. 59, pp. 1436–1439, 9 1987. (*Cited on page 32*)

[50] J. R. Johnson and C. Z. Cheng, "Stochastic ion heating at the magnetopause due to kinetic alfvén waves," *Geophysical Research Letters*, vol. 28, pp. 4421–4424, 12 2001. (*Cited on page 32*)

[51] J. M. McChesney, P. M. Bellan, and R. A. Stern, "Observation of fast stochastic ion heating by drift waves," *Physics of Fluids B: Plasma Physics*, vol. 3, pp. 3363–3378, 12 1991. (*Cited on pages 33, 116*)

[52] E. G. Zweibel and M. Yamada, "Perspectives on magnetic reconnection," *Proceedings of the Royal Society A: Mathematical, Physical and Engineering Sciences*, vol. 472, p. 20160479, 12 2016. (*Cited on page 34*)

[53] S. Braginskii, *Reviews of Plasma Physics*. Consultants Bureau, 1965. (*Cited on pages 35, 107*)

[54] H. R. Strauss, B. E. Chapman, and N. C. Hurst, "Mst resistive wall tearing mode simulations," *Plasma Physics and Controlled Fusion*, vol. 65, 2023. (*Cited on page 40*)

[55] J. J. Koliner, "Neutral beam excitation of alfven continua in the madison symmetric torus reversed field pinch," 2013. (*Cited on page 41*)

[56] J. C. Triana, "Measurements of two-fluid relaxation in the madison symmetric torus," 2017. (*Cited on page 43*)

[57] T. Nishizawa, A. F. Almagri, W. Goodman, S. Ohshima, and J. S. Sarff, "Development of a multi-channel capacitive probe for electric field measurements with fine spatial and high time resolution," *Review of Scientific Instruments*, vol. 89, 10 2018. (*Cited on page 43*)

[58] M. Tan, D. R. Stone, J. C. Triana, A. F. Almagri, G. Fiksel, W. Ding, J. S. Sarff, K. J. McCollam, H. Li, and W. Liu, "A multi-channel capacitive probe for electrostatic fluctuation measurement in the madison symmetric torus reversed field pinch," *Review of Scientific Instruments*, vol. 88, 2 2017. (*Cited on page 43*)

[59] E. Parke, W. X. Ding, J. Duff, and D. L. Brower, "An upgraded interferometer-polarimeter system for broadband fluctuation measurements," *Review of Scientific Instruments*, vol. 87, 11 2016. (*Cited on page 44*)

[60] S. R. Burns, W. A. Peebles, D. Holly, and T. Lovell, "Madison symmetric torus far-infrared interferometer," *Review of Scientific Instruments*, vol. 63, pp. 4993–4995, 10 1992. (*Cited on page 44*)

[61] B. H. Deng, D. L. Brower, W. X. Ding, M. D. Wyman, B. E. Chapman, and J. S. Sarff, "High-speed three-wave polarimeter-interferometer diagnostic for madison symmetric torus," *Review of Scientific Instruments*, vol. 77, 10 2006. (*Cited on page 44*)

[62] J. Duff, "Observation of trapped-electron mode microturbulence in improved confinement reversed-field pinches," 2018. (*Cited on page 44*)

[63] I. H. Hutchinson, "Principles of plasma diagnostics: Second edition," *Plasma Physics and Controlled Fusion*, vol. 44, pp. 2603–2603, 12 2002. (*Cited on pages 44, 46*)

[64] D. Craig, D. J. D. Hartog, D. A. Ennis, S. Gangadhara, and D. Holly, "High throughput spectrometer for fast localized doppler measurements," *Review of Scientific Instruments*, vol. 78, 1 2007. (*Cited on page 45*)

[65] T. Nishizawa, M. D. Nornberg, D. J. D. Hartog, and D. Craig, "Upgrading a high-throughput spectrometer for high-frequency measurements," *Review of Scientific Instruments*, vol. 87, 11 2016. (*Cited on pages 45, 50*)

[66] D. J. D. Hartog, D. Craig, D. A. Ennis, G. Fiksel, S. Gangadhara, D. J. Holly, J. C. Reardon, V. I. Davydenko, A. A. Ivanov, A. A. Lizunov, M. G. O'Mullane, and H. P. Summers, "Advances in neutral-beam-based diagnostics on the madison symmetric torus reversed-field pinch (invited)," *Review of Scientific Instruments*, vol. 77, 10 2006. (*Cited on page 46*)

[67] D. Craig, D. J. D. Hartog, G. Fiksel, V. I. Davydenko, and A. A. Ivanov, "First charge exchange recombination spectroscopy and motional stark effect results from the madison symmetric torus reversed field pinch," *Review of Scientific Instruments*, vol. 72, pp. 1008–1011, 1 2001. (*Cited on page 47*)

[68] G. F. Abdrashitov, V. I. Davydenko, P. P. Deichuli, D. J. D. Hartog, G. Fiksel, A. A. Ivanov, S. A. Korepanov, S. V. Murakhtin, and G. I. Shulzhenko, "A diagnostic neutral beam system for the mst reversed-field pinch," *Review of Scientific Instruments*, vol. 72, pp. 594–597, 1 2001. (*Cited on page 47*)

[69] S. Gangadhara, D. Craig, D. A. Ennis, and D. J. D. Hartog, "Modeling fast charge exchange recombination spectroscopy measurements from the madison symmetric torus," *Review of Scientific Instruments*, vol. 77, 10 2006. (*Cited on page 47*)

[70] S. T. A. Kumar, D. J. D. Hartog, V. V. Mirnov, K. J. Caspary, R. M. Magee, D. L. Brower, B. E. Chapman, D. Craig, W. X. Ding, S. Eilerman, G. Fiksel, L. Lin, M. Nornberg, E. Parke, J. A. Reusch, and J. S. Sarff, "Classical confinement and outward convection of impurity ions in the mst rfp," *Physics of Plasmas*, vol. 19, 5 2012. (*Cited on page 107*)

[71] T. Barbui, L. Carraro, D. J. D. Hartog, S. T. A. Kumar, and M. Nornberg, "Impurity transport studies in the madison symmetric torus reversed-field pinch during standard and pulsed poloidal current drive regimes," *Plasma Physics and Controlled Fusion*, vol. 56, p. 075012, 7 2014. (*Cited on page 107*)

[72] Z. Xing, "Ion thermal transport and heating in reduced tearing rfp plasmas," 2019. (*Cited on page 107*)

[73] J. Callen, *Fundamentals of Plasma Physics*, 2006. (*Cited on page 109*)

[74] D. Salzmann, *Atomic Physics in Hot Plasmas*. Oxford University PressNew York, NY, 8 1998. (*Cited on pages 111, 112*)

[75] R. E. Olson, E. J. Shipsey, and J. C. Browne, "Charge-transfer cross sections for b3+ , c4+ +h collisions," *Journal of Physics B: Atomic and Molecular Physics*, vol. 11, pp. 699–708, 2 1978. (*Cited on page 111*)

[76] M. A. Bautista and N. R. Badnell, "Dielectronic recombination data for dynamic finite-density plasmas," *Astronomy and Astrophysics*, vol. 466, pp. 755–762, 5 2007. (*Cited on page 112*)

[77] U. Gupta and C. R. Sovinec, "Pressure-driven tearing and thermal transport in finite-beta reversed field pinch computations," *Physics of Plasmas*, vol. 30, 1 2023. (*Cited on page 130*)